# TOWARDS ANGLE-CONTROLLED VAN DER WAALS HETEROSTRUCTURES

A Dissertation

Presented to the Faculty of the Graduate School

of Cornell University

In Partial Fulfillment of the Requirements for the Degree of

Doctor of Philosophy

by

Lola Brown

August 2015

# TOWARDS ANGLE-CONTROLLED VAN DER WAALS HETEROSTRUCTURES

Lola Brown, Ph. D.

Cornell University 2015

Two-dimensional (2D) materials such as graphene exhibit a combination of unique electronic, mechanical, and optical properties that have drawn significant attention over the past decade. While there has been extensive investigation into individual 2D materials, the burgeoning field of 2D heterostructures offers an even richer array of desirable properties. This led to increasing efforts to controllably manipulate these materials and to tailor them toward potential applications. An important step toward the realization of functional 2D heterostructures is the fabrication and characterization of high quality bilayers with a uniform rotation angle ($\theta$) between the constituent layers. The rotation angle represents a new degree of freedom capable of tuning both optical and electrical properties and is therefore a critical component in designing heterostructures for specific applications.

In this thesis, we discuss the fabrication of bilayer graphene with a controlled rotation angle. To accomplish this, we first develop an application of transmission electron microscopy (TEM) capable of imaging the structure and atomic registry between graphene layers in bilayer and trilayer structures. We then introduce a new method for creating graphene and hexagonal boron nitride (*h*-BN) single layers with crystallographic alignment over large scales, and we characterize the structural and

electronic uniformity of these films using a variety of techniques, including TEM, low-energy electron diffraction (LEED), and angle-resolved photoemission spectroscopy. We conclude by showing that these large-scale aligned films can be used as building blocks for 2D layered structures with a controllable rotation angle and uniform optical properties. These findings provide a framework for imaging and fabricating angle-controlled heterostructures that is extensible beyond graphene and *h*-BN to a variety of 2D materials, thereby opening the door to a virtually limitless combination of 2D heterostructures with uniquely tailored properties.

# BIOGRAPHICAL SKETCH

Lola Brown was born in 1982 and grew up in a small town near Jerusalem, Israel. She completed her military service, and graduated from the Adi Lautman program for outstanding students at Tel Aviv University. After earning her M.Sc. degree in Chemistry in 2010 from Tel Aviv University, she entered the Chemistry and Chemical Biology doctoral program at Cornell University, where she received a Fulbright Doctoral Fellowship. She completed her Ph.D. under the supervision of Professor Jiwoong Park.

To Ima, Aba, Dor, and Guy

ACKNOWLEDGEMENT

This work would not have been possible without the support of many dear friends and colleagues. First and foremost, I owe the greatest thanks to my family. Ima, Aba, Dor, and Guy, you are the wind under my wings. You have always supported my wildest projects, and offered advice, help and encouragement, even when there was an ocean between us. Your good nature, enthusiasm, and creativity inspire me to be the best person I can be. I can't thank you enough for the great love you've surrounded me with, and I dedicate this thesis to you with love.

I wouldn't be here today without much love and support from my extended family. Savta Chana has encouraged my academic development and supported me throughout boarding school. I know she would have been proud of her granddaughter's PhD. I also spent many happy days with Savta Sylvia and Saba David, who taught me how to appreciate time spent together, and how to build things and nurture kittens and roses. Aunt Zoe and uncle Shalom and their children, Hadas, Zohar, and Elisha, have surrounded me with love and with delicious foods (and made uncle Shalom's famous Fish Patties every time I came to visit). I hope to keep you in my life always.

The choice of joining the Park group has shaped my time at Cornell. Jiwoong, your sharp wit and your commitment to the scientific process have been an inspiration to me. You demanded creativity, independence, and deep conviction in my work, and never settled for anything less than adequate. Even though the process was, at times, frustrating, I am now an incredibly better scientist than when I started. You have also encouraged me to explore my true passion, and for that I am eternally grateful.

I would also like to thank the other members of my committee, Professor David Muller and Professor William Dichtel. Your insights and advice have been

invaluable through the years. I am also thankful for the opportunity to work with a number of other Professors and experts through collaborations, including Kyle Shen, Rodney Ruoff, Abhay Pasupathy, Maria Asensio, José Avila, and Paul McEuen.

I owe much of my success in graduate school to my choice of wonderful collaborators. The work done in this thesis could not have been written without the ongoing collaboration with Robert Hovden and Edward Lochocki. Robby and Ed, thank you for sharing your expertise with such patience and enthusiasm. The pleasure, as always, was mine. Furthermore, I was fortunate to collaborate with a large group of talented graduate students and postdocs, with special thanks to Pinshane Huang, Daniel Shai, Eric Monkman, Haofei Wei, ShanShan Chen, and Christopher Gutiérrez. I am also thankful for the technical support provided by John Grazul on the TEM and Nathan Ellis in the Machine Shop, as well as many of the CNF and CCMR staff. Things would not have gone as smoothly without you.

The collaborative spirit of the Park group is another thing I am profoundly grateful for. I have benefited from the wisdom and companionship of many of the Park group members, with special thanks to Robin Havener, Mark Levendorf, Wei Tsen, Cheol-Joo Kim, Yui Ogawa, Michal Wojcik, Nicholas Rolston, and Dong-Ki Kim. I also enjoyed scientific discussions and time spent with Carlos Ruiz-Vargas, Lujie Huang, Matt Graham, Kin Fai Mak, Zenghui Wang, Chibeom Park, Lihong Herman, Daniel Joh, Michael Segal, Sang-Yong Ju, Joel Sleppy, Saien Xie, Kibum Kang, Yimo Han, Kan-heng Lee, Hui Gao, Zack Ziegler, and Marcos Guimarães.

This thesis was mostly written on Daniel Shai's dining table while he provided me with writing space and delicious snacks. Daniel, you deserve an extremely special thank-you for your sense of humor and your clear thinking, which light up my days and frequently serve to get me out of a rut.

Spending time away from the lab, through rare, was particularly joyous thanks

to several dear friends. Robin, Mark, Cheol-Joo, Wei, and Carlos, they say the best friendships are forged on the battlefield – thank you for sharing the PhD battlefield with me in many parties, cookouts, and travels. I hope our gang will come together for many more happy occasions. Robert Hovden and Kara Church, your house has become my second home, thank you for graciously providing room on your couch and many reasons to celebrate. A big thank-you goes to Lennessa Shantaya for her gentle teaching and her kindness. I am eternally grateful for the company of my girlfriends – Robin Havener, Sasha Devore, Sisca Harya, Kara Church, Shira Kritchman, Noa Marom, Tauhira Hoossainy, Hyeri Anna Lee, and Elva Cha – you walked into my life precisely when I needed you. I am so blessed to have found the company of such wonderful friends throughout my time in Ithaca. Thank you all!

Lola Brown

August 2015

TABLE OF CONTENTS

LIST OF FIGURE

# CHAPTER 1

# INTRODCUTION

## 1.1 Overview

Graphene is a two-dimensional (2D) sheet composed entirely of carbon atoms arranged in a hexagonal lattice. It was the first 2D crystal to be isolated and has been featured as the new 'wonder' material, promising to upend the world of electronic materials[1]. Graphene has a wide variety of unique properties such as high electrical and thermal conductivities, high mechanical strength, elasticity, transparency, and impermeability, making it well-suited for many novel applications[2]. For example, its low sheet resistance and transparency render it as a potential replacement for indium titanium oxide (ITO) as a low-cost electrode for touch screens[3,4] and solar cells[5]; its low bending radius, high fracture strain, and uniform absorption across the visible spectrum make it suitable for flexible, lightweight, biocompatible electronic devices[6,7]; its extremely high electron mobility makes it an ideal material for high frequency transistors[8,9], as well as many other applications[10] such as photodetectors[11], strain gauges[12], conductive inks[13].

Since its discovery in 2004, graphene has generated interest in an entire family of 2D materials, including hexagonal boron nitride (*h*-BN) and a variety of transition metal dichalcogenides (TMDs)[14]. These are layered Van der Waals (VdW) materials, which are characterized by strong in-plane bonding and weak VdW interlayer interactions, and span a variety of electronic and mechanical properties. Their versatility has drawn interest from both research and industry. If graphene alone can

inspire such a wide array of applications as described above, then the entire 2D family, as well as their layered and juxtaposed combinations, has the potential to enhance current technologies and create entirely new fields. 2D films possess several clear advantages over traditional materials. Compared with metallic thin-films, which become discontinuous when their thickness drops below several nanometers, 2D materials such as graphene are stable in the form of an atomically thin membrane. And unlike semiconducting interfaces, which are buried between slabs of bulk material, the properties of 2D materials are defined by their in-plane crystalline structure and chemical composition, and thus can be suspended or supported by a variety of substrates without compromising their performance. The inherent properties of 2D crystals can also be modified by their surroundings, opening the door to the design of structurally-controlled functionalities for a variety of applications.

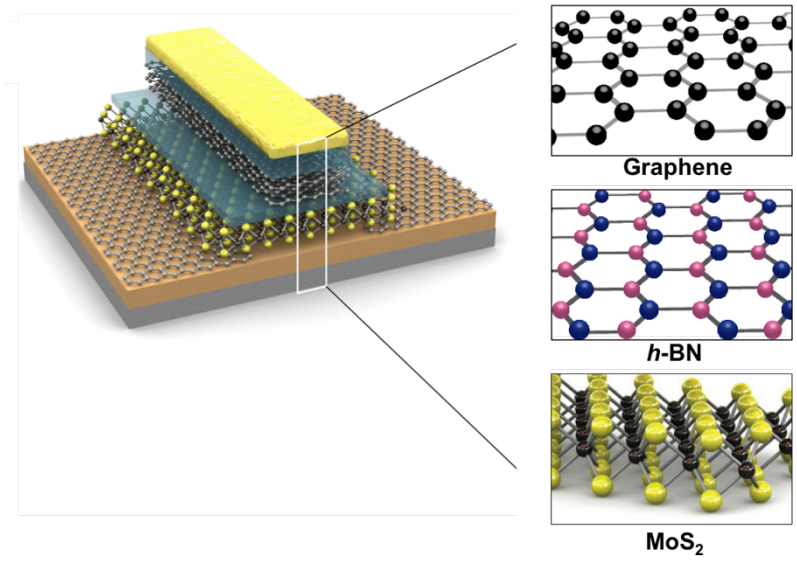


**Figure 1.1: Layered device with 2D building blocks.** An illustration of a heterostructure device, built from layers of 2D crystals such as graphene, *h*-BN, and $MoS_2$. Adapted from [14] and [15].

The field of 2D materials has experienced tremendous progress in the past decade as researchers around the world work to increase our understanding of the growth, fabrication, and fundamental properties of 2D crystals. While each material offers new and exciting applications, the combination of several types of 2D films into a heterostructure with uniquely tailored properties (see illustration in Figure 1.1), has become the focus of the 2D research community in recent years. Nevertheless, before 2D heterostructures reach maturity as viable candidates for technology applications, there are a number of challenges that must be addressed.

First, growth and fabrication methods for producing high quality 2D materials must be developed, and their structural and performance homogeneity must be assessed. The production of uniform 2D sheets over large areas requires developing control over the growth process, and the creation of heterostructures from these sheets requires techniques for combining these materials with precise structural and electronic control.

Second, methods to efficiently characterize the structural, electronic, optical and mechanical properties of the fabricated heterostructures over a large spatial scale are required.

In this thesis, we address these challenges for layered graphene systems, which presents several interesting avenues themselves, and also serves as a prototypical system for the development of more complicated heterostructures in the future. We discuss our vision of the potential embodied in layered graphene structures, and present original methods for overcoming the challenges depicted above.

First, we present a dark-field transmission electron microscopy (DF-TEM) method for characterizing the structure of two- and three- layered graphene stacks found in chemical vapor deposition (CVD) grown graphene. The high level of non-uniformity found in the as-grown layered graphene samples motivates the next part our study, where we present a method for growing single layer graphene (SLG) sheets with structural and electronic uniformity over centimeter scale. We then use these uniform SLG sheets as building blocks in creating angle-controlled bilayer graphene stacks, and we characterize their optical and structural uniformity over large scales. The remainder of this chapter includes a general introduction to the structure, growth, and applications of graphene and graphene layers, which will provide the background material for subsequent chapters of this thesis.

## 1.2 Introduction to 2D Materials

### 1.2.1 Graphene

Ever since the 2004 discovery that single atomic layers of graphite could be stably isolated using mechanical exfoliation[16], there has been a rapid effort to investigate the various properties of the resulting 2D sheet, graphene[17]. Graphene has a unique crystalline structure (Figure 1.2) which gives rise to a host of exceptional characteristics.

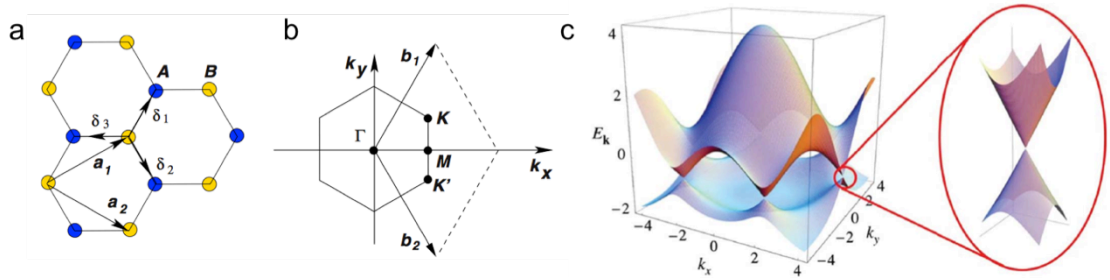


**Figure 1.2: Electronic band structure of graphene. a,** Honeycomb lattice of graphene with two inequivalent carbon atoms per unit cell, *A* (blue) and *B* (yellow), with a lattice constant of a = 2.46 Å. **b,** Brillouin zone of graphene. **c,** Left: Tight binding calculated band structure of graphene, energy is plotted in units of tight binding parameter t = 2.7 eV. Right: Zoom in on the linear band-structure in low energies near the K-point. Reproduced from [18].

Electronically, its band-structure near its K-points resembles that of relativistic massless particles (see Figure 1.2c). This allows carriers to move with extremely high electron mobility, up to 250,000 $cm^2/Vs$ for suspended SLG at 1.5 K (and up to 500,000 $cm^2/Vs$ for bilayer/trilayer graphene), about 200 times greater than that of silicon[19], as demonstrated in Figure 1.3. However, electron mobility values may vary with the film's quality, as will be further discussed in Chapter 3. Graphene also possesses high thermal conductivity, above 3,000 $W\ m^{-1}\ K^{-1}$, an order of magnitude higher compared to copper (Cu)[20,21].

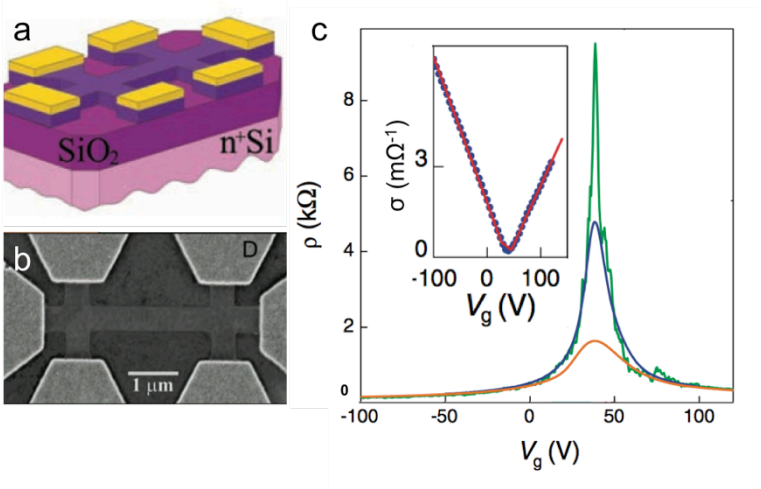


**Figure 1.3: Electronic properties of graphene. a,** Illustration of a multichannel Hall bar device. **b,** SEM image of the device in (a), showing etched graphene channels between the electrodes. **c,** Typical dependences of few layer graphene's resistivity (ρ) on gate voltage ($V_g$) for different temperatures (T = 5, 70, and 300 K for top to bottom curves, respectively). Inset: Example of changes in the film's conductivity $\sigma = 1/\rho(V_g)$, obtained by inverting the 70 K curve (dots). Adapted from [16].

Mechanically, graphene has a Young's modulus of 1 TPa and an intrinsic strength close to 130 GPa, greater than that of any other material, due to the large energies of its covalent carbon-carbon bonds[22]. Additionally, graphene is also impermeable to gases[23], and relatively inert – making it an ideal membrane for protective coating[24].

Optically, graphene's band-structure enables it to absorb 2.3% of light per layer uniformly over the visible and IR range Figure 1.4a, a surprisingly large value for an atomically thin material[25]. Absorption is increased in the UV (see Figure 1.4b) due to the saddle-point singularity near the M point[26].

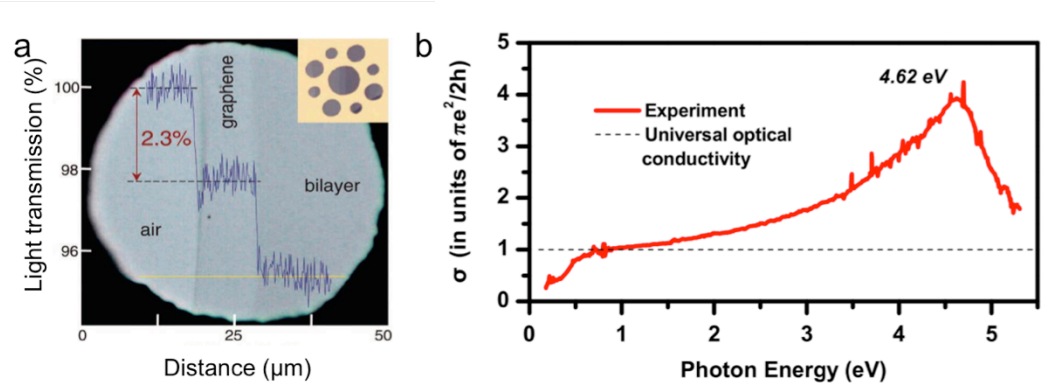


**Figure 1.4: Optical properties of graphene layers. a,** Uniform 2.3% absorption in the visible range per layer. Reproduced from [25]. **b,** Graphene's measured optical conductivity σ(E) over a range of photon energies, E = 0.2-5.3 eV. Reproduced from [26].

### 1.2.2 Hexagonal Boron Nitride

Hexagonal boron nitride (*h*-BN) is a structure analogue of graphene in which alternating boron and nitrogen atoms substitute the carbon atoms (Figure 1.5a). In its bulk form it has been used for industrial applications since the 1940's. Thanks to its electrical insulation properties, as well as its thermal and chemical stability, it has been used as an intercalation host and as a dry lubricant in the cosmetics, plastics, machine parts, and space industries, among others. In its 2D form, a single sheet of *h*-BN is an insulator with a large band-gap of 5.97 eV, which turns it into a functional insulator for 2D-based circuits[27].

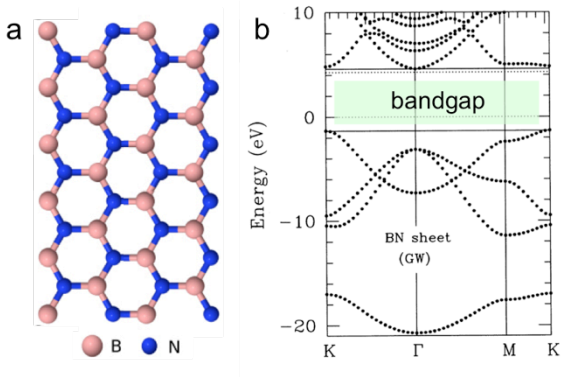


**Figure 1.5: Hexagonal Boron Nitride. a,** An illustration of the atomic structure of *h*-BN, a hexagonal lattice with alternating boron and nitrogen atoms. Adapted from [28]. **b,** Theoretically calculated band structure of *h*-BN, featuring a large band gap of 5.97 eV. Adapted from [29].

Nonetheless, its most intriguing application may be as part of an *h*-BN/Graphene heterostructure. It has been shown that graphene on *h*-BN is ultra-flat, thus decreasing scattering and increasing device performance 10-fold[30,31]. Additionally, the added *h*-BN layer can allow for modification of the graphene band structure. Specifically, the periodic modulation applied by the *h*-BN sheet allows for band-gap opening in the graphene band structure – a crucial aspect for implementing graphene as a active component in transistor devices[32–34]. Similar to graphene, *h*-BN can be grown by chemical vapor deposition (CVD) process on Cu substrates[35], and thus advances in graphene growth can often be directly applied to *h*-BN. The similarity in growth conditions also allows for graphene and *h*-BN to be directly integrated in planar devices, thus enabling complex geometries with high quality inter-stitching, while minimizing transfer steps and contaminations[36]. This capability will be further discussed in Appendix B.

### 1.2.3 $MoS_2$ and Other Dichalcogenides

Transition metal dichalcogenides (TMDs) are a large class of three-atom-thick 2D crystals, with varying properties depending on their chemical composition. TMDs have the general formula of $MX_2$, where M is a transition metal, and X is a chalcogen, and they include materials such as $MoS_2$, $MoSe_2$, $WS_2$, $NbSe_2$, and others[37]. Like graphene and *h*-BN, these materials can be exfoliated from bulk crystals[38], or grown using epitaxial growth or CVD methods[39]. Specifically, the single layer form of molybdenum disulfide ($MoS_2$) has attracted recent attention as a semiconductor analogue of graphene (see Figure 1.6).

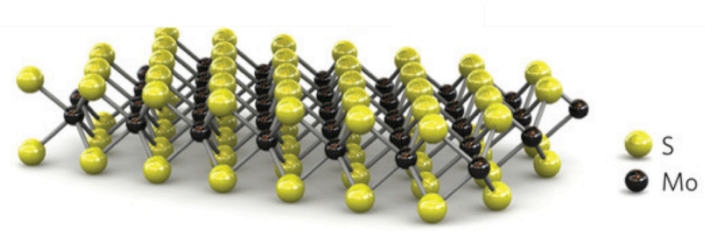


**Figure 1.6: The structure of $MoS_2$.** Adapted from [15]

Single layer $MoS_2$ is an intrinsic semiconductor with direct band-gap of 1.9 eV. Various electronic and optoelectronic studies have proven its potential as an active component for novel applications such as flexible, transparent, low-power electronic devices[15]. Furthermore, the discovery of valley polarization in single layer $MoS_2$ has proven its aptness for future valleytronic applications[40,41]. Recent advances in $MoS_2$ growth allow for uniform growth over wafer-scale[39,42], and pave the path for industrial applications.

## 1.3 Methods for Graphene Fabrication

### 1.3.1 Exfoliation of 2D Films

The initial discovery of graphene was enabled by a simple method of mechanical exfoliation of graphitic layers from a bulk crystal of highly ordered pyrolytic graphite (HOPG). The weak van der Waals forces between the graphite layers allow the layers to slide and separate from each other. This method is depicted in Figure 1.7a. It requires nothing more complicated than the application of a piece of scotch-tape onto the HOPG surface, an action that results in thin crystal pieces adhering to the tape.

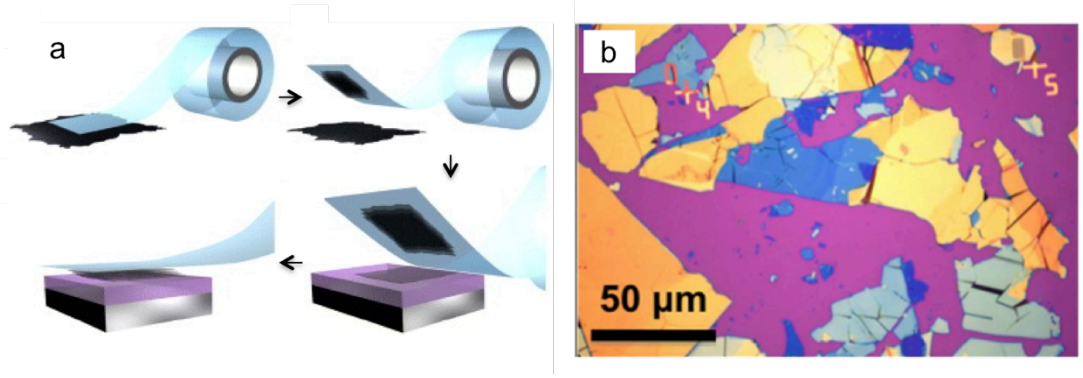


**Figure 1.7: Graphene exfoliation. a,** Illustration of the scotch-tape exfoliation method; scotch-tape is attached to the HOPG crystal, taking with it several graphite layers. It is then repeatedly attached to the $SiO_2$/Si substrate until the desired number of layers is achieved. Adapted from [27]. **b,** A typical optical microscope image of exfoliated graphene, displaying spatial inhomogeneity in the number of layers. Adapted from [43].

The scotch-tape is then repeatedly attached to a substrate – a thin $SiO_2$ film on a silicon wafer – each time shedding graphite layers onto the $SiO_2$ substrate. Several iterations of this process result in graphite layers of varying thicknesses, as can be seen in Figure 1.7b. By carefully choosing the $SiO_2$ thickness and the wavelength of incident light to enhance the contrast between the layers of different thicknesses[25], it

was possible to distinguish areas with few graphitic layer. This breakthrough enabled researchers to study the basic properties of few layer graphene[16], and to open up the field of 2D films for further exploration.

Many other 2D films have been isolated from their bulk crystal using the exfoliation method[38]. It is particularly useful for basic experiments combining one or more 2D material, as it can be done in an extremely clean manner, allowing for dirt-free adherence between two, or more, layers vertically[44]. It also allows for careful control over the placement of the 2D crystals, enabling fabrication of complex multilayer heterostructure devices[45–48], although without the ability to control their crystalline angle orientation.

### 1.3.2 Chemical Vapor Deposition

Unfortunately, the simple exfoliation method could not satisfy the size and scale requirements for research requiring large samples or large number of devices, or for industrial applications[17], and so several methods have been developed to obtain large-area graphene with greater throughput. Graphene synthesis by chemical vapor deposition (CVD) on copper (Cu) has emerged as one of the most convenient techniques to obtain high quality, single layer graphene, which can then be transferred onto arbitrary substrates using a simple etching process[49–53]. Furthermore, this method is scalable and has been used to produce films on meter length scales[4]. A schematic of the growth setup is shown in Figure 1.8a[54]. A typical growth recipe for preparing large-area, single layer graphene film is as follows[50]: Cu substrate is inserted into a CVD furnace, and exposed to a carbon source at a high temperature (*ca.* 1000 °C) in a

reducing environment. The resultant film is shown in Figure 1.8b. The graphene film is mostly uniform, except for a few wrinkles and small bilayer areas.

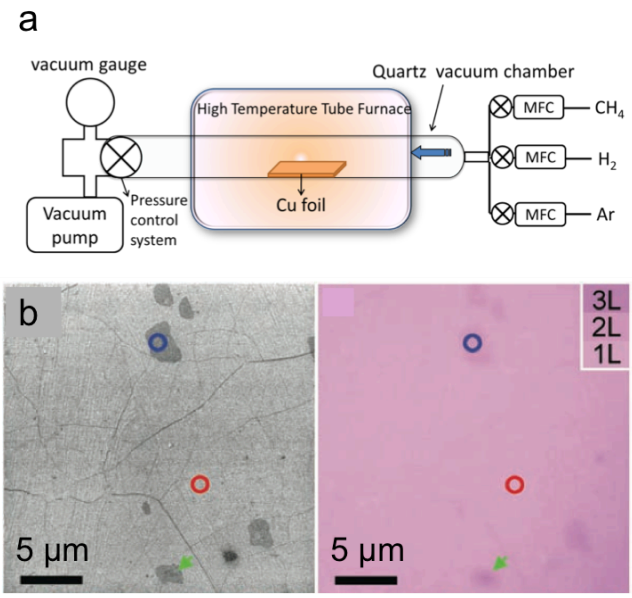


**Figure 1.8: Chemical vapor deposition of graphene. a,** Illustration of CVD tube furnace setup. Reproduced from [54]. **b,** Left: SEM image of graphene on the Cu foil substrate. The graphene film is mostly uniform (red circle), except for small dark multilayer areas (blue circle), and wrinkles which appear as thin dark lines. Right: the same area transferred onto a 300 nm $SiO_2$ substrate. Adapted from [50].

The CVD method can be easily adjusted to grow small grain or large grain graphene, and can selectively be tuned to produce one, two, or more layers by controlling the growth variables – time, temperature, choice of gases, and their concentration. These variations on the CVD process will be discussed in chapter 3.

An additional benefit of CVD graphene is the ease with which it can be transferred from its Cu growth substrate. In Figure 1.9 we show a roll-to-roll process developed to transfer large area graphene, up to 35 inches, onto plastic polyethylene terephthalate

(PET) sheets, and the flexible electronic devices that were fabricated using the graphene/PET film.

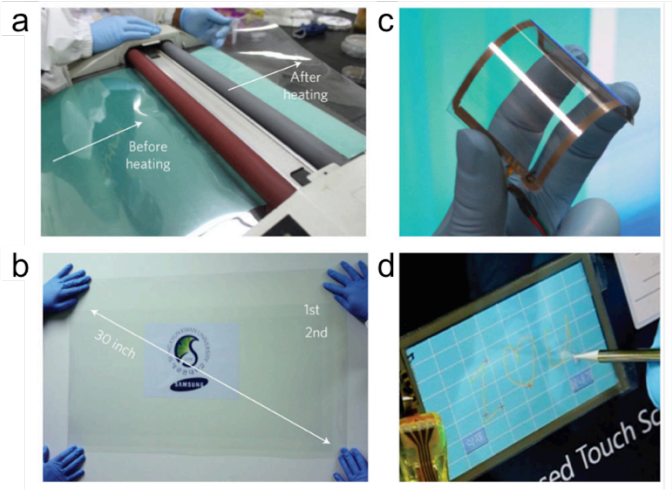


**Figure 1.9: Large-scale graphene transfer. a,** Roll-to-roll transfer of graphene films from a thermal release tape to a polymer (PET) film. **b,** A transparent large area graphene film transferred onto a 35-inch PET sheet. **c,** Assembled graphene/PET flexible touch panel. **d,** Graphene based touch-screen panel. Reproduced from [4].

Another common method, although not at the industrial scale, is the poly(methyl methacrylate) (PMMA) transfer method, where PMMA is spun on top of the graphene film in order to maintain its structural integrity while the Cu substrate is being etched, and later used to transfer the graphene onto the desired transfer before it is washed away.

### 1.3.3 Other Large-Scale Growth Methods

Large-scale graphene with high electronic performance (although not necessarily better than CVD grown graphene) can be grown epitaxially on silicon carbide (SiC) substrates[55,56]. Graphene is grown by exposing the SiC to high temperatures, *ca.*

1400°C, in vacuum, thus sublimating the Si atoms and leaving behind epitaxial graphitic surfaces. The growth rate is much lower for the Si-face of the SiC crystal, enabling the growth of few-layer graphene. The growth rate can be further controlled by limiting the Si sublimation rate through the introduction of Si gas or an inert gas (see Figure 1.10a,b**)**. Graphene multilayers grown on the Si-face are Bernal stacked, similar to graphitic stacking[57], whereas graphene grown on the C-face has turbostratic stacking, where the layers are randomly rotated with respect to each other, and electronically decoupled[58]. Graphene on SiC is mechanically coupled to the semiconducting SiC substrate, which renders its transfer process complicated and expensive[59]. Nonetheless, the graphene/SiC structure can be doped to electronically decouple the graphene from the substrate (Figure 1.10c)[60].

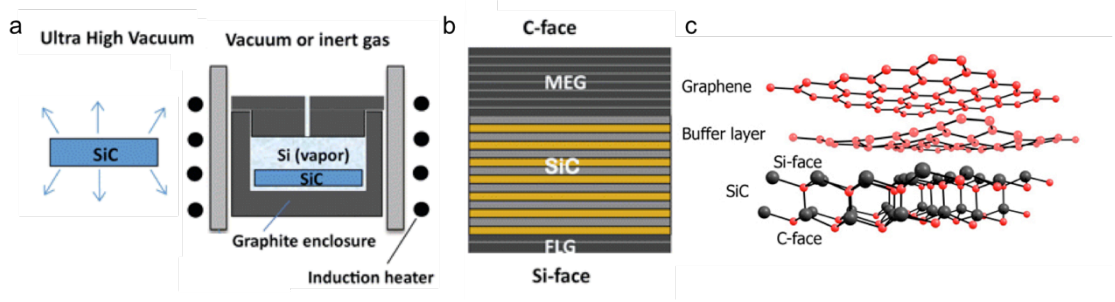


**Figure 1.10: Epitaxial graphene on SiC. a,** Two graphene growth modes on SiC. Left: high-vacuum growth with fast Si sublimation. Right: a growth setup that enables controlled sublimation rate. **b,** Ilustration depicting the consequence of the different growth rates on the C- and Si-faces. Adapted from [57]. **c,** Illustration of graphene on SiC, including a buffer layer between the graphene and the bulk SiC. Adapted from [61].

Despite its high quality, the widespread utilization of epitaxial graphene on SiC is hindered by the high cost of the SiC substrates, the high energy-cost of the

growth, the complicated transfer process, and the difficulty in obtaining uniform single-layer coverage.

In contrast, the self-assembly of graphene oxide (GO) sheets and their subsequent reduction into graphene platelets could provide a low-cost, water-soluble alternatives, as demonstrated in Figure 1.11[62]. These sheets can be assembled via large-scale chemical production methods, and be cast into a variety of forms[63,64]. Their applications include conductive inks for printable electronics, electrodes for solar cells[65], ultra-light graphene aerogel for energy applications[66], additives to ceramic and plastic materials enhancing their thermal and electronic properties, and more.


**Figure 1.11: Graphene oxide production and applications. a,** Centrifuge based isolation of few-layer graphene oxide platelets. Adapted from [63] **b,** scalable production of graphene platelets through liquid phase sheer exfoliation process. Adapted from [64]. **c,** compressible, lightweight graphene aerogel. Adapted from [66] **d,** graphene based transparent conducting electrode. **e,** graphene polymer composite. Adapted from [63].

Nonetheless, These films also tend to exhibit relatively poor electrical conductivity and varying optical properties, limiting their applications. Additionally, their casting methods produce multilayer stacks with limited control over the stacking order and number of layers, thus failing to take advantages of the unique benefits of few-layer graphene.

## 1.4 Bilayer and Trilayer Graphene

In this thesis we describe the fabrication of layered graphene stacks as a prototypical stacked 2D system. In these systems, variations in layer orientation and stacking order can induce distinct physical properties. For instance, bilayer graphene (BLG) in a graphite-like stacking (Bernal stacking) was shown to possess a tunable electronic bandgap (see figure Figure 1.12b)[67].

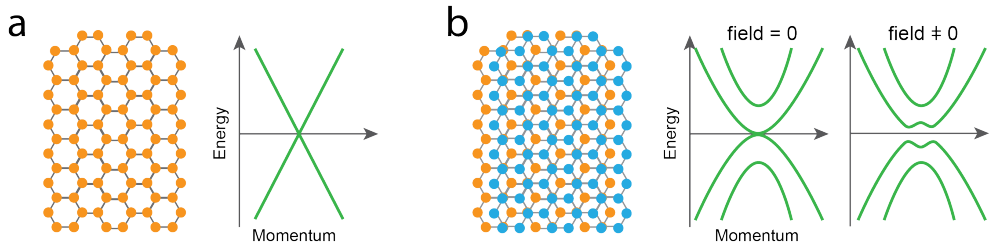


**Figure 1.12: Illustration of the physical and electronic structure SLG and Bernal Stacked BLG. a**, single layer and **b**, Bernal stacked bilayer graphene, and their electronic band structure near the K point. Single layer graphene has a linear band structure while Bernal stacked bilayer graphene has quadratic bands and a gap that opens under an applied vertical electric field. Adapted from [67].

At the same time, twisted bilayer graphene (tBLG) shows twist angle (θ) dependent optical and electronic properties[68,69]. This relative twist angle θ is a unique new degree of freedom, which provides exciting new opportunities for the creation of graphene stacks with predetermined properties. For example, the low-θ tBLG ($\theta < 6°$) system is a particularly interesting opportunity, as it is proposed to display new physical phenomena, yet does not exist in nature, nor is it thermodynamically preferred during growth. The low-θ tBLG system has been predicted to display fascinating new physics such as charge density waves, antiferromagnetism, and may

even display an exotic form of fermion-mediated superconductivity predicted for highly doped SLG[70,71]. Therefore, the ability to create bilayer graphene (BLG) or trilayer graphene (TLG) stacks with an arbitrary twist angle would allow us to systematically access the entire range of θ, including areas which were previously unavailable.

As mentioned above, two main challenges stand in the way of creating these structures. First, we must find ways to create these structures uniformly on large-scale. Second, we must understand their structure-related properties, both in order to ensure that the designed structures would exhibit the desired properties, and to assess the uniformity of the structure.

There are two possible approaches to the fabrication of angle-controlled layered graphene structures. They can be either (a) grown or (b) artificially assembled. The advantages of growing layered structures are clear; this approach would not require a layered transfer processes, and the resultant structures would be free of interlayer contaminants. Unfortunately, as-grown layered graphene suffer from inhomogeneity in both number of layers and the relative twist angle (θ) between the layers. This inhomogeneity will be further discussed in Chapter 4. The growth approach is also less compatible with the future incorporation of other types of 2D materials, as their growth conditions may vary and interfere with previously grown layers. The assembly approach constitutes of the growth of single layer sheets of graphene (SLG) with uniform angle distribution, which would then serve as building blocks for angle-controlled multilayer structures. This approach produces uniform

results over large scales, and enables the fabrication of structures that are rare in as-grown samples, as will be further discussed in Chapter 5.

It is possible to determine the structure of tBLG using transmission electron microscopy (TEM) techniques, which we will discuss in Chapters 2 and 4. This structural identification method is a useful independent measurement when we strive to understand the twist-angle dependent optical and electronic properties of tBLG, and can be done in conjunction with optical or electronic measurements.

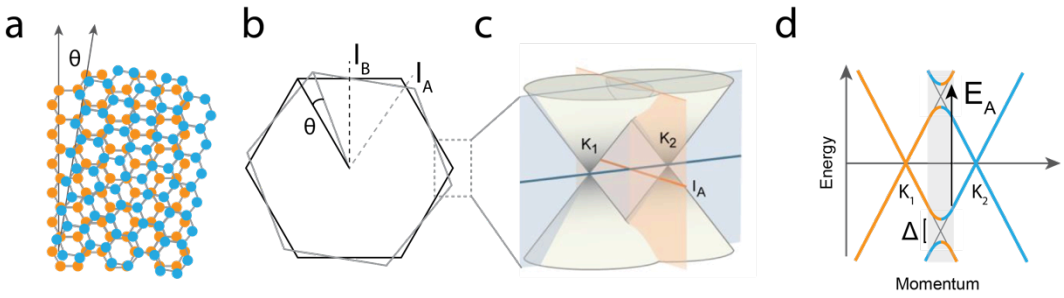


**Figure 1.13: Electronic properties of twisted bilayer graphene (tBLG). a**, Illustration of the physical structure of tBLG. **b**, two Brillouin zones corresponding to each graphene layer. The bands from each layer intersect at along lines $I_A$ and $I_B$. **c**, zoom-in of the area between the two Dirac cones. **d**, the band structure of tBLG along the blue line in (c). Minigaps with energy Δ are formed where the cones intersect. Allowed parallel band optical transitions with energy ~$E_A$ are marked with an arrow and highlighted in grey.

In order to understand the principles governing tBLG properties, it is essential to understand its electronic band structure. The band structure of tBLG can be approximated by the superposition of two single layer Brillouin zones twisted by θ with respect to each other, as can be seen in Figure 1.13b. The interaction at the intersection of the two twisted Brillouin zones leads to angle-dependent van Hove Singularities (vHS) in the density of states (DOS). The transition between the two vHS

has a characteristic energy $E_{A,}$ shown in Figure 1.13d. This transition is responsible to θ-dependent features in the optical and electronic response of tBLG. It can be observed experimentally in scanning tunneling spectroscopy (STS) experiments, like the one featured in Figure 1.14b. On the left a scanning tunneling microscopy (STM) image that shows a moiré pattern corresponding to a low-θ tBLG with θ = 1.79°. In the STS spectra to the right the vHS appear as two sharp peaks in the density of states, with an energy separation that corresponds to $E_A$.

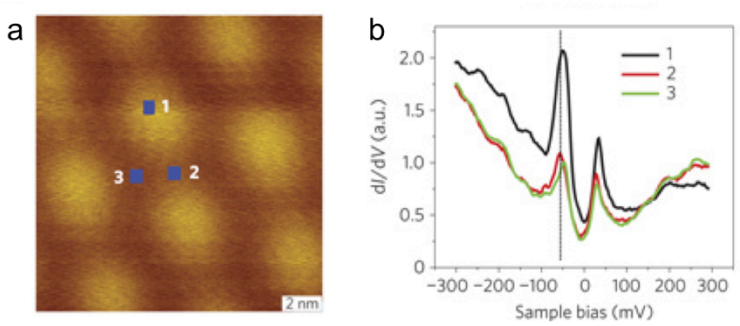


**Figure 1.14: Observation of vHS in low-θ tBLG.** a, STM image of tBLG showing a moire pattern corresponding to θ = 1.79°. b, STS spectra of the sample in (a), showing sharp peaks corresponding to the vHSs in the tBLG density of states. Adapted from [72]

Optically, tBLG exhibits a θ-dependent absorption peak, which serves as a useful tool in enabling optical identification of the twist angle between the layers[73], and will be further discussed in Chapter 2, section 2.2.3. θ-dependent resonant Raman scattering is another relevant phenomenon, which will also be discussed in chapter 2 [74,75]. As we progress in our ability to make more complex graphene stacks, we expect to discover new θ-dependent phenomenon in material realms that were not systematically accessible before, such as low-θ tBLG or chiral graphene stacks.

## 1.5 Summary and Outlook

In this chapter we introduced graphene, the first of an entire host of 2D crystalline materials. We discussed its properties, structure, methods of production, and its potential applications. While many applications of graphene as a stand-alone material have been suggested, the true potential of the field lies in creating intelligent combinations between various 2D materials[37]. This thesis will discuss the recent advances and remaining challenges pertaining to bilayer graphene system as a model system for 2D heterostructures. In **Chapter 2** we explore state-of-the-art imaging methods for probing the quality and structure of graphene layers, focusing on large-scale characterization methods. In **Chapter 3** we discuss current methods for synthesis and transfer of several types of CVD graphene, including large grains and bilayer graphene. We present a TEM imaging method in **Chapter 4,** for rapid and accurate determination of key structural parameters (twist angle, stacking order and interlayer spacing) of few-layer CVD graphene. We also discuss two kinds of strain-induced deformations, and develop an angle-dependent interlayer potential model. In **Chapter 5** we report the scalable growth of SLG aligned graphene and *h*-BN on copper foils, where each film originates from multiple nucleations yet exhibits a single orientation. Thorough characterization reveals uniform crystallographic and electronic structures on length scales ranging from nanometers to tens of centimeters. We then use these SLG building blocks to create artificial twisted graphene bilayers and characterize their angle-tunable optoelectronic properties. In **Chapter 6** we conclude our findings, and present several future directions that would be exciting continuation to this work. Two noteworthy topics are presented in the appendices; In **Appendix A** we present the

ability of CVD grown graphene films to protect the surface of the metallic growth substrates from air and liquid oxidation. This protection method offers significant advantages and can be used on any metal that catalyzes graphene growth. In **Appendix B** we report graphene-based in-plane heterostructures fabricated using a versatile and scalable process for creating high quality lateral heterojuntions in 2D materials, which we call 'patterned regrowth'. Patterned regrowth allows for the spatially controlled synthesis of lateral junctions between electrically conductive graphene and insulating *h*-BN, as well as between intrinsic and substitutionally doped graphene. We demonstrate the high quality of the resulting films and the mechanical continuity between these heterostructures.

# REFERENCES


1. Geim, A. K. & Novoselov, K. S. The rise of graphene. *Nat. Mater.* **6,** 183–91 (2007).

2. Novoselov, K. S. *et al.* A roadmap for graphene. *Nature* **490,** 192–200 (2012).

3. Zhu, Y., Sun, Z., Yan, Z., Jin, Z. & Tour, J. M. Rational design of hybrid graphene films for high-performance transparent electrodes. *ACS Nano* **5,** 6472–9 (2011).

4. Bae, S. *et al.* Roll-to-roll production of 30-inch graphene films for transparent electrodes. *Nat. Nanotechnol.* **5,** 574–8 (2010).

5. Park, H., Rowehl, J. A., Kim, K. K., Bulovic, V. & Kong, J. Doped graphene electrodes for organic solar cells. *Nanotechnology* **21,** 505204 (2010).

6. Parlak, O., Turner, A. P. F. & Tiwari, A. On/Off-switchable zipper-like bioelectronics on a graphene interface. *Adv. Mater.* **26,** 482–6 (2014).

7. Mann, J. A., Rodríguez-López, J., Abruña, H. D. & Dichtel, W. R. Multivalent binding motifs for the noncovalent functionalization of graphene. *J. Am. Chem. Soc.* **133,** 17614–7 (2011).

8. Cheng, R. *et al.* High-frequency self-aligned graphene transistors with transferred gate stacks. *Proc. Natl. Acad. Sci. U. S. A.* **109,** 11588–92 (2012).

9. Lin, Y.-M. *et al.* Operation of graphene transistors at gigahertz frequencies. *Nano Lett.* **9,** 422–6 (2009).

10. Graphene applications: Focus Issue. *Nat. Nanotechnol.* **9,** 725–868

11. Gan, X. *et al.* Chip-integrated ultrafast graphene photodetector with high responsivity. *Nat. Photonics* **7,** 883–887 (2013).

12. Li, X. *et al.* Stretchable and highly sensitive graphene-on-polymer strain sensors. *Sci. Rep.* **2,** 870 (2012).

13. Huang, L., Huang, Y., Liang, J., Wan, X. & Chen, Y. Graphene-based conducting inks for direct inkjet printing of flexible conductive patterns and their applications in electric circuits and chemical sensors. *Nano Res.* **4,** 675–684 (2011).

14. Ferrari, A. C. Science and technology roadmap for graphene, related two-dimensional crystals, and hybrid systems. *Nanoscale* **7,** 4598–4810 (2014).

15. Radisavljevic, B., Radenovic, A., Brivio, J., Giacometti, V. & Kis, A. Single-layer MoS2 transistors. *Nat. Nanotechnol.* **6,** 147–50 (2011).

16. Novoselov, K. S. *et al.* Electric field effect in atomically thin carbon films. *Science* **306,** 666–9 (2004).

17. Geim, A. K. Graphene: status and prospects. *Science* **324,** 1530–4 (2009).

18. Castro Neto, A. H., Peres, N. M. R., Novoselov, K. S. & Geim, A. K. The electronic properties of graphene. *Rev. Mod. Phys.* **81,** 109–162 (2009).

19. Lau, C. N., Bao, W. & Velasco, J. Properties of suspended graphene membranes. *Mater. Today* **15,** 238–245 (2012).

20. Balandin, A. A. Thermal properties of graphene and nanostructured carbon materials. *Nat. Mater.* **10,** 569–81 (2011).

21. Balandin, A. A. *et al.* Superior thermal conductivity of single-layer graphene. *Nano Lett.* **8,** 902–7 (2008).

22. Lee, C., Wei, X., Kysar, J. W. & Hone, J. Measurement of the elastic properties and intrinsic strength of monolayer graphene. *Science* **321,** 385–8 (2008).

23. Bunch, J. S. *et al.* Impermeable atomic membranes from graphene sheets. *Nano Lett.* **8,** 2458–62 (2008).

24. Chen, S. *et al.* Oxidation resistance of graphene-coated Cu and Cu/Ni alloy. *ACS Nano* **5,** 1321–7 (2011).

25. Nair, R. R. *et al.* Fine structure constant defines visual transparency of graphene. *Science* **320,** 1308 (2008).

26. Mak, K. F., Shan, J. & Heinz, T. F. Seeing Many-Body Effects in Single- and Few-Layer Graphene: Observation of Two-Dimensional Saddle-Point Excitons. *Phys. Rev. Lett.* **106,** 46401 (2011).

27. Novoselov, K. S. & Castro Neto, A. H. Two-dimensional crystals-based heterostructures: materials with tailored properties. *Phys. Scr.* **T146,** 014006 (2012).

28. Slotman, G. J. & Fasolino, A. Structure, stability and defects of single layer hexagonal BN in comparison to graphene. *J. Phys. Condens. Matter* **25,** 045009 (2013).

29. Blase, X., Rubio, A., Louie, S. G. & Cohen, M. L. Quasiparticle band structure of bulk hexagonal boron nitride and related systems. *Phys. Rev. B* **51,** 6868–6875 (1995).

30. Dean, C. R. *et al.* Boron nitride substrates for high-quality graphene electronics. *Nat. Nanotechnol.* **5,** 722–6 (2010).

31. Xue, J. *et al.* Scanning tunnelling microscopy and spectroscopy of ultra-flat graphene on hexagonal boron nitride. *Nature materials* **10,** 282–285 (2011).

32. Hunt, B. *et al.* Massive Dirac fermions and Hofstadter butterfly in a van der Waals heterostructure. *Science* **340,** 1427–30 (2013).

33. Kim, K. S. *et al.* Coexisting massive and massless Dirac fermions in symmetry-broken bilayer graphene. *Nat. Mater.* **advance on,** (2013).

34. Dean, C. R. *et al.* Hofstadter's butterfly and the fractal quantum Hall effect in moiré superlattices. *Nature* **497,** 598–602 (2013).

35. Kim, K. K. *et al.* Synthesis of monolayer hexagonal boron nitride on Cu foil using chemical vapor deposition. *Nano Lett.* **12,** 161–6 (2012).

36. Levendorf, M. P. *et al.* Graphene and boron nitride lateral heterostructures for atomically thin circuitry. *Nature* **488,** 627–32 (2012).

37. Geim, A. K. & Grigorieva, I. V. Van der Waals heterostructures. *Nature* **499,** 419–25 (2013).

38. Novoselov, K. S. *et al.* Two-dimensional atomic crystals. *Proc. Natl. Acad. Sci. U. S. A.* **102,** 10451–3 (2005).

39. Shi, Y., Li, H. & Li, L.-J. Recent advances in controlled synthesis of two-dimensional transition metal dichalcogenides via vapour deposition techniques. *Chem. Soc. Rev.* (2014). doi:10.1039/C4CS00256C

40. Mak, K. F., He, K., Shan, J. & Heinz, T. F. Control of valley polarization in monolayer MoS2 by optical helicity. *Nat. Nanotechnol.* **7,** 494–8 (2012).

41. Zeng, H., Dai, J., Yao, W., Xiao, D. & Cui, X. Valley polarization in MoS2 monolayers by optical pumping. *Nat. Nanotech.* **7,** 490–493 (2012).

42. K. Kang, S. Xie, L. Huang, Y. Han, P. Y. Huang, K. F. Mak, C.-J. Kim, D. A. Muller, J. P. High-mobility three-atom-thick semiconducting films with wafer scale homogeneity. *Submitted*

43. Kang, J., Shin, D., Bae, S. & Hong, B. H. Graphene transfer: key for applications. *Nanoscale* **4,** 5527–37 (2012).

44. Wang, L. *et al.* One-dimensional electrical contact to a two-dimensional material. *Science* **342,** 614–7 (2013).

45. Britnell, L. *et al.* Field-effect tunneling transistor based on vertical graphene heterostructures. *Science* **335,** 947–50 (2012).

46. Ponomarenko, L. A. *et al.* Tunable metal–insulator transition in double-layer graphene heterostructures. *Nat. Phys.* **7,** 958–961 (2011).

47. Haigh, S. J. *et al.* Cross-sectional imaging of individual layers and buried interfaces of graphene-based heterostructures and superlattices. *Nat. Mater.* **11,** 764–7 (2012).

48. Dean, C. *et al.* Graphene based heterostructures. *Solid State Commun.* **152,** 1275–1282 (2012).

49. Reina, A. *et al.* Large area, few-layer graphene films on arbitrary substrates by chemical vapor deposition. *Nano Lett.* **9,** 30–5 (2009).

50. Li, X. *et al.* Large-area synthesis of high-quality and uniform graphene films on copper foils. *Science* **324,** 1312–4 (2009).

51. Kim, K. S. *et al.* Large-scale pattern growth of graphene films for stretchable transparent electrodes. *Nature* **457,** 706–710 (2009).

52. Li, X. *et al.* Large-area graphene single crystals grown by low-pressure chemical vapor deposition of methane on copper. *J. Am. Chem. Soc.* **133,** 2816–9 (2011).

53. Mattevi, C., Kim, H. & Chhowalla, M. A review of chemical vapour deposition of graphene on copper. *J. Mater. Chem.* **21,** 3324 (2011).

54. Hu, Y. & Sun, X. in (ed. Aliofkhazraei, M.) (InTech, 2013). doi:10.5772/55666

55. Hass, J., de Heer, W. A. & Conrad, E. H. The growth and morphology of epitaxial multilayer graphene. *J. Phys. Condens. Matter* **20,** 323202 (2008).

56. Riedl, C., Coletti, C. & Starke, U. Structural and electronic properties of epitaxial graphene on SiC(0 0 0 1): a review of growth, characterization, transfer doping and hydrogen intercalation. *J. Phys. D. Appl. Phys.* **43,** 374009 (2010).

57. De Heer, W. A. *et al.* Large area and structured epitaxial graphene produced by confinement controlled sublimation of silicon carbide. *Proc. Natl. Acad. Sci. U. S. A.* **108,** 16900–5 (2011).

58. Sprinkle, M. *et al.* First Direct Observation of a Nearly Ideal Graphene Band Structure. *Phys. Rev. Lett.* **103,** 226803 (2009).

59. Kim, J. *et al.* Layer-Resolved Graphene Transfer via Engineered Strain Layers. *Science* **342,** 833–836 (2013).

60. Waldmann, D. *et al.* Bottom-gated epitaxial graphene. *Nat. Mater.* **10,** 357–60 (2011).

61. Jasper van den Berg, Eek Huisman , Wees, B. van. Epitaxial graphene. at <http://www.rug.nl/research/physics-of-nanodevices/research/graphene/epitaxial-graphene?lang=en.>

62. Dreyer, D. R., Park, S., Bielawski, C. W. & Ruoff, R. S. The chemistry of graphene oxide. *Chem. Soc. Rev.* **39,** 228–40 (2010).

63. Bonaccorso, F. *et al.* Production and processing of graphene and 2d crystals. *Mater. Today* **15,** 564–589 (2012).

64. Paton, K. R. *et al.* Scalable production of large quantities of defect-free few-layer graphene by shear exfoliation in liquids. *Nat. Mater.* **13,** 624–30 (2014).

65. Wang, X., Zhi, L. & Müllen, K. Transparent, conductive graphene electrodes for dye-sensitized solar cells. *Nano Lett.* **8,** 323–7 (2008).

66. Hu, H., Zhao, Z., Wan, W., Gogotsi, Y. & Qiu, J. Ultralight and highly compressible graphene aerogels. *Adv. Mater.* **25,** 2219–23 (2013).

67. Zhang, Y. *et al.* Direct observation of a widely tunable bandgap in bilayer graphene. *Nature* **459,** 820–3 (2009).

68. Mele, E. J. Commensuration and interlayer coherence in twisted bilayer graphene. *Phys. Rev. B* **81,** (2010).

69. Ohta, T. *et al.* Evidence for interlayer coupling and moiré periodic potentials in twisted bilayer graphene. *Phys. Rev. Lett.* **109,** 186807 (2012).

70. Nandkishore, R., Thomale, R. & Chubukov, A. V. Superconductivity from weak repulsion in hexagonal lattice systems. *Phys. Rev. B* **89,** 144501 (2014).

71. Nandkishore, R., Levitov, L. S. & Chubukov, A. V. Chiral superconductivity from repulsive interactions in doped graphene. *Nat. Phys.* **8,** 158–163 (2012).

72. Li, G. *et al.* Observation of Van Hove singularities in twisted graphene layers. *Nat. Phys.* **6,** 109–113 (2009).

73. Havener, R. W. *et al.* Hyperspectral imaging of structure and composition in atomically thin heterostructures. *Nano Lett.* **13,** 3942–6 (2013).

74. Havener, R. W., Zhuang, H., Brown, L., Hennig, R. G. & Park, J. Angle-Resolved Raman Imaging of Interlayer Rotations and Interactions in Twisted Bilayer Graphene. *Nano Lett.* **12,** 3162–3167 (2012).

75. Kim, K. *et al.* Raman Spectroscopy Study of Rotated Double-Layer Graphene: Misorientation-Angle Dependence of Electronic Structure. *Phys. Rev. Lett.* **108,** 22 (2012).

# CHAPTER 2

# IMAGING AND CHARACTERIZATION OF GRAPHENE

## 2.1 Introduction

The novelty of the two-dimensional (2D) class of crystalline materials necessitated the rapid development of new imaging methods. Imaging these materials is an essential component in the process of understanding their structure-property relations, as well as adapting them to industrial scale applications. Characterization of 2D materials is challenging due to their extreme thinness and transparency. These films are often structurally heterogeneous, containing many crystalline grains connected by grain boundaries, with locally varying number of layers. They require characterization over many length scales, from their macroscopic shape and polycrystalline structure down to their atomic structure. Rapid spatial characterization techniques are required to identify these parameters, and to determine the effect of the structural morphology on the electronic, optical, thermal, and mechanical properties of the film.

Standard bulk characterization methods, such as optical microscopy and scanning electron microscopy (SEM) can be useful for initial characterization, but fail to capture the complex crystalline structure of these 2D films. Fortunately, many microscopy and spectroscopy techniques have been developed to provide spatially resolved information about the structure of graphene[1]. In this chapter we will review the main methods available to examine the structure, quality and physical properties of graphene films with one, two, and three layers, and explore their related optical, electrical, and mechanical properties. The goal of this chapter is to provide an

overview of imaging methods that have been developed by many groups in the 2D community since the initial discovery of graphene in 2004. Many of these methods have become standard techniques for imaging graphene, and they include optical microscopy and spectroscopy, electron microscopy, scanning probe techniques, and other specialized methods. Many of these techniques were used extensively throughout this thesis, and will be mentioned in the following chapters.

We will also discuss specific techniques have been developed by our group and our collaborators, such as hyperspectral imaging, wide-field Raman, and dark-field transmission electron microscopy (DF-TEM). In a later chapter (Chapter 4) we will also introduce a dark-field TEM method we developed to explore the structure of bilayer and trilayer graphene.

In this chapter we will examine optical imaging techniques, such as bright field imaging of graphene to determine gross morphology and layer number, Hyperspectral absorption microscopy for heterostructures and bilayer structural analysis, and Raman spectroscopy and microscopy to determine the quality and structure of graphene films. We will also explore electron microscopy techniques, such as scanning electron microscopy (SEM) and back-scattered electron diffraction (BSED), used to image the gross structure of graphene layers and its crystalline copper substrate. We will discuss a variety of transmission electron microscopy (TEM), which are powerful techniques used to analyze the graphene structure on many length-scales. Finally, we will examine techniques such as angle-resolved photoemission spectroscopy (ARPES), used to measure graphene's band structure, and scanning methods such as atomic force microscopy (AFM), which probes structural and mechanical properties, and

scanning tunneling microscopy (STM), used to image graphene film's structure and electronic properties on the atomic scale.

Since these techniques provide distinctly different types of information, often a combination of these methods is required to establish the film's properties. We discuss these methods with regards to imaging few layer graphene, but many of these techniques have been successfully applied to *h*-BN and to other TMD materials.

## 2.2 Optical Microscopy Imaging

Direct optical microscopy techniques allow for rapid investigation of 2D films over millimeter, or even centimeter, scales. Some methods are easy to access, as many labs own optical microscopes, but the more advanced techniques, like wide-field Raman and hyperspectral imaging, require specialized setups. They tend to be quick, done in atmospheric conditions, often do not require special sample preparation, and are relatively easy to interpret. Nevertheless, they suffer from diffraction-limited spatial resolution, and usually do not provide information regarding the crystalline structure of the materials.

### 2.2.1 Direct Imaging on the Growth Substrate

Bright field (BF) optical microscopy imaging is especially useful for estimating the quality of the graphene directly after growth. For instance, partially grown graphene grains can be visualized directly on their copper (Cu) growth substrate by heating up the Cu foil in air up to 250 °C for 1 minute.

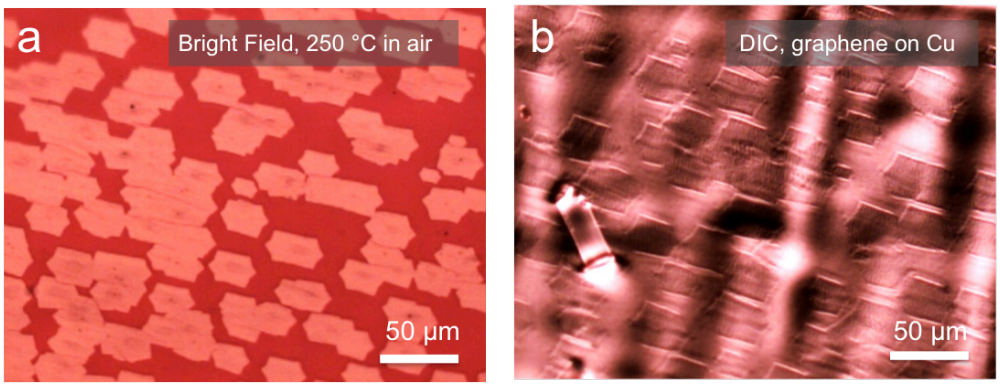


**Figure 2.1: Optical imaging of graphene on Cu. a,** Bright field image of partially grown graphene on Cu after heating to 250 °C in air for 1 minute. The bare Cu is visibly oxidized, while the protected Cu underneath the graphene remains intact. **b,** DIC image of partially grown graphene on Cu foil. Grain edges are visible without oxidation.

This process oxidizes the exposed Cu to a dull red copper oxide $(CuO)^2$, as seen in Figure 2.1a. The Cu underneath the graphene, which is protected from the oxygen in the air, remains bright, thus highlighting the shape of the graphene grains. Bilayer areas are also sometimes visible due to their raised ridge morphology, which increases light scattering, causing them to appear as dark spots in the center of some grains in Figure 2.1a.

Nevertheless, this method damages the Cu substrate, preventing complete removal of the Cu during graphene transfer, or its use as a growth substrate in subsequent growths. To resolve this, we found that differential interference contrast (DIC) is a useful non-destructive method for imaging partially grown graphene on Cu. DIC is sensitive to the path length of the light refracted from the sample, as well as to changes in the sample's refractive index. As seen in Figure 2.1b, DIC imaging highlights the graphene edges without oxidizing the copper surface. Both of these methods are mostly suitable to image partial growths rather than complete sheets.

### 2.2.2 Optical Imaging 2D Materials on Various Substrates

The ability to transfer graphene off graphite or its metallic growth substrate, and to subsequently determine it structure, is the cornerstone of the emerging field of 2D materials. In their groundbreaking 2004 study, Novoselov *et al*[3] successfully investigated the electronic properties of few layer graphene for the first time. They corroborate the thickness of graphene by depositing it on a $SiO_2$ substrate with a precise thickness, designed to enhance the contrast between individual graphene layers[4]. As can be seen in Figure 2.2, the combination of specific $SiO_2$ thicknesses and illumination wavelengths creates optimal conditions for enhancing the contrast difference between one, two, or more graphene layers. Since this calculation is based on the known optical parameters and geometry of graphene and $SiO_2$, it can be extended to different substrates and to other 2D materials.

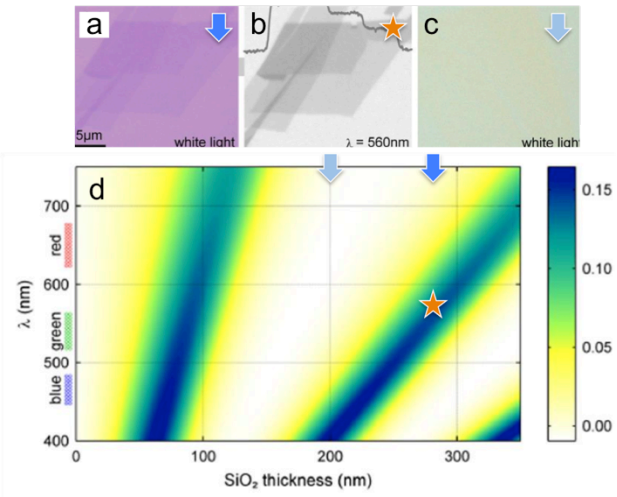


**Figure 2.2: Making graphene visible. a-b,** Graphene crystallites on 300 nm $SiO_2$ imaged with **a,** white light (denoted on the plot in (d) with a dark blue arrow) and **b,** green light (denoted on the plot in (d) with a star). In both cases graphene layers are visible, but the contrast in (b) is distinctly higher. **c,** Another graphene sample on 200 nm $SiO_2$ imaged with

white light, displaying low contrast (denoted on the plot in (d) with a light blue arrow). **d.** Wavelength vs. $SiO_2$ thickness plot illustrating the contrast (color scale) between graphene layers on $SiO_2$ substrates illuminated at different wavelengths. Adapted from [4].

While this method is extremely useful for the identification of the shape, size, and uniformity of graphene during device fabrication process, it does not provide information on the crystallographic properties of the film.

### 2.2.3 Hyperspectral Microscopy

Optical absorption microscopy, or DUV-Vis-IR hyperspectral microscopy, is a versatile imaging technique, used to distinguish between different 2D films by their absorption fingerprint[5]. This spatially resolved method is a powerful technique to analyze both the structure and composition of complex 2D heterostructures. Many different types of substrates can be used for hyperspetral imaging, as long as they comply with similar requirements to those detailed in section 2.2.2. Hence, this technique is compatible with other advanced imaging techniques such as SEM, TEM, and also enables concurrent electrical measurements. This technique measures the material's optical response over a broad range of energies – from the deep UV to the near IR. It is particularly useful in two cases; first, for the imaging of the relative twist angle (θ) in twisted bilayer graphene (tBLG) layers, and second, for imaging lateral heterostructures constructed with different 2D materials.

tBLG is a model layered heterostructure because of its strongly twist angle (θ) dependent optical properties, and because it can be found in CVD grown samples, or be created using transfer techniques. As described in Chapter 1, interlayer interactions in tBLG perturb the band structure to create θ-dependent van Hove singularities

(vHSs). As shown in Figure 2.3, these vHSs result in θ-dependent absorption peaks, which do not exist in monolayer graphene, or in Bernal stacked BLG.

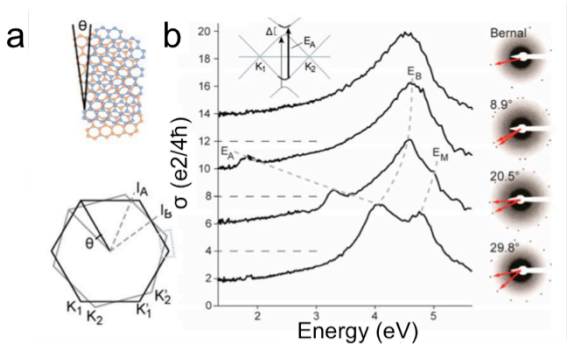


**Figure 2.3: The optical response of tBLG. a,** Schematic of tBLG (top) and rotated Brillouin zones of each tBLG layer (bottom). Adapted from [6]. **b,** Measured optical conductivity (σ) spectra of BLG (top) and tBLG with increasing θ. Dashed lines are guides to the eye indicating three features in the σ spectra of tBLG which are not found in BLG. Spectra are offset in σ by $4e^2/4\hbar$ for clarity. Inset: band structure sliced through Dirac cones of each layer. Allowed optical transitions are shown (arrows) at energies $E_A$. Adapted from [5].

The monotonic structure-property relationship shown in Figures 2.3-2.4 allows us to perform accurate, all-optical identification of θ in tBLG samples on opaque and transparent substrates[5]. This imaging method enabled the quantitative imaging of the interlayer interactions in tBLG, which includes many-body excitonic effects[6]. It provides better spatial of θ compared with the DF-TEM method (See section 2.4.2.3), but it is limited to investigate θ between $5° < \theta \leq 30°$.

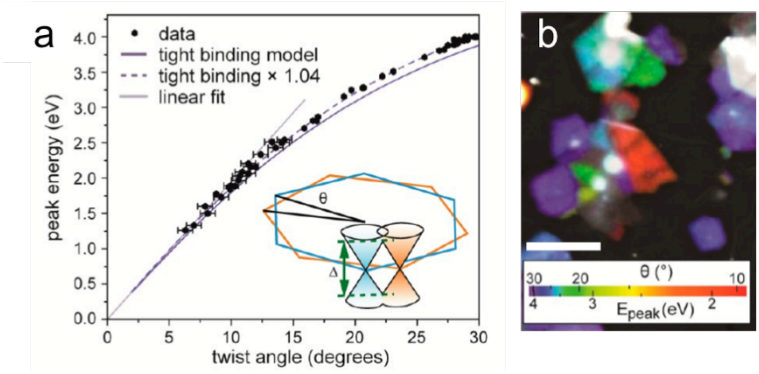


**Figure 2.4: Hyperspectral microscopy of tBLG. a**, Absorption peak energy ($E_{peak}$) versus θ measured for many tBLG domains showing a clear monochromatic relationship, along with fits for theoretical models developed in [5] and [6]. **b,** False color image of the resonance energies of many bilayer domains, illustrating the complex structure of tBLG grown by CVD.

The Hyperspectral imaging method is also useful for imaging the chemical composition and structure of devices combining two or more 2D materials. For example, it has been used to identify lateral structures in graphene/*h*-BN devices, shown in Figure 2.5[5]. Since the wavelength-dependent optical response is markedly different for graphene and *h*-BN (Figure 2.5b), a single measurement can distinguish between the two materials – as can be seen in Figure 2.5c, where a transmission measurement done at 6.1 eV reveals the highly absorptive (dark) *h*-BN flakes.

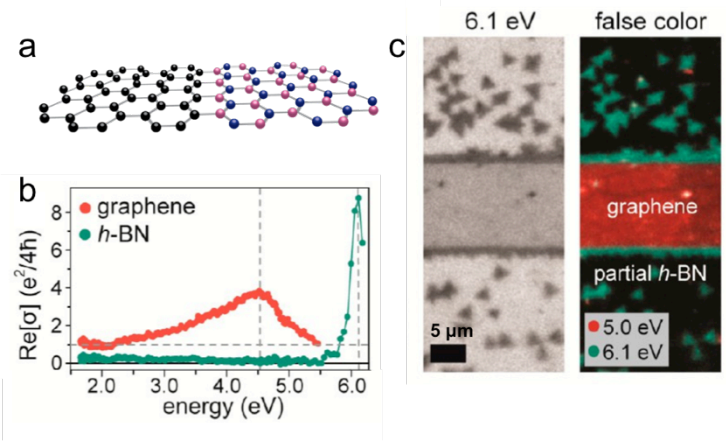


**Figure 2.5: Hyperspectral imaging for graphene and *h*-BN. a,** Illustration of a graphene/*h*-BN lateral junction. **b,** Absorption spectra for graphene and *h*-BN, showing a distinct peak for graphene at 4.6 eV, and a sharp peak for h-BN at 6.1 eV. **c,** Hyperspectral images of *h*-BN taken at 6.1 eV (left) and false colored hyperspectral image showing both *h*-BN and graphene. Adapted from [5].

Similar to other optical characterization techniques, this measurement can be done in ambient environment, and can be extended to measure the optical response of 2D materials under electric bias, complex layered 2D structures, and more. Nonetheless, this method is also diffraction limited, and can only reveal limited information on the atomic structure of heterjunctions.

## 2.3 Raman Spectroscopy and Wide-Field Raman

Raman spectroscopy is a powerful technique. It is sensitive to the phonon structure of the material, and can be used to estimate the quality of graphene films, as well as their doping, strain[7], number and stacking of layers[8], and more[9,10]. Typically, micro-Raman measurements are performed to examine random areas in a sample. However, in a method called wide-field Raman it is possible to image large areas in a short time by focusing on individual Raman bands using a filter[11]. Despite its popularity as a general method for identifying the quality and number of layers on graphene, Raman spectra

should be interpreted carefully, as the peak shifts and intensities are affected by variables such as choice of substrate and laser energy, making it difficult to compare results between different samples[12].

The Raman spectrum of graphene shows three main peaks. As can be seen in Figure 2.6a, single layer graphene displays sharp G (~1580 $cm^{-1}$) and 2D (~2700 $cm^{-1}$) bands, with a 2D/G ratio close to 2[13,14]. Defect density is indicated by the D (~1350 $cm^{-1}$)/G ratio[15], which is negligible for pristine single crystal graphene[16]. In Figure 2.6b we show that the 2D band frequency blue-shifts with increasing number of layers, and its intensity decreases, resulting in a 2D/G ratio close to, or lower than, 1.

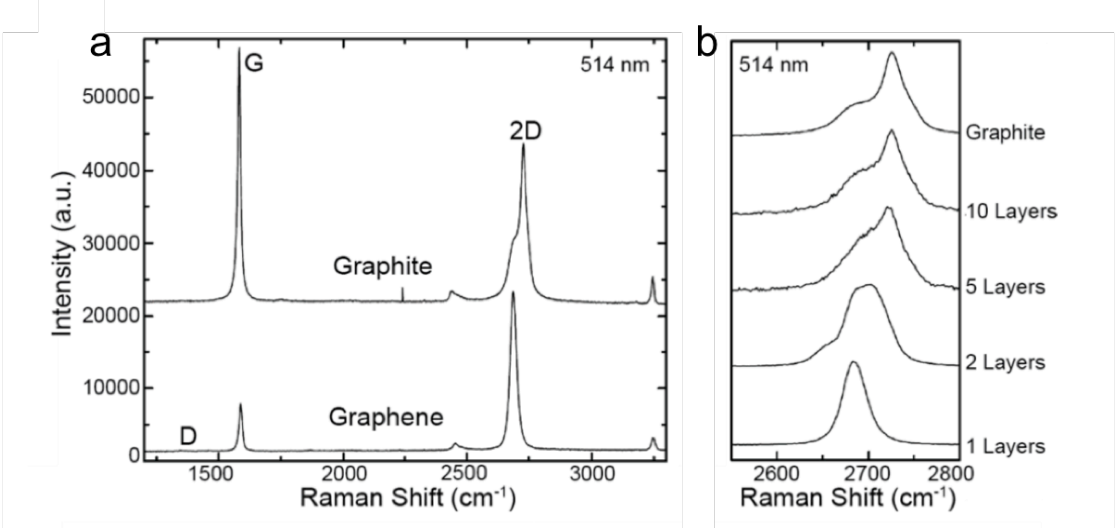


**Figure 2.6: Raman signature of graphene layers.** Left: spectra of graphene and graphite depicting the differences between them. One layer of graphene displays a sharp 2D peak, about twice the height of the G peak. Ideal graphene would show a very small D peak, which would grow in highly defected graphene. Right: the evolution of the 2D peak with number of layers. Reproduced from [16].

The micro-Raman setup, illustrated in Figure 2.7a, is useful in obtaining general information about the quality of the graphene layer, and can also be expanded

to a map by raster scanning the sample. Each map, however, requires long acquisition times (typically hours), and suffers from drift and resolution issues.

For this purpose, a 'wide-field' method can be used for imaging large areas of graphene in a short time[11], which is illustrated in Figure 2.7b. The sample is illuminated by a large, defocused laser spot, and the Raman scattered light is collected and filtered for a single Raman band. A large image is acquired using this setup, several hundreds of microns across, which represent the intensity of a single band (Figure 2.7c). The acquisition of several images for different bands enables large-area calculations of the ratio between the bands, quickly (several minutes per acquisition) and within diffraction limited resolution.

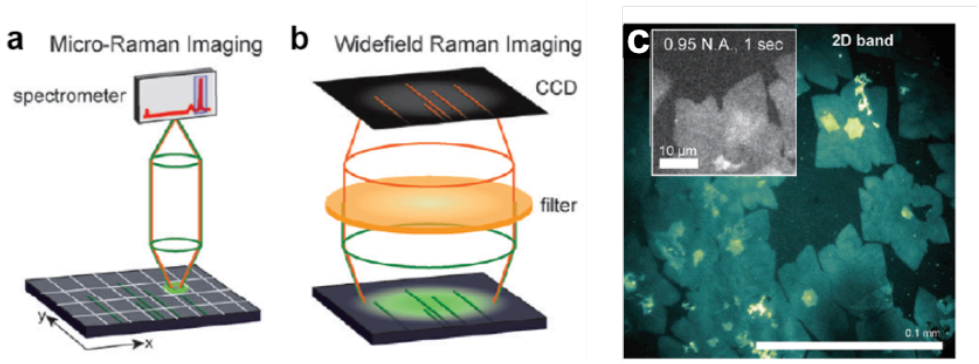


**Figure 2.7: Widefield Raman. a**, Illustration of conventional micro-Raman imaging, using a confocal geometry. **b**, Widefield Raman setup. **c**, False color image of the 2D-band for a sample of graphene using 20X objective. Inset: 100X objective. Reproduced from [11].

Widefield Raman can also be used to characterize the relative twist angle θ in twisted BLG. The vHSs created at the cone crossing (see Chapter 1 and Section 2.2.3 for more details) are responsible for θ-dependent G band enhancement[17] and for 2D band modifications[12]. Figure 2.8 shows wide-field Raman G band images of a bilayer

graphene area that contains several regions with different twist angles. Each image in Figure 2.8a shows the same region illuminated with different laser energy.

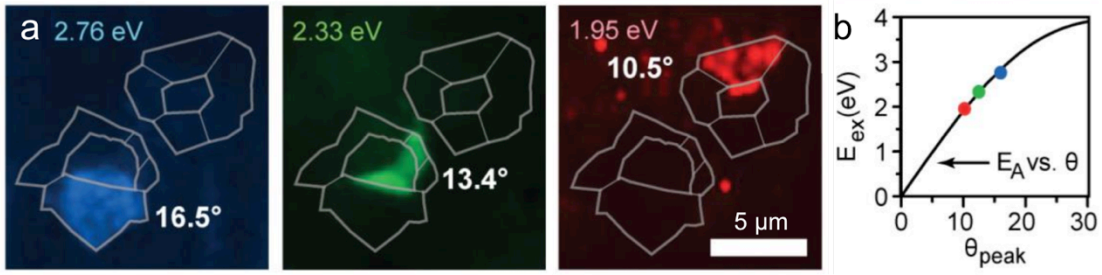


**Figure 2.8: θ-dependent Raman G-band enhancement in tBLG.** a, Widefield G-band images of the same tBLG regions (outlined) at three different excitation wavelengths. In each image, a different tBLG domain exhibits G-band enhancement. **b**, Excitation energy ($E_{ex}$) versus θpeak is plotted for each excitation wavelength, showing a clear monochromatic relationship. Adapted from [17].

Consequently, areas with different twist angles lights up in each of the three images. The correspondence between the twist angle and the incident laser energy is depicted in Figure 2.8b, and is similar to Figure 2.4a shown previously for optical absorption peaks. While this spatially-resolved Raman spectroscopy is sensitive to the presence of defects[10], number of layers[16], and their relative rotation[8,11,12] in graphene, it is limited as a twist angle characterization tool due to the monochromatic nature of the illuminating lasers.

## 2.4 Electron Microscopy Techniques

Electron microscopy (EM) techniques provide significantly increased resolution, while maintaining the ability to image 2D materials over large areas (up to several millimeters). These techniques can be used to image the morphology, crystalline structure, and chemical composition of 2D material, down to the atomic level. While

being widely used and extremely versatile, EM techniques are usually done in low-pressure (vacuum) conditions, making it challenging (but not impossible) to image liquid or biological samples. The high-energy electrons are also likely to damage biological samples, and in fact may damage the 2D films themselves[18].

### 2.4.1 Scanning Electron Microscopy

Scanning electron microscopy (SEM) is a commonly used method for micron-scale characterizing by scanning it with a focused electron beam. The electron beam produces several signals, including secondary electrons (SE), back-scattered electrons (BSE), X-rays, and cathodoluminescence photon (CL) signals, which reveal different information about the sample. Thanks to its large depth of field and high resolution, it can be used to image large areas, up to the centimeter scale, with sub-10 nm resolution. It can be used to image graphene directly on the Cu growth substrate (See Figure 2.9a-b), where graphene layers and folds are observed, as well as the morphology of the substrate, such as Cu steps and defects. It is also extremely useful in performing failure analysis on devices during the photolithography process. An SEM image of a suspended graphene device is shown in Figure 2.9c. SEM can be used to observe any conductive material, and it is available in most fabrication facilities. Nonetheless, SEM imaging does not provide information regarding the crystalline morphology of the 2D films.

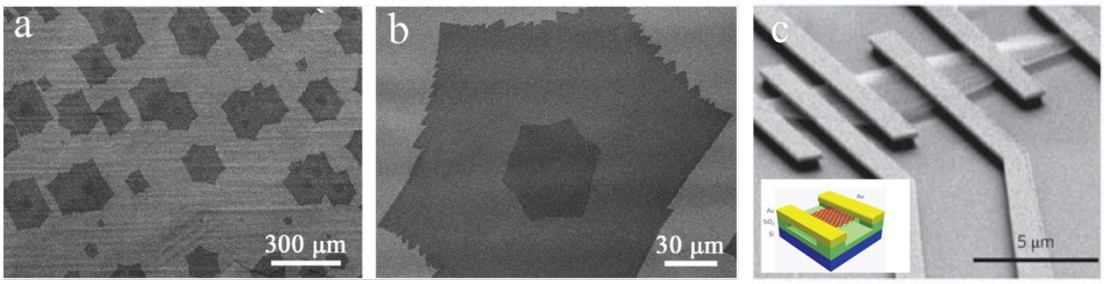


**Figure 2.9: Imaging graphene using SEM. a,** SEM image of partially grown graphene grains on Cu. **b,** A close-up on one of the graphene grains, showing the surrounding Cu surface, the leaf-like edges of the first layer, and the darker second layer. Adapted from [19]. **c,** SEM image of a suspended graphene device contacted by electrodes. Inset: illustration of device. Adapted from [20].

#### *2.4.1.1 Back-Scatter Electron Diffraction*

Some SEMs are equipped with a back-scatter electron diffraction (BSED) capability. This method is used to measure the surface crystallinity of the material, and is useful in determining the crystallinity of Cu films used to grow graphene and *h*-BN, since the substrate's crystalline orientation can have significant effect on the 2D film structure (more details on that in Chapter 5). The backscattered electrons reflected from a crystalline sample create distinct diffraction patterns, named "Kikuchi bands"[21] (see Figure 2.10a).

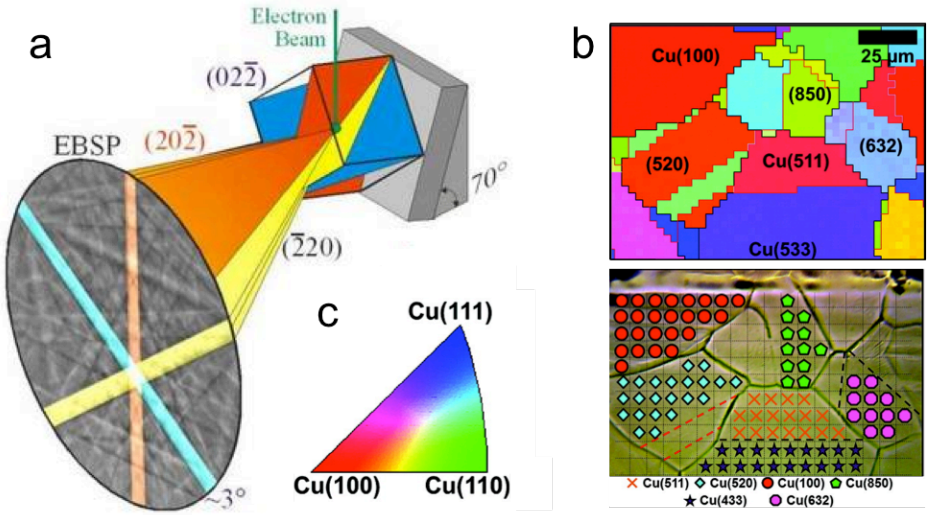


**Figure 2.10: Backscatter electron diffraction. a,** Electron interaction with bulk crystalline material, displaying Kikuchi bands that relate to the crystalline orientation in space. Adapted from [21]. **b,** Top: BSED map on crystalline Cu. Bottom: optical image of the Cu surface, matching crystalline orientation to Cu grain. **c,** Inverse pole figure (IPF) used to match the color in a BSED map (such as the map in (b)) to crystalline orientation. Adapted from [22].

The bands' frequency and orientation are determined by the crystal's lattice parameters, its orientation in space, the incident electron energy, and the sample's proximity to the detector. Thus, by using *a-priori* information regarding the sample, it is possible to extract not only the surface orientation of the sample, but also its in-plane rotation, which can be used to detect crystalline twinning. By further analyzing a series of point measurements, it is possible to create a map of the crystalline orientations on the sample's surface, as demonstrated on the polycrystalline surface of the Cu sample in Figure 2.10b.

### 2.4.2 Transmission Electron Microscopy

TEM imaging is based on passing a high-energy electron beam through thin samples, and observing the transmitted electron beam. This method is particularly useful for

characterizing 2D crystals as various TEM techniques provide information on the materials' structure and crystallinity down to the atomic level. By observing the parallel electron beam, the transmitted electron beam can provide information on the morphology of graphene, number of layers, tears, etc. By analyzing the location and relative intensity of the Bragg peaks that form when electrons diffract from an ordered surface, the sample's crystalline structure can be resolved[23,24]. In a method called scanning TEM (STEM), the beam can be converged to provide sub-Angstrom resolution, and scanned across the sample to provide atomic resolution imaging. Similar to SEM imaging, these techniques require vacuum conditions and mandate very clean samples. Additionally, they require special sample holders – TEM grids – making it challenging to combine these methods with standard photolithography processes. Low-resolution (down to 1 nm) TEM machines are not uncommon in research facilities, as they are often used for biological and material research. However, high resolution, aberration corrected TEMs are still rare, and it may be more difficult to gain access to those facilities. Special sample holders and TEM grids are available for a variety of imaging conditions, such as heating, cooling, electronic testing, and low-vacuum.

#### *2.4.2.1 High Resolution Transmission Electron Microscopy*

Aberration-corrected annular dark-field scanning transmission electron microscopy (ADF-STEM) provides unrivaled atomic-scale images of the 2D lattice, as can be seen in the atomic resolution image of single layer *h*-BN in Figure 2.11a. The image contrast reflects two parameters, the (local) atomic number, and the sample's

thickness. Hence, a brighter area represents a thicker sample, or the presence of a heavier atom. ADF-STEM additionally provides a method for precise determination of the elemental identity of each atom, as seen in Figure 2.11b. In this image boron and nitrogen atoms are identified as part of the original lattice, as well as carbon and oxygen substitutes. This method was used to image *h*-BN[25], graphene and graphene grain boundaries,[26,27] $MoS_2$[28], and much more.

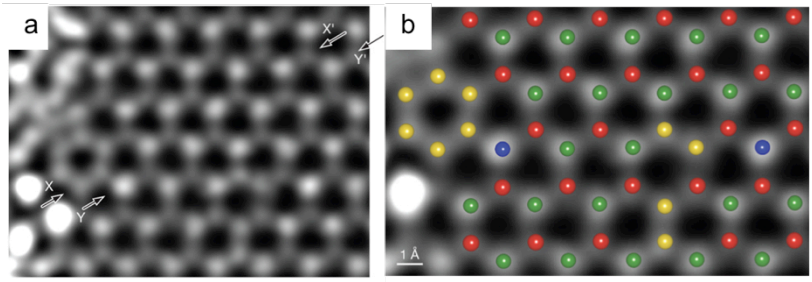


**Figure 2.11: High resolution STEM imaging of 2D lattices. a,** Deconvolved STEM image of single layer *h*-BN. **b,** Overlaid elemental atomic identification on part of the image in (a). Red= Boron; yellow=Carbon; green=Nitrogen; blue=Oxygen. Adapted from [25].

However, this method is unfit for imaging large areas as it is slow and requires long acquisition times to image a sample even on the micron scale. Additionally, it requires a lengthy sample preparation procedure with low sample yield.

#### *2.4.2.2 Atomic Chemical Mapping*

Both STEM and TEM can be used to obtain chemical information on the sample, using electron energy loss spectroscopy (EELS) and energy dispersive X-ray (EDX)[29]. Both measurements are based on the incident electron beam's interaction with the sample's core electrons. An incident electron can excite core electrons by transferring some of its energy. The excited electron leaves behind it an empty core state, which is

almost immediately filled by a conduction band electron. This transition emits X-ray with an energy equal to the energy difference of this transition.

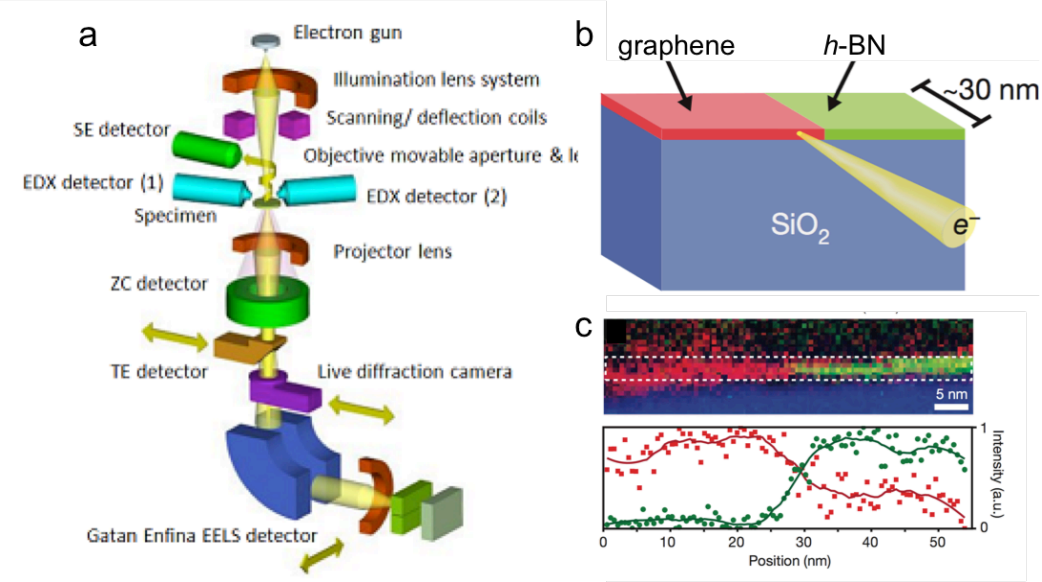


**Figure 2.12: Chemical analysis in TEM imaging. a,** Schematic for EELS and EDX detectors. Adapted from[30]. **b,** Illustration of the 2D junction between graphene and *h*-BN. **c,** Top: EELS data showing the elemental map of the graphene/*h*-BN junction region containing graphitic carbon (red; g-C), boron (green), and oxygen (blue). Bottom: intensity profile of g-C and boron, indicating no voids or overlap in the junction region. Adapted from [31].

EELS detects energy loss of the emitted electrons, while EDX detects the energy of the emitted X-rays. Both measurements can determine the sample's chemical composition by the characteristic energy levels for each element. Both methods can be done concurrently with STEM/TEM measurements (and EDX with SEM) (see Figure 2.12), and can provide spatially resolved chemical information with nanometer or atomic resolution. EDX can be used to detect many chemical elements at the same time, while EELS has smaller energy dispersion, enabling the detection of few elements at a time, but a better spectral resolution and so it can provide

information regarding the nature of the chemical bond. In Figure 2.12b-c we demonstrate an EELS analysis done on the atomic interface of a 2D junction between graphene and *h*-BN (see Appendix B for details on this work), showing an abrupt transition between the two 2D materials.

#### *2.4.2.3 Dark Field Transmission Electron Microscopy*

TEM possesses the capability to image in a configuration that is sensitive to electron diffraction. This imaging mode, named dark-field TEM (DF-TEM), is a robust method to image the different grain orientations in CVD graphene over large areas with high throughput.[26] The technique is also widely available, as it can be implemented even on microscopes that do not possess atomic resolution. This method had been used to observe the polycrystalline structure of CVD graphene[26], *h*-BN[32], and $MoS_2$[28].

The mechanism of DF-TEM can be understood from the top panels of Figure 2.13. Figure 2.13a, shows a typical TEM image of CVD graphene fully suspended on top of a hole, which exhibits almost no contrast differences across the sheet. The selected area electron diffraction (SAED) pattern from this area, however, shows many sets of six-fold-symmetric spots (Figure 2.13b). This diffraction pattern implies that the area contains many distinct graphene crystals. In order to image this area in a dark-field mode, a small aperture is placed in the diffraction plane to collect only the electrons passing through it (denoted by a circle), thereby selectively imaging the graphene domains diffracting in this small range of angles (Figure 2.13c). By repeating this process with several different aperture positions, the images are

colorized and overlaid together to generate complete maps of the domain structure in this area (Figure 2.13e and f).

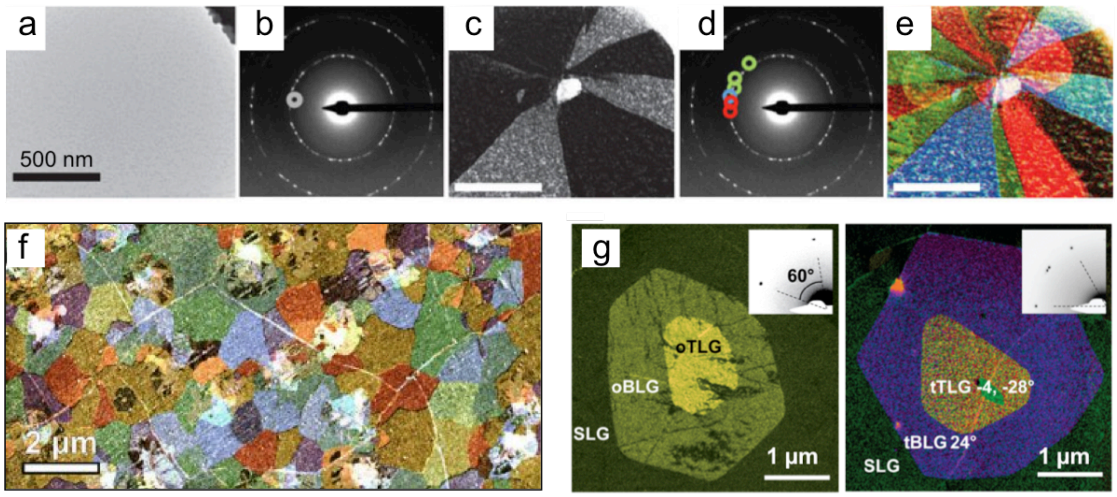


**Figure 2.13: DF-TEM imaging of polycrystallinity in Graphene. a-e**, DF-TEM process for characterization of graphene grain structure, resulting in **f**, a color-coded large-scale image of various crystals in the graphene sheet. Adapted from [26]. **g,** DF-TEM images of multi-layer regions with Bernal (left) and twisted (right) stacking. Inset shows the corresponding diffraction patterns. Adapted from [33].

DF-TEM can also be used to determine the stacking orientations in multi-layered CVD graphene[33]. The left panel of Figure 2.13g, shows three layers of graphene, which can be easily distinguished by their relative dark-field intensities. Since their combined electron diffraction pattern only contains one set of six-fold symmetric spots (inset), this indicates that the lattices of all the graphene layers are rotationally aligned. In contrast, the three distinct sets of diffraction spots in the right panel indicate that all three layers are misoriented. The relative intensities of the DF-TEM images and their corresponding SAED patterns offer a wealth of information regarding the precise atomic stacking of the graphene layers. In Chapter 4 we describe

how a combination of DF-TEM and SEAD data can be used to determine the structure and interlayer interaction of oriented and twisted bilayer and trilayer graphene.

### 2.4.3 Low Energy Electron Diffraction and Microscopy

Low-energy electron diffraction (LEED) is a surface sensitive technique, used to characterize the crystalline surface structure. Similar to transmission electron diffraction, the surface crystal structure determination can be accomplished by analyzing the location and intensity of the Bragg peaks. The inelastic mean free path for low energy (~100 eV) electron is on the order of 1 nm[34], which makes this method sensitive only to the first few layers in the material. This property makes LEED an excellent method for probing 2D materials, and their interactions with their substrate, simultaneously, as shown in Figure 2.14a and b. For example, LEED can be used to determine the relative orientation of graphene and its substrate *in situ*[35]. While LEED usually only provides diffraction data averaged over large (~3 mm) areas, low energy electron microscopy (LEEM) can be used to provide crystalline information with high resolution, often *in situ* inside the growth chamber[36] (see Figure 2.14c, d).

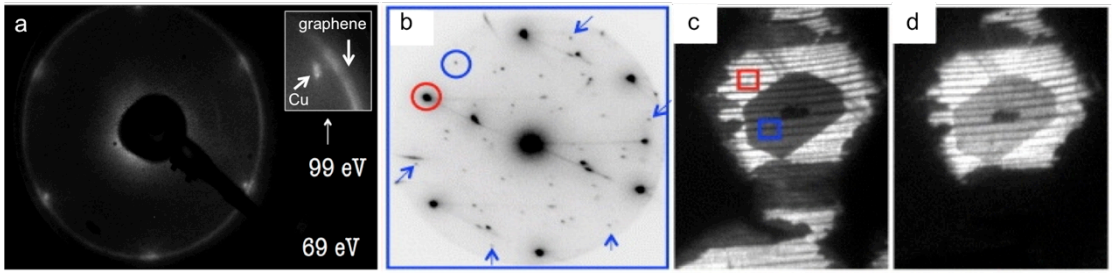


**Figure 2.14: Imaging graphene with LEED and LEEM. a,** LEED diffraction pattern from polycrystalline graphene (outer ring) on Cu(111) surface (six bright spots). Adapted from [37]. **b,** Selected-area LEED from a bilayer graphene region showing two sets of diffraction spots in red and blue. **c,** Bright field LEEM image of the bilayer area and **d,** Dark field LEEM image of the area in (c) highlighting the single layer region, taken with an aperture on the red circle in (b). Adapted from [38].

LEEM has been used to resolve graphene thickness variation, domain structure, layer spacing and stacking[38], and has been helpful in advancing our understanding of graphene growth process. In our experiments in Chapter 5, LEED is frequently used prior to ARPES experiments, in order to assess the sample's cleanliness, its crystalline uniformity and relative orientations. Nonetheless, LEED has limited spatial and spectral resolutions, and both measurements require extremely clean sample surfaces.

## 2.5 Angle Resolved Photoemission Electron Spectroscopy

Angle Resolved Photoemission Electron Spectroscopy (ARPES) is a unique measurement technique for a material's momentum-resolved electronic band structure[39]. The measurement consists of sample illumination by a monochromatic light source (10 – 900 eV), and a subsequent analysis of the energy and momentum of electrons emitted from it due to the photoelectric effect. ARPES can be used to measure a material's band structure below the Fermi level (mostly valence band), hence a sample must be heavily doped to image the conductance band.

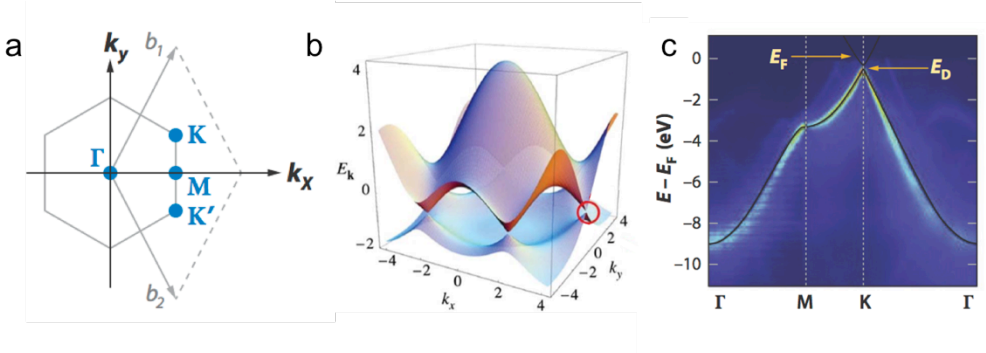


**Figure 2.15: Imaging graphene band structure with ARPES. a,** Graphene Brilliouin zone, showing the Γ, K, and M high symmetry points. **b,** Illustration of graphene's energy vs. momentum band structure plot, highlighting the Dirac cone at the K point. Adapted from [40]. **c,** APRES valence band spectra, showing the Dirac cone at the K point. Adapted from [41].

ARPES has been used to directly image the electronic structure of graphene near the Dirac cones[41], and can even reach up to the M-point with significant doping[42]. It can be used to detect interlayer coupling[43], and other properties such as Fermi velocity, band shape, alignment with the substrate, and more. Furthermore, by employing spatially resolved ARPES, it can be used to explore the electronic homogeneity of the sample[37]. In Figure 2.15c we show graphene ARPES displaying cuts along Γ-K, Γ-M, and M-K directions, which correspond to the graphene calculated band structure in Figure 2.15b.

In Figure 2.16 we show an ARPES measurement of a twisted bilayer graphene sample, showing the two rotated Dirac cones in Figure 2.16b, as well as direct evidence for the existence of a vHs near the avoided crossing between the two cones (red arrow, Figure 2.16c).

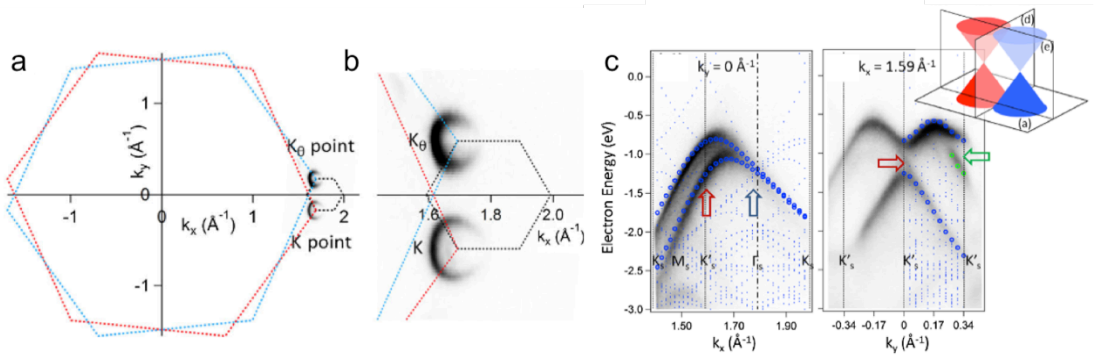


**Figure 2.16: Imaging tBLG band structure with ARPES. a,** schematics of tBLG rotated Brilliouin zone of each layer. **b,** zoom-in of the two K points form each layer. **c,** valence band spectra perpendicular and parallel to the intersection between the Dirac cones, cut directions shown in the inset. Red arrow points to the avoided crossing between the cones. Adapted from [43].

While this method is extremely useful for direct imaging of a material's band-structure, it is limited to probing only the areas below the Fermi level. Additionally, it requires a conductive substrate, extreme sample cleanliness, and access to ARPES imaging facilities.

## 2.6 Scanning Probe Techniques

Scanning probe techniques, such as atomic force microscopy (AFM) and scanning tunneling microscopy (STM), are based on the principle of investigating the interaction of a small probe with the sample's surface as it raster scans the sample. AFM can probe atomic height of the surface in the z-direction, as well as mechanical and electrical properties, while STM can probe the atomic structure of the surface, as well as its electronic properties. Both of these techniques rely on a feedback mechanism, thus limiting their speed and the areas they can probe, making them well suited for small area measurements – on the micron scale or smaller. While AFM measurements can be done in ambient conditions on almost any type of surface, STM

studies requires extreme sample cleanliness and may take a long time to map areas larger than a micron.

### 2.6.1 Atomic Force Microscopy

In tapping mode AFM a small, oscillating cantilever is brought in direct gentle contact with the sample's surface, thus dampening its oscillations. The cantilever then scans the sample while maintaining a fixed oscillation amplitude.

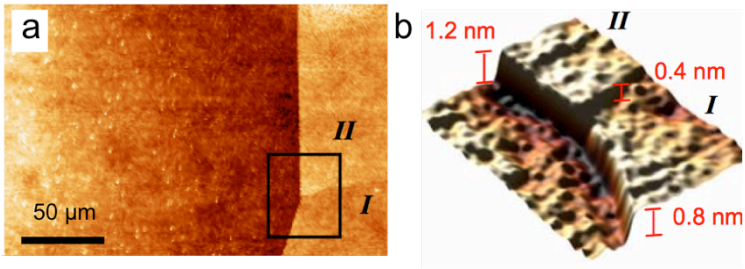


**Figure 2.17: AFM imaging of graphene. a,** graphene on SiO2 substrate **b,** 3D rendering of the highlighted area in (a), showing fixed height increase per layer, except for the transition between $SiO_2$ and graphene. Adapted from [44]

Changes in the surface morphology or physical properties cause the tip to shift in the z direction, and thus provide sub-nanometer information on the sample's height. A variety of AFM modes provide information on the structural, electronic, and mechanical properties of graphene[45]. AFM can be used to determine the number of graphene layers[44], giving a value of ~0.4 nm per layer (single layer graphene thickness is 0.35 nm). However, the difference in the tip-substrate interactions renders the height value between the $SiO_2$ substrate and the graphene inaccurate.

### *2.6.1.1 Mechanical Properties Investigation with AFM*

Mechanical information on the breaking strength of suspended sheets can be obtained by suspending graphene on top of small holes, and performing nanoindentation measurements using the AFM tip (Figure 2.18a). Such studies done on single-crystal, exfoliated graphene revealed an exceptionally strong material with a high elastic modulus (≈1 TPa) and large breaking force (≈2 μN) (Figure 2.18b)[46]. This is largely a reflection of the strength of carbon-carbon bonds, the same concept that has previously motivated the use of carbon fibers to mechanically reinforce composite materials.

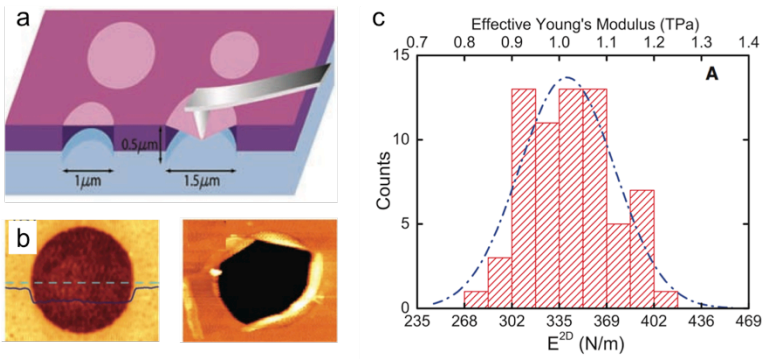


**Figure 2.18: Mechanical properties of graphene. a,** Schematic of nanoindentation measurements. **b,** AFM images of suspended graphene (left) and of a ruptured graphene membrane after maximal load (right). **c,** Histograms of elastic stiffness of mechanically-exfoliated graphene. Adapted from [46].

For polycrystalline graphene, indentation measurements performed on CVD graphene films revealed both their elastic modulus and breaking force to be consistently reduced by an order of magnitude from that of exfoliated graphene (Figure 2.19)[47].

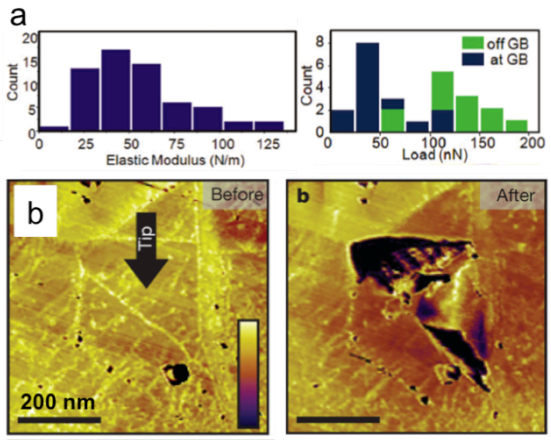


**Figure 2.19: Mechanical properties of graphene grain boundaries. a,** Histograms of elastic stiffness of CVD graphene (left), and breaking loads on and off the grain boundary (right), showing lower loads at the GB. **b,** AFM images before and after nanoindentation showing that tears occurred along the grain boundaries. Adapted from [26].

While the softening of graphene's stiffness was attributed to the presence of ripples in the film, its breaking strength was severely weakened by its polycrystallinity. In fact, as shown in Figure 2.19b, CVD graphene was often observed to tear precisely along its grain boundaries[26].

### 2.6.2 Scanning Tunneling Microscopy

In STM imaging, a voltage bias is applied between a conductive, atomically sharp tip and a conductive surface[48,49]. As the tip approaches a few Angstrom from substrate tunneling current is measured and used as a feedback signal. In constant current mode (CCM) the tip raster-scans the sample while keeping a constant current, and so vertical displacements of the tip reflect the surface topography, providing a sub-atomic resolution image of the local density of states (LODS). Alternately, the tip can also be parked in one location and measure the current as a function of changing bias, in a

method called scanning tunneling spectroscopy (STS), thus probing the energy dependence of the LDOS.

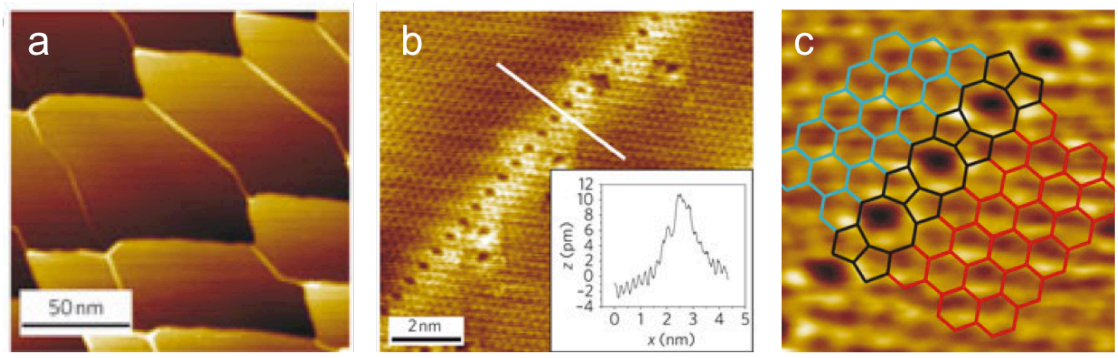


**Figure 2.20: Imaging graphene using STM. a,** STM image of graphene on Ni(111) showing the ridge structure. **b,** Line defect with image profile in the direction perpendicular to the wire (inset). **c,** Defect structure and superimposed defect model. Adapted from [49]

STM had been used to image the atomic structure of graphene on its growth surface and graphene grain boundaries, as can be seen in Figure 2.20, as well as the structure of local dopants[50], charge puddles in graphene[51], and the structure of graphene on *h*-BN[52]. Particularly relevant for this work, STM has been used to probe interlayer interactions in bilayer graphene[48], demonstrating the presences of vHs in small twist angle samples, and the graphene-Cu interaction in Cu(111) and Cu(100) surfaces[53]. Nonetheless, STM can only be used to probe the combined LDOS of the graphene and its substrate together, which in turn creates challenges in de-convolving the electronic structure of graphene alone.

## 2.7 Conclusion

In this chapter we examined several methods used to image graphene on many length scales. Optical imaging methods – such as bright field microscopy and Raman

spectroscopy – are well suited for fast, centimeter scale characterization. More advanced methods, such as hyperspectral imaging and widefield Raman provide more information regarding the chemical and structural identity of the films, but still suffer from diffraction-limited resolution. Electron microscopy techniques provide much higher resolution. SEM can image stacks of graphene and graphene devices in high resolution over large areas, as well as provide information regarding the crystallinity of the metal growth substrate. TEM methods can provide unique data regarding the sample's crystallinity and chemical and atomic structure, but require specialized, ultra thin substrates. Finally, scanning probe methods can provide unparalleled information regarding the sample's topography and atomically resolve electronic structure. Specifically, dark-field TEM imaging for bilayer and trilayer graphene and hyperspectral microscopy imaging were developed as a part of this thesis, and are particularly useful tools in imaging the structure of layered graphene stacks.

REFERENCES


1. Tsen, A. W., Brown, L., Havener, R. W. & Park, J. Polycrystallinity and stacking in CVD graphene. *Acc. Chem. Res.* **46,** 2286–96 (2013).

2. Chen, S. *et al.* Oxidation resistance of graphene-coated Cu and Cu/Ni alloy. *ACS Nano* **5,** 1321–7 (2011).

3. Novoselov, K. S. *et al.* Electric field effect in atomically thin carbon films. *Science* **306,** 666–9 (2004).

4. Blake, P. *et al.* Making graphene visible. *Appl. Phys. Lett.* **91,** 063124 (2007).

5. Havener, R. W. *et al.* Hyperspectral imaging of structure and composition in atomically thin heterostructures. *Nano Lett.* **13,** 3942–6 (2013).

6. Havener, R. W., Liang, Y., Brown, L., Yang, L. & Park, J. Van Hove singularities and excitonic effects in the optical conductivity of twisted bilayer graphene. *Nano Lett.* **14,** 3353–7 (2014).

7. Mohiuddin, T. *et al.* Uniaxial strain in graphene by Raman spectroscopy: G peak splitting, Grüneisen parameters, and sample orientation. *Phys. Rev. B* **79,** 205433 (2009).

8. Lui, C. H. *et al.* Imaging stacking order in few-layer graphene. *Nano Lett.* **11,** 164–9 (2011).

9. Ferrari, A. C. & Basko, D. M. Raman spectroscopy as a versatile tool for studying the properties of graphene. *Nat. Nanotechnol.* **8,** 235–46 (2013).

10. Malard, L. M., Pimenta, M. A., Dresselhaus, G. & Dresselhaus, M. S. Raman spectroscopy in graphene. *Phys. Rep.* **473,** 51–87 (2009).

11. Havener, R. W. *et al.* High-throughput graphene imaging on arbitrary substrates with widefield Raman spectroscopy. *ACS Nano* **6,** 373–80 (2012).

12. Kim, K. *et al.* Raman Spectroscopy Study of Rotated Double-Layer Graphene: Misorientation-Angle Dependence of Electronic Structure. *Phys. Rev. Lett.* **108,** 22 (2012).

13. Reina, A. *et al.* Large area, few-layer graphene films on arbitrary substrates by chemical vapor deposition. *Nano Lett.* **9,** 30–5 (2009).

14. Li, X. *et al.* Large-area synthesis of high-quality and uniform graphene films on copper foils. *Science* **324,** 1312–4 (2009).

15. Tuinstra, F. Raman Spectrum of Graphite. *J. Chem. Phys.* **53,** 1126 (1970).

16. Ferrari, A. C. *et al.* Raman Spectrum of Graphene and Graphene Layers. *Phys. Rev. Lett.* **97,** 187401 (2006).

17. Havener, R. W., Zhuang, H., Brown, L., Hennig, R. G. & Park, J. Angle-Resolved Raman Imaging of Interlayer Rotations and Interactions in Twisted Bilayer Graphene. *Nano Lett.* **12,** 3162–3167 (2012).

18. Meyer, J. C. *et al.* Accurate Measurement of Electron Beam Induced Displacement Cross Sections for Single-Layer Graphene. *Phys. Rev. Lett.* **108,** 196102 (2012).

19. Shi, Y. G. *et al.* Fabrication of single-crystal few-layer graphene domains on copper by modified low-pressure chemical vapor deposition. *CrystEngComm* **16,** 7558 (2014).

20. Chen, C. *et al.* Performance of monolayer graphene nanomechanical resonators with electrical readout. *Nat. Nanotechnol.* **4,** 861–7 (2009).

21. Wilkinson, A. J., Dingley, D. J. & Meaden, G. Electron Backscatter Diffraction in Materials Science. *Electron Backscatter Diffr. Mater. Sci.* 345–360 (2009). doi:10.1007/978-0-387-88136-2

22. Wood, J. D., Schmucker, S. W., Lyons, A. S., Pop, E. & Lyding, J. W. Effects of polycrystalline cu substrate on graphene growth by chemical vapor deposition. *Nano Lett.* **11,** 4547–54 (2011).

23. Kotakoski, J. & Meyer, J. Mechanical properties of polycrystalline graphene based on a realistic atomistic model. *Phys. Rev. B* **85,** 5 (2012).

24. Meyer, J. C. *et al.* The structure of suspended graphene sheets. *Nature* **446,** 60–3 (2007).

25. Krivanek, O. L. *et al.* Atom-by-atom structural and chemical analysis by annular dark-field electron microscopy. *Nature* **464,** 571–4 (2010).

26. Huang, P. Y. *et al.* Grains and grain boundaries in single-layer graphene atomic patchwork quilts. *Nature* **469,** 389–92 (2011).

27. Kim, K. *et al.* Grain boundary mapping in polycrystalline graphene. *ACS Nano* **5,** 2142–6 (2011).

28. Van der Zande, A. M. *et al.* Grains and grain boundaries in highly crystalline monolayer molybdenum disulphide. *Nat. Mater.* **12,** 554–61 (2013).

29. Wei Wang, Xing Wu, and Jian Zhang, ". Graphene and Other 2D Material Components Dynamic Characterization and Nanofabrication at Atomic Scale. *J. Nanomater.* **2015,**

30. Photo Gallery | Quantitative Bioelemental Imaging Center. at <http://qbic.facilities.northwestern.edu/photo-gallery/>

31. Levendorf, M. P. *et al.* Graphene and boron nitride lateral heterostructures for atomically thin circuitry. *Nature* **488,** 627–32 (2012).

32. Kim, C.-J. *et al.* Stacking order dependent second harmonic generation and topological defects in h-BN bilayers. *Nano Lett.* **13,** 5660–5 (2013).

33. Brown, L. *et al.* Twinning and twisting of tri- and bilayer graphene. *Nano Lett.* **12,** 1609–15 (2012).

34. Seah, M. P. & Dench, W. A. Quantitative electron spectroscopy of surfaces: A standard data base for electron inelastic mean free paths in solids. *Surf. Interface Anal.* **1,** 2–11 (1979).

35. Wofford, J. M., Nie, S., McCarty, K. F., Bartelt, N. C. & Dubon, O. D. Graphene Islands on Cu Foils: The Interplay between Shape, Orientation, and Defects. *Nano Lett.* **10,** 4890–4896 (2010).

36. Man, K. L. & Altman, M. S. Low energy electron microscopy and photoemission electron microscopy investigation of graphene. *J. Phys. Condens. Matter* **24,** 314209 (2012).

37. Avila, J. *et al.* Exploring electronic structure of one-atom thick polycrystalline graphene films: a nano angle resolved photoemission study. *Sci. Rep.* **3,** 2439 (2013).

38. Nie, S. *et al.* Growth from Below: Bilayer Graphene on Copper by Chemical Vapor Deposition. (2012). at <http://128.84.158.119/abs/1202.1031?context=cond-mat>

39. Lu, D. *et al.* Angle-Resolved Photoemission Studies of Quantum Materials. *Annu. Rev. Condens. Matter Phys.* **3,** 129–167 (2012).

40. Castro Neto, A. H., Peres, N. M. R., Novoselov, K. S. & Geim, A. K. The electronic properties of graphene. *Rev. Mod. Phys.* **81,** 109–162 (2009).

41. Bostwick, A., Ohta, T., Seyller, T., Horn, K. & Rotenberg, E. Quasiparticle dynamics in graphene. *Nat. Phys.* **3,** 36–40 (2006).

42. McChesney, J. L. *et al.* Extended van Hove Singularity and Superconducting Instability in Doped Graphene. *Phys. Rev. Lett.* **104,** 136803 (2010).

43. Ohta, T. *et al.* Evidence for interlayer coupling and moiré periodic potentials in twisted bilayer graphene. *Phys. Rev. Lett.* **109,** 186807 (2012).

44. Zhang, Y., Tan, J. W., Stormer, H. L. & Kim, P. Experimental observation of the quantum Hall effect and Berry's phase in graphene. *Nature* **438,** 201–204 (2005).

45. Bertolazzi, S. *et al.* Exploring Flatland: AFM of mechanical and electrical properties of graphene, MoS2 and other low-dimensional materials. *Microsc. Anal.* 21–24 (2013).

46. Lee, C., Wei, X., Kysar, J. W. & Hone, J. Measurement of the elastic properties and intrinsic strength of monolayer graphene. *Science* **321,** 385–8 (2008).

47. Ruiz-Vargas, C. S. *et al.* Softened elastic response and unzipping in chemical vapor deposition graphene membranes. *Nano Lett.* **11,** 2259–63 (2011).

48. Li, G. *et al.* Observation of Van Hove singularities in twisted graphene layers. *Nat. Phys.* **6,** 109–113 (2009).

49. Lahiri, J., Lin, Y., Bozkurt, P., Oleynik, I. I. & Batzill, M. An extended defect in graphene as a metallic wire. *Nat. Nanotechnol.* **5,** 326–9 (2010).

50. Zhao, L. *et al.* Local atomic and electronic structure of boron chemical doping in monolayer graphene. *Nano Lett.* **13,** 4659–65 (2013).

51. Zhang, Y., Brar, V. W., Girit, C., Zettl, A. & Crommie, M. F. Origin of spatial charge inhomogeneity in graphene. *Nat. Phys.* **5,** 722–726 (2009).

52. Woods, C. R. *et al.* Commensurate–incommensurate transition in graphene on hexagonal boron nitride. *Nat. Phys.* **10,** 451–456 (2014).

53. Zhao, L. *et al.* Influence of copper crystal surface on the CVD growth of large area monolayer graphene. *Solid State Commun.* **151,** 509–513 (2011).

# CHAPTER 3

# GRAPHENE GROWTH AND TRANSFER

## 3.1 Introduction

A world-wide effort is underway for the development of new and improved methods for growing graphene on metal substrates[1–5]. Initially, the studies of graphene's intrinsic properties were reported by using small, mechanically-exfoliated graphene crystals found randomly, as described in Chapter 1. However, exploiting graphene's unique properties for many scientific and technological applications requires the growth of large-area graphene films with uniform structural and physical properties, which can then be easily transferred to other substrates. Chemical vapor deposition (CVD) techniques have been successfully applied for the purpose of growing high quality single and multilayer graphene onto various metal substrates, including single-layer graphene (SLG) growth on Cu[4,6], Pt[7], and Ir[8], and multilayer growth on Ni[2,9] and Ru[10]. In general, these graphene films are polycrystalline, consisting of multiple graphene crystals joined by grain boundaries. In addition, portions of these single layer films contain multilayer regions, and each layer may possess a different crystal orientation. In this review chapter we will explore how changes in the growth parameters can affect the growth dynamics and the final graphene structures. These parameters include growth substrate, time, temperature, pressure, gas choice, gas concentrations, and ratios between different gases. Considering the purpose of creating large-scale, angle uniform bilayer graphene stacks, we will explore growth methods for several types of graphene sheets. We will present the growth of single layer and

bilayer graphene, as well as graphene with large grains. In Chapter 5 we will expand upon this knowledge, and present our own growth method for single layer graphene with single-crystal-like alignment on the centimeter scale. We will also touch here on the effects of the growth dynamics on the electronic and mechanical properties of graphene sheets. Finally, we will discuss methods of transferring graphene off of its growth substrate and onto a variety of scaffolds for further imaging and device fabrication.

## 3.2 Single Layer Graphene Growth on Copper Substrates

Graphene can be grown on a variety of metallic and insulating surfaces. Cu is an ideal substrate for uniform single layer graphene growth using CVD, due to its low carbon solubility[5], as well as its low cost and wide availability. Other metals, such as Ni[1], Ru[10], Ir[8], Pt[11], Co[12,13], Pd[14], and Re[15] have also been used for CVD growth, but they entail high substrate costs, or suffer from high carbon solubility.

Graphene grown on Cu substrates was shown to grow by a surface adsorption mechanism (see Figure 3.1a), which limits its coverage to a few atomic layers, and assists in controlling the graphene morphology through control over the Cu crystallinity, as will be further discussed in Chapter 5. Graphene grown on substrates with higher carbon solubility, such as Ni, grows by a surface precipitation mechanism (see Figure 3.1b), where the carbon atoms diffuse into the metal, graphene platelets are created underneath the surface, and diffuse back onto the Ni surface, which results in a random multilayer structure. A general recipe for growing SLG was reported by Li *et al*[4]. First, a Cu substrate is inserted into a tube furnace and heated to a high

temperature. Since graphene can only grow on an oxide-free Cu surface, the Cu substrate is first annealed at a hydrogen ($H_2$) environment for approximately 1 hour in order to reduce the inherent surface copper oxide (CuO) layer. Following anneal, graphene is grown in a methane ($CH_4$)/$H_2$ environment for 10 minutes. Once the growth is finished, the Cu foil is cooled and extracted. Growth temperature ranges from 650 °C to above 1000 °C, depending on the substrate of choice and the carbon source used[2,4,6–10,16,17].

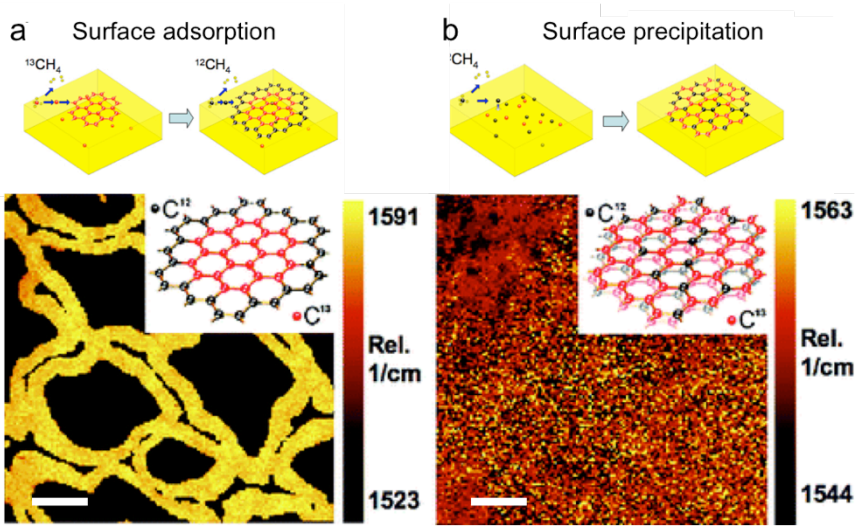


**Figure 3.1: CVD graphene growth mechanisms. a,** Single layer graphene grown on Cu surface via carbon surface adsorption (top), as seen in this carbon isotope labeled Raman image (bottom), where time-dependent isotope flow leads to a radially patterned graphene. **b,** multilayer graphene grown on Ni surface via carbon dissolution and precipitation (top), which produces a mixed isotope Raman image (bottom). Scale bars are 5 μm. Adapted from [5].

Many carbon containing materials, such as methane gas[4], poly-methyl-methilacrilate (PMMA)[18], and even sugar[19], have been used to create graphene. Graphene can also be grown directly on insulating substrates such as sapphire, *h*-BN,

$SiO_2$, $Si_3N_4$, and $Al_2O_3$, a beneficial process enabling electrical device fabrication without transfer.

The growth method described above is a relatively 'fast' growth, where graphene is synthesized on Cu foil with a high concentration of methane gas, leading to high nucleation density and rapid growth. This forms a continuous, mostly single layer (>95%) graphene film with small (~1 μm) graphene crystals in random crystalline orientations, and atomically stitched grain boundaries (see Figure 3.2) [20,21]. Despite the high frequency of grain boundaries, often cited as a potential cause for significantly increasing electron scattering and thus decreasing electron mobility, these films have been reported to still have excellent electrical properties, with field effect mobility up to 250,000 $cm^2/Vs$ for suspended SLG graphene at 1.5K, on par with exfoliated graphene samples[22].


**Figure 3.2: Small grain graphene growth on Cu. a,** SEM image of graphene on Cu, showing mostly uniform single layer, with some darker bilayer patches. **b,** dark-field TEM image of the grain structure of a similarly grown graphene film, where each color represents a different crystalline orientation. **c,** High resolution STEM image of a grain boundary in this type of growth, showing perfect atomic stitching. Adapted from [23].

Their mechanical properties, however, such as elastic modulus and breaking force, are sometimes reduced compared with exfoliated samples. Their softening is attributed to the presence of wrinkles created due to the rough Cu substrate[24], while

the breaking force is reduced due to the presence of defects at the grain boundaries. Notably, graphene has been shown to break along grain boundaries[20], thus weakening the overall film. Nonetheless, CVD graphene can exhibit comparable strength and stiffness to exfoliated samples, but this requires careful transfer and processing to avoid rippling and damage[25].

### 3.3 Large Grain Graphene

Many groups have been working towards developing a growth methods aimed at achieving large graphene grains. Theoretically, the inherent properties within a single crystalline domain could reach the quality of exfoliated graphene, and not be compromised by the existence of grain boundaries[26,27]. In order to increase the graphene grain size, two growth mechanisms must be controlled – the nucleation density and the growth rate[28]. Current literature could be grouped into two approaches, the first focuses on limiting precursor concentration, and the second focuses on limiting nucleation sites; The first method limits both nucleation density and growth rate by reducing the concentration of the carbon precursor[29]. Nucleation is first suppressed by annealing the substrate for several hours in an $H_2$ environment, thus reducing surface steps and defects, which function as nucleation sites[30]. The growth is then performed in an ultra-low methane concentration, allowing for the growth to last for several hours. This growth can yield graphene grains of several hundred microns, and even up to several millimeters, as shown in Figure 3.3a-b.

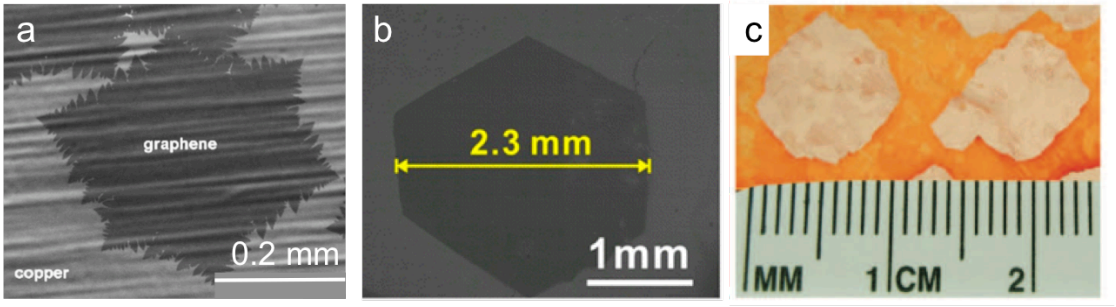


**Figure 3.3: Large grain graphene growth. a,** Large graphene flakes grown using precursor limiting method. Reproduced from [29], **b,** This method can be used to grow flakes up to several millimeters. Reproduced from [31] . **c,** Centimeter sized grains grown using nucleating limiting method. Reproduced from [32]

The second method reduces the nucleation density by intentionally creating a CuO layer prior to the start of the growth[32,33]. Since graphene can only grow on the Cu substrate, a low flow of methane and $H_2$ simultaneously etches the CuO surface and creates nucleation sites at a low density, down to 4 $cm^{-2}$, as can be seen in Figure 3.3c. Both methods allow for growth of extremely large graphene grains, often visible by eye.

While the shape of these grains may appear like a single crystal, they often contain several distinct crystalline domains, as well as small bilayer areas, as can be seen in Figure 3.4. It appears that grain boundaries in this 'slow' growth are not as robust as the 'fast' growth described above. Mechanically, they are either overlapped, or display incomplete stitching, as shown in Figure 3.5.

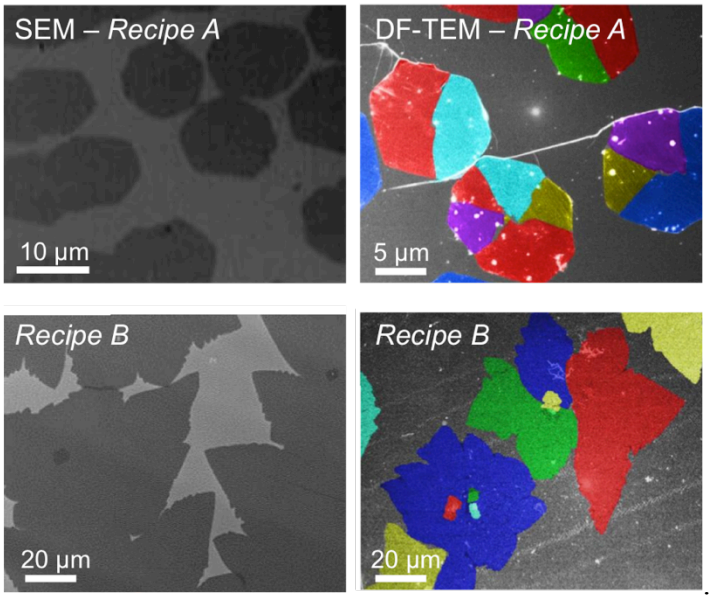


**Figure 3.4: Crystallinity in large graphene grains.** Left: SEM images of two different large grain graphene growths, and their respective DF-TEM image on the right. These DF-TEM images reveal that even areas that might be considered a 'single' crystal under SEM can still have multiple crystalline orientations.

While the electronic properties within one grain are excellent[32], grain boundaries in large grain growths tend to significantly increase resistance and reduce electron mobility due to poor stitching quality as seen in Figure 3.5[23,34]. Unfortunately, the atomic structure of these grain boundaries is difficult to investigate, since the yield of suspended samples is very low, probably due to their poor inter-grain stitching demonstrated in Figure 3.5a-b.

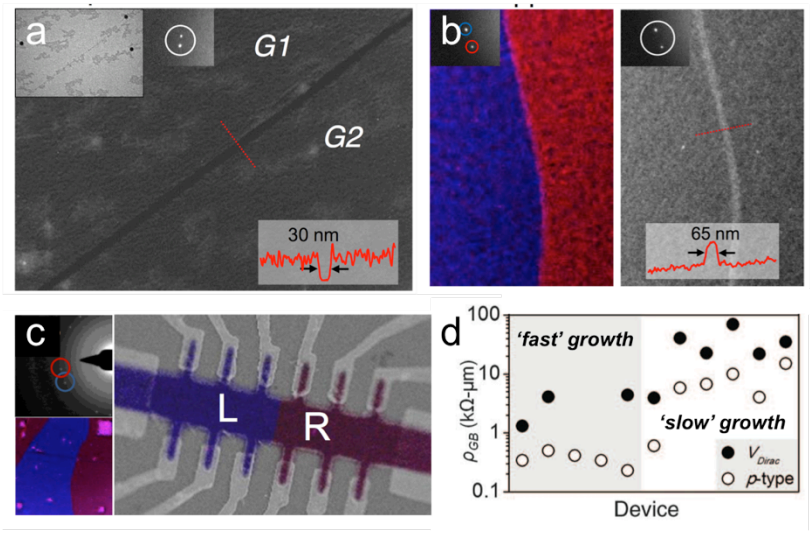


**Figure 3.5: Electrical Performance of grain boundaries in large grain graphene. a,** DF-TEM image of an amorphous grain boundary, inset: bright field and diffraction images, and **b,** DF-TEM images of overlapped grain boundary. **c,** combined DF-TEM and SEM images of an electrical device overlapping a grain boundary. **d,** resistivity data for 11 devices, showing an order of magnitude higher resistivity for grain boundaries in the 'slow' growth.

The ability to slow down the graphene growth enables researchers to look into the growth kinetics[27,35]. $H_2$, in particular plays an important dual role; first, it activates surface-bound carbon which is necessary for monolayer growth. Additionally, it also acts as an graphene etchant, controlling the size and morphology of the graphene crystals[27].

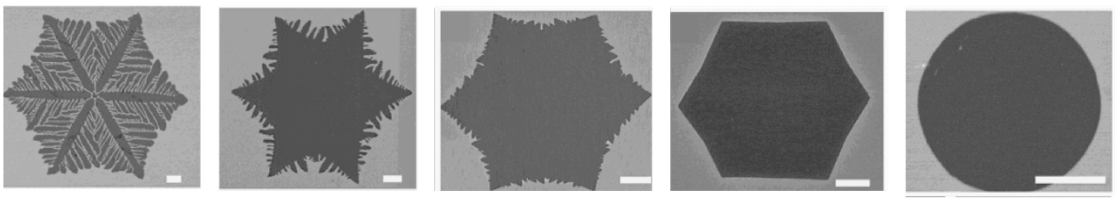

**Figure 3.6: Effect of Ar:$H_2$ ratio on the shape of graphene grains.** The images progress from left to right from negative (high Ar:$H_2$ ratio) to positive (Low Ar:$H_2$ ratio) curvature edges. All scale bars are 5 μm. Adapted from [35].

As shown in Figure 3.6, the ratio between Ar:$H_2$ during large-grain growth can be used to change the grain morphology. These findings help researchers better understand and control the growth processes.

## 3.4 Bilayer Graphene

In general, BLG shows some desirable properties for some applications. Bernal stacked BLG has been shown to have a small, tunable bandgap[36], a desirable property for active components in semiconducting devices. At the same time, twisted BLG possess angle-dependent optical and electronic properties, as described in Chapters 1 and 2, making it a candidate for optoelectric applications. However, the growth of large-scale BLG with uniform twist angle has not been demonstrated. Here we explore the mechanisms of BLG growth on Cu substrates. BLG areas can be grown by CVD process on Cu substrates despite the limited carbon solubility in Cu. Careful control of growth parameters could be used to enhance, or suppress, the growth of additional layers during graphene growth[37,38]. Using low energy electron microscopy (LEEM) imaging of graphene grown on Cu, it was shown that additional graphene layers stack like an inverted wedding cake, where the smaller layer is under the larger layer (see

Figure 3.7)[39]. The proposed mechanism is one which methane decomposes on the bare Cu, generating C adatoms that diffuse under the previous graphene sheet.

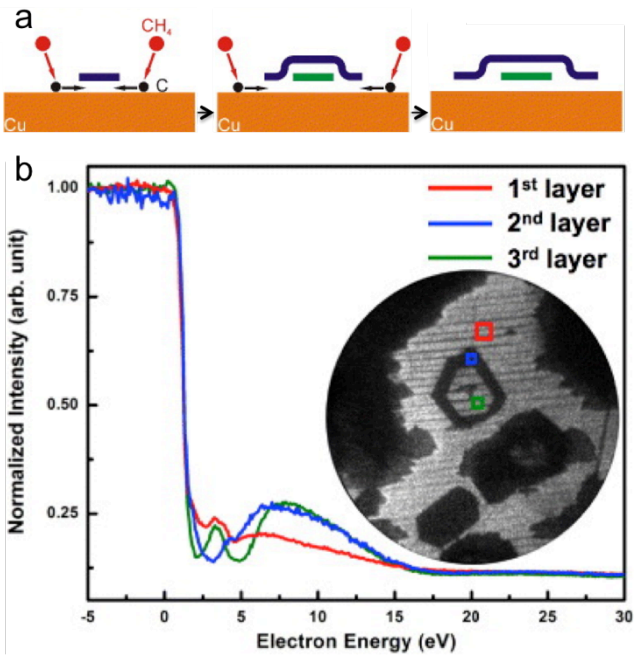


**Figure 3.7: Bilayer growth mechanism. a,** Cross-sectional schematics of the growth process of graphene layers on a Cu substrate, depicting the underlayer mechanism of nucleation and growth during CVD. The new graphene layer (green) nucleates below the single layer (blue), giving an inverted wedding cake structure. **b,** Electron reflectivity versus electron energy for one–three graphene layers on Cu foil. Measurement regions are color coded in the LEEM image (field of view is 15 μm). Layers one, two and three have no pronounced minimum, a single minimum at ~3 eV, or two minima, respectively. Adapted from [39]

Considering this model, BLG growth could be quenched by increasing the methane/$H_2$ ratio, thus preferentially encouraging the growth of the first layer, and not allowing time for carbon species to diffuse below the first layer[40]. Alternately, the same principle could be used to encourage bilayer growth, creating bilayer coverage of up to 67%, as shown in an example in Figure 3.8a[37]. Employing large-grain graphene recipes, large Bernal stacked graphene bilayer areas have been reported, up to 300 μm for a single grain[38].

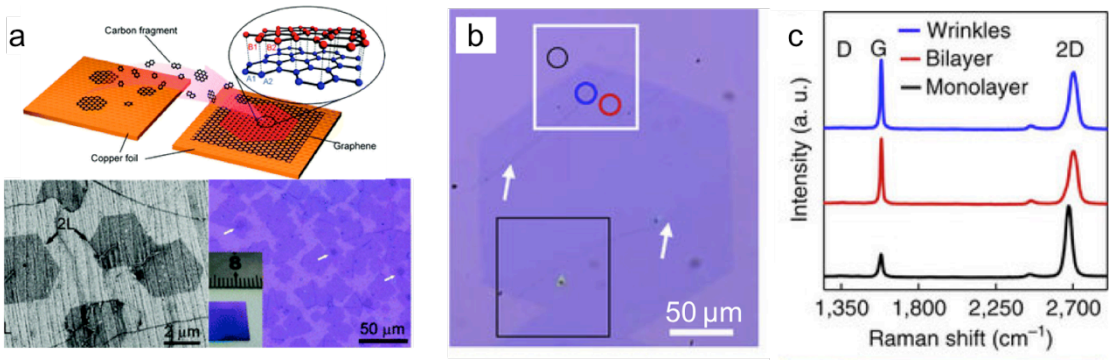


**Figure 3.8: Bilayer graphene CVD growth. a,** High density Bernal stacked bilayer growth, up to 67% coverage. Adapted from [37]. **b,** Large bilayer graphene grain, 300 μm across, and **c,** Raman data showing the Raman signature for monolayer (black) and bilayer (blue) graphene in (b). Adapted from [38].

Nonetheless, angle uniformity is difficult to obtain in CVD grown bilayer graphene. While Bernal stacked BLG can be obtained, as it is the energetically preferred form[41], the production of large areas with uniform, non-zero twist angle using CVD is unlikely, and CVD bilayers often spans multiple orientations even in connected BLG regions[42].

## 3.5 Transfer

In order to utilize graphene's exquisite properties it is often essential to transfer graphene from its growth substrate to various structures. A transfer method, ideally, would enable the removal of graphene from its growth substrate without damaging it, and subsequently deposit it on the desired surface. Additionally, the transfer method should be clean – it should leave the transferred graphene layers without contaminants –, easy, and would ideally render the growth substrate reusable for further growths. There are many available techniques for transferring graphene from Cu foils onto arbitrary target substrates[43–45]. Among these, the use of a poly(methyl methacrylate)

(PMMA) as a support layer, followed by liquid Cu etching, has become a prevalent transfer method. This method is relatively straightforward, and it allows for transfer onto both supported and suspended geometries. In this section we will explore this method and other, less frequently used, transfer methods[46].

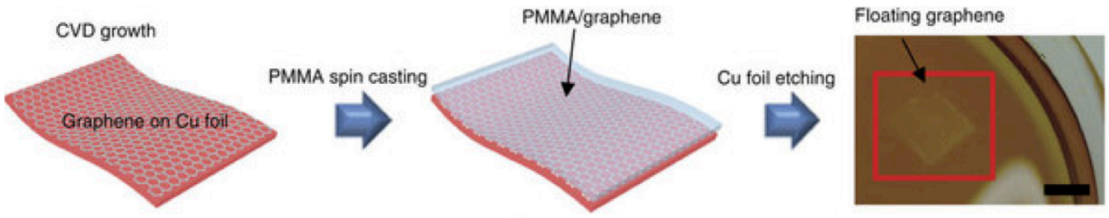


**Figure 3.9: PMMA transfer process.** Grapehene on Cu is coated with a PMMA film, followed by etching of the Cu substrate. Adapted from [49]

The PMMA method can be used to transfer graphene from its Cu growth substrate cleanly, quickly, and over large areas[47]. This method, depicted in Figure 3.9, includes the following steps: first, PMMA (MicroChem, 495K, 2% in Anisol, 4000 rpm, 60 sec) is spun on the graphene surface, creating a 150 nm thick PMMA layer. The PMMA/graphene/Cu stack is then floated on top of Cu etchant solution (Transene, CE-200), until the Cu has completely dissolved, about 4 hours. It is then transferred into several ultra high purity water baths, and transferred onto the desired substrate by inserting it into the water and "fishing" the PMMA/graphene film. The stack is then dried by gently blowing $N_2$ gas, and the PMMA is washed off in acetone and isopropanol (IPA) baths for 10 minutes each. This process, however, often results in trapped iron particle residue from the Cu etch solution under the graphene layer. This can be ameliorated by dipping the PMMA/graphene stack in a dilute acidic

solution for a few minutes to remove iron particles, or by using a saturated ammonium persulfate[48] as an etchant, for a cleaner result.

The transfer process for suspended samples is slightly different. There are several substrates that are well suited for the investigation of graphene's properties as a free-standing membrane, free of substrate interactions. These include a variety of TEM grids with holes in various sizes, sometimes with additional capacities for heating or electrical measurements (see Figure 3.10)[50,51]. For these applications, the PMMA can be slowly ashed in air for 3 hours at a mildly high temperature (300-350 °C).

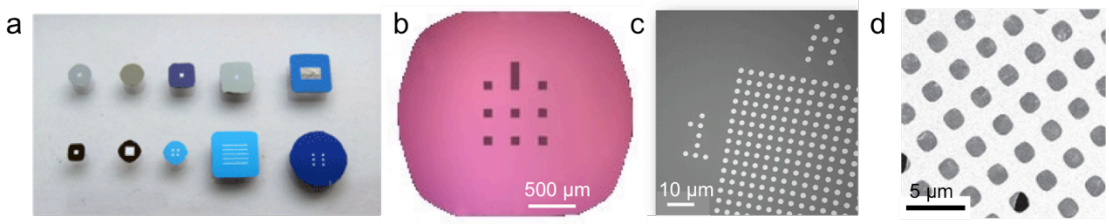


**Figure 3.10: A variety of options for TEM grids for concurrent examination of structural, electronic, mechanical and optical properties. a,** Selection of TEM grids. **b,** Optical image of a TEM chip with 10 nm SiN windows 100 µm wide. **c,** SEM image of a TEM chip with arrays of 2 µm holes. Images from TEMWindows.com. **d,** graphene suspended on holes. Adapted from [20].

Still, these methods leave the graphene with some carbon residue, which often renders high-resolution imaging methods – such as HR-TEM and STM – very difficult. Several 'direct transfer' methods have been proposed for graphene transfer without the PMMA support membrane. The first is simply laying a flexible gold (Au) TEM grid face-down on the graphene surface, and applying a drop of a liquid with high vapor pressure, such as IPA, to adhere the grid to the graphene[52]. The Cu is then

etched in a similar way to the PMMA method, and the grid is washed in water. This method is only compatible with flexible substrates, and its yield is low.

An additional economic transfer method, which preserves the growth substrate for subsequent growths, has been demonstrated for graphene on Pt, Cu, and Ni[53]. The metal foil is dipped into an aqueous sodium hydroxide (NaOH) solution and used as a cathode in an electrolysis cell. The water reduction reaction, which occurs at the cathode, then produces $H_2$ gas that serves to detach the graphene from the metal. This reaction is much faster than metal etching, and the metal can be re-used to grow high quality graphene films. Nonetheless, the somewhat aggressive bubbling process may interfere with the mechanical integrity of the PMMA/graphene film, and eliminating the bubbles post-detachment can be challenging, making this method non-ideal for large area transfer.

## 3.6 Conclusion

In this chapter we have reviewed two types of single-layer graphene CVD growths; First, a 'fast' growth, which results in a polycrystalline sheet with small, well stitched grains and excellent electrical properties for the entire sheet. Second, a 'slow' growth that results in large, often isolated graphene grains, with excellent electrical properties within the grain, but with higher resistance between grains, and compromised inter-grain stitching. We additionally examined methods for creating bilayer graphene films. We show that it is possible to create Bernal stacked bilayer films with coverage close to 70%, but, for reasons that will be discussed in the next chapter, that it would be difficult to create high coverage of uniform, non-zero tBLG via CVD growth.

Finally, we reviewed methods used to transfer graphene off of its growth substrate onto arbitrary surfaces.

REFERENCES


1. Yu, Q. *et al.* Graphene segregated on Ni surfaces and transferred to insulators. *Appl. Phys. Lett.* **93,** 113103 (2008).

2. Kim, K. S. *et al.* Large-scale pattern growth of graphene films for stretchable transparent electrodes. *Nature* **457,** 706–710 (2009).

3. Reina, A. *et al.* Large area, few-layer graphene films on arbitrary substrates by chemical vapor deposition. *Nano Lett.* **9,** 30–5 (2009).

4. Li, X. *et al.* Large-area synthesis of high-quality and uniform graphene films on copper foils. *Science* **324,** 1312–4 (2009).

5. Li, X., Cai, W., Colombo, L. & Ruoff, R. S. Evolution of graphene growth on Ni and Cu by carbon isotope labeling. *Nano Lett.* **9,** 4268–72 (2009).

6. Li, X. *et al.* Synthesis, Characterization, and Properties of Large-Area Graphene Films. in *ECS Transactions* **19,** 41–52 (ECS, 2009).

7. Fujita, T., Kobayashi, W. & Oshima, C. Novel structures of carbon layers on a Pt(111) surface. *Surf. Interface Anal.* **37,** 120–123 (2005).

8. Coraux, J., N'Diaye, A. T., Busse, C. & Michely, T. Structural coherency of graphene on Ir(111). *Nano Lett.* **8,** 565–70 (2008).

9. Cai, W., Zhu, Y., Li, X., Piner, R. D. & Ruoff, R. S. Large area few-layer graphene/graphite films as transparent thin conducting electrodes. *Appl. Phys. Lett.* **95,** 123115 (2009).

10. Sutter, P. W., Flege, J.-I. & Sutter, E. A. Epitaxial graphene on ruthenium. *Nat. Mater.* **7,** 406–11 (2008).

11. Sutter, P., Sadowski, J. T. & Sutter, E. Graphene on Pt(111): Growth and substrate interaction. *Phys. Rev. B* **80,** (2009).

12. Varykhalov, A. & Rader, O. Graphene grown on Co(0001) films and islands: Electronic structure and its precise magnetization dependence. *Phys. Rev. B* **80,** 035437 (2009).

13. Wang, S. M. *et al.* Synthesis of graphene on a polycrystalline Co film by radio-frequency plasma-enhanced chemical vapour deposition. *J. Phys. D. Appl. Phys.* **43,** 455402 (2010).

14. Kwon, S.-Y. *et al.* Growth of semiconducting graphene on palladium. *Nano Lett.* **9,** 3985–90 (2009).

15. Miniussi, E. *et al.* Thermal Stability of Corrugated Epitaxial Graphene Grown on Re(0001). *Phys. Rev. Lett.* **106,** 216101 (2011).

16. Kondo, D. *et al.* Low-Temperature Synthesis of Graphene and Fabrication of Top-Gated Field Effect Transistors without Using Transfer Processes. *Appl. Phys. Express* **3,** 025102 (2010).

17. Kumar, S. *et al.* Low Temperature Graphene Growth. in *ECS Transactions* **19,** 175–181 (ECS, 2009).

18. Yan, Z. *et al.* Growth of bilayer graphene on insulating substrates. *ACS Nano* **5,** 8187–92 (2011).

19. Sun, Z. *et al.* Growth of graphene from solid carbon sources. *Nature* **468,** 549–52 (2010).

20. Huang, P. Y. *et al.* Grains and grain boundaries in single-layer graphene atomic patchwork quilts. *Nature* **469,** 389–92 (2011).

21. Kim, K. *et al.* Grain boundary mapping in polycrystalline graphene. *ACS Nano* **5,** 2142–6 (2011).

22. Lau, C. N., Bao, W. & Velasco, J. Properties of suspended graphene membranes. *Mater. Today* **15,** 238–245 (2012).

23. Tsen, A. W. *et al.* Tailoring Electrical Transport Across Grain Boundaries in Polycrystalline Graphene. *Science* **336,** 1143–1146 (2012).

24. Ruiz-Vargas, C. S. *et al.* Softened elastic response and unzipping in chemical vapor deposition graphene membranes. *Nano Lett.* **11,** 2259–63 (2011).

25. Lee, G.-H. *et al.* High-Strength Chemical-Vapor-Deposited Graphene and Grain Boundaries. *Science* **340,** 1073–1076 (2013).

26. Mattevi, C., Kim, H. & Chhowalla, M. A review of chemical vapour deposition of graphene on copper. *J. Mater. Chem.* **21,** 3324 (2011).

27. Vlassiouk, I. *et al.* Role of hydrogen in chemical vapor deposition growth of large single-crystal graphene. *ACS Nano* **5,** 6069–76 (2011).

28. Vlassiouk, I. V *et al.* Graphene Nucleation Density on Copper: Fundamental Role of Background Pressure. *J. Phys. Chem. C* 130821140638002 (2013). doi:10.1021/jp4047648

29. Li, X. *et al.* Large-area graphene single crystals grown by low-pressure chemical vapor deposition of methane on copper. *J. Am. Chem. Soc.* **133,** 2816–9 (2011).

30. Nie, S., Wofford, J. M., Bartelt, N. C., Dubon, O. D. & McCarty, K. F. Origin of the mosaicity in graphene grown on Cu(111). *Phys. Rev. B* **84,** 155425 (2011).

31. Yan, Z. *et al.* Toward the synthesis of wafer-scale single-crystal graphene on copper foils. *ACS Nano* **6,** 9110–7 (2012).

32. Hao, Y. *et al.* The role of surface oxygen in the growth of large single-crystal graphene on copper. *Science* **342,** 720–3 (2013).

33. Wu, Y. A. *et al.* Large single crystals of graphene on melted copper using chemical vapor deposition. *ACS Nano* **6,** 5010–7 (2012).

34. Yu, Q. *et al.* Control and characterization of individual grains and grain boundaries in graphene grown by chemical vapour deposition. *Nat. Mater.* **10,** 443–9 (2011).

35. Wu, B. *et al.* Self-organized graphene crystal patterns. *NPG Asia Mater.* **5,** e36 (2013).

36. Zhang, Y. *et al.* Direct observation of a widely tunable bandgap in bilayer graphene. *Nature* **459,** 820–3 (2009).

37. Yan, K., Peng, H., Zhou, Y., Li, H. & Liu, Z. Formation of bilayer bernal graphene: layer-by-layer epitaxy via chemical vapor deposition. *Nano Lett.* **11,** 1106–10 (2011).

38. Zhou, H. *et al.* Chemical vapour deposition growth of large single crystals of monolayer and bilayer graphene. *Nat. Commun.* **4,** 2096 (2013).

39. Nie, S. *et al.* Growth from Below: Bilayer Graphene on Copper by Chemical Vapor Deposition. (2012). at <http://128.84.158.119/abs/1202.1031?context=cond-mat>

40. Fang, Wenjing, S. M. M. I. of T. Bilayer graphene growth by low pressure chemical vapor deposition on copper foil. (Massachusetts Institute of Technology, 2012). at <http://dspace.mit.edu/handle/1721.1/75656>

41. Suárez Morell, E., Vargas, P., Chico, L. & Brey, L. Charge redistribution and interlayer coupling in twisted bilayer graphene under electric fields. *Phys. Rev. B* **84,** (2011).

42. Brown, L. *et al.* Twinning and twisting of tri- and bilayer graphene. *Nano Lett.* **12,** 1609–15 (2012).

43. Suk, J. W. *et al.* Transfer of CVD-grown monolayer graphene onto arbitrary substrates. *ACS Nano* **5,** 6916–24 (2011).

44. Gao, L. *et al.* Repeated growth and bubbling transfer of graphene with millimetre-size single-crystal grains using platinum. *Nat. Commun.* **3,** 699 (2012).

45. Li, X. *et al.* Large-area synthesis of high-quality and uniform graphene films on copper foils. *Science* **324,** 1312–4 (2009).

46. Kang, J., Shin, D., Bae, S. & Hong, B. H. Graphene transfer: key for applications. *Nanoscale* **4,** 5527–37 (2012).

47. Li, X. *et al.* Transfer of large-area graphene films for high-performance transparent conductive electrodes. *Nano Lett.* **9,** 4359–63 (2009).

48. Pirkle, A. *et al.* The effect of chemical residues on the physical and electrical properties of chemical vapor deposited graphene transferred to SiO2. *Appl. Phys. Lett.* **99,** 122108 (2011).

49. Kim, Y. *et al.* Strengthening effect of single-atomic-layer graphene in metal-graphene nanolayered composites. *Nat. Commun.* **4,** 2114 (2013).

50. Barton, R. A. *et al.* High, size-dependent quality factor in an array of graphene mechanical resonators. *Nano Lett.* **11,** 1232–6 (2011).

51. Bunch, J. S. *et al.* Impermeable atomic membranes from graphene sheets. *Nano Lett.* **8,** 2458–62 (2008).

52. Regan, W. *et al.* A direct transfer of layer-area graphene. *Appl. Phys. Lett.* **96,** 113102 (2010).

53. Gao, L. *et al.* Repeated growth and bubbling transfer of graphene with millimetre-size single-crystal grains using platinum. *Nat. Commun.* **3,** 699 (2012).

# CHAPTER 4

# IMAGING THE ATOMIC REGISTRY IN BILAYER AND TRILAYER GRAPHENE

## 4.1 Introduction

Bilayer graphene (BLG) and trilayer graphene (TLG) are a prototypical layered material system where interlayer structure and coupling determine key physical properties. Their electronic, optical and mechanical properties may be varied depending upon their structures, including the stacking order, relative twist, and interlayer spacing[1–7], providing ways to realize useful characteristics not available to single layer graphene. Well known examples are Bernal stacked (BS) BLG and rhombohedral TLG, which open tunable band gaps in a transverse electric field[8–10], making them promising candidates for optoelectronic and nanoelectronic applications. Twisted BLG (tBLG) has also been a subject of many recent studies, both theoretical and experimental, where the interlayer coupling, which can be sensitive to the configuration of commensurate unit cell, provides intriguing possibilities for controlling electronic band structure[11]. Furthermore, graphene growth using chemical vapor deposition (CVD) can produce large areas of single and multilayer graphene, as discussed in Chapter 3[12–14], which could allow utilization of BLG and TLG in technologically relevant scale. However, CVD grown BLG and TLG may grow in various stacking configurations that are not common in natural graphite. This presents a significant problem, since most applications require materials with uniform electrical and optical properties. Controlling stacking and other structural properties in BLG and

TLG synthesis thus necessitates efficient large-scale characterization of multilayer graphene structures, which must provide all key structural information. These include the twist angle, stacking configuration, interlayer spacing as well as local structural deformations.

This chapter is largely adapted from L. Brown *et al*, "Twinning and Twisting of Tri- and Bilayer Graphene", ***Nano Letters***, 12, 1609-1615 (2012), and describes work done mainly in collaboration with R. Hovden on the structural characterization of graphene layers. We use dark-field transmission electron microscopy (DF-TEM) and selected area electron diffraction (SAED) techniques for quick, accurate, and high-resolution determination of twist angle, interlayer atomic registry (stacking order) and interlayer spacing of bi- and tri-layer CVD graphene. In contrast to micro-Raman mapping[15] and high-resolution TEM[16] these techniques allow large areas to be mapped and processed in minutes. The accessibility of these techniques, which utilize a common, commercial uncorrected TEM, is particularly appealing. In DF-TEM, real-space images are formed from a selected diffracted beam. These images are sensitive to the alignment between the electron diffraction angle and the crystal orientation and have been used to characterize the grain structure of CVD graphene (see Chapter 2)[17,18]. SAED provides regional structural information and has enabled quantification of the intrinsic surface roughening in exfoliated graphene[19]. We use the SAED peak intensities measured at various diffraction and sample tilt angles which, when combined with DF-TEM imaging, provide a powerful set of information that enables detailed structural characterization in BLG and TLG.

Using this technique, we first find that our CVD growth produces a mixture of BLG and TLG areas both in oriented (non-twisted) and twisted configurations, with the oriented ones as the major species. Our data show that the structure of oriented BLG (oBLG) and TLG (oTLG) contain long-range atomic registry and conform exclusively to either Bernal or rhombohedral stacking with the same interlayer spacing as that of natural graphite (3.35 Å). In contrast, we show that twisted BLG (tBLG) lacks long range atomic registry, and that the twisted layers are free to move laterally with respect to each other, suggesting superlubricity[20] between the top and bottom layers. The atomic registry (and its absence) in oBLG and tBLG is consistent with the two different strain induced deformations we observed. In oBLG, multiple domains of two different Bernal stacked configurations (AB vs. AC stacking) coexist within individual oBLG pieces connected by discrete twin domain boundaries, while individual layers in tBLG regions continuously stretch and shear independently forming elaborate Moiré patterns. Finally, these results will be discussed together with an angle-dependent interlayer potential model, which explains the twist angle distribution in our CVD few-layer graphene.

## 4.2 Imaging Graphene Layers with Dark Field Transmission Electron Microscopy

The graphene samples studied in this chapter were synthesized using the low-pressure CVD method[12,13], which produces large grain, high quality graphene. Previously, it was shown that this method can be used to grow graphene with a different number of layers and various grain structures by modifying growth parameters, such as reactant

gas flow rates and furnace temperature (see Chapter 3 for more details)[21–24] – making it an ideal method for producing large scale BLG and TLG samples. Under our growth conditions (we use a recipe similar to that in ref. [12]) we observe extended single layer graphene (10 – 60 μm across) dotted with multilayer regions, whose size ranges between 2 and 7 microns across (see angle and size distribution in Figure 4.1e). While SEM images may be used to locate these multilayer regions and to resolve the number of layers in each region (Figure 4.1a), they provide no other structural information. In order to measure the twist angles in these regions, we transferred the graphene from the Cu growth substrate to a TEM support grid, and took a SAED image of each region. Multilayer regions are either all in same orientation indicated by the single set of six-fold diffraction peaks (Figure 4.1b, inset), or arranged in twisted configurations with more than one set of diffraction peaks (Figure 4.1c, inset), or in a combination of these two options (Figure 4.1d).

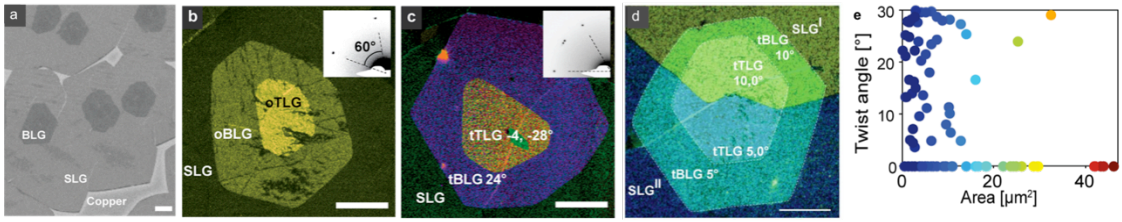


**Figure 4.1: Imaging twist angles in multilayer graphene. a,** SEM image of CVD graphene partially grown on the Cu substrate. **b-d,** DF-TEM image of **b,** oriented BLG and TLG. *Inset*: diffraction pattern with one set of peaks within 60°. **c,** three layers that are twisted with respect to each other. *Inset*: diffraction pattern within 60°. **d,** second and third layers (dotted borders), in an area where two SLGs meet ($SLG^{I}$ and $SLG^{II}$). Relative twist angles are labeled in each region. All scale bars are 1 micron. **e,** twist angle vs. area plot measured for over 100 BLG domains.

Once these diffraction spots are identified, DF-TEM images are taken to form spatial images of BLG and TLG regions with an aperture chosen for each electron diffraction spots. The combination of SAED and DF-TEM images thus allow full determination of twist angles in each multilayer graphene area (Figure 4.1b-d). In Figure 4.1e, we show the distribution of twist angle and area measured from over a hundred individual bilayer domains in 50 contiguous multilayer sites. We find that in our CVD growth most of the bilayer area is oriented (70%), while only 30% are twisted. An additional histogram is shown in Figure 4.11.

## 4.3 Stacking Order in Oriented Bilayer and Trilayer Graphene

In both oriented and twisted multilayer graphene, one important question is the presence of interlayer atomic registry (stacking order). If adjacent layers are atomically registered, the x-y position of the two-atom unit cell is specified by a single lateral displacement vector everywhere. For instance, there are several different stacking configurations in oriented multilayer graphene. In the typical "graphitic", or "Bernal" stacking commonly found in highly oriented pyrolitic graphite (HOPG)[15], half of the atoms in one layer are positioned exactly on top of half the atoms of the other layer. Two different Bernal stacking arrangements exist for bilayer graphene—for a given basis layer A, the second layer can be either a B or a C layer, each shifted by half a basis vector (arrows, Figure 4.2a) with respect to each other. Furthermore, for oriented TLG, there are two principle forms—a Bernal (ABA) stacked, or rhombohedral (ABC) stacked trilayer. While geometrically similar, these two stacking arrangements can radically change the electronic properties—from tunable bandgaps

in BS-BLG and rhomboheral TLG to metallic behaviors in Bernal stacked TLG[8,23]. Other types of stacking are also possible in oriented multilayer graphene, such as AA stacking[25]. Currently there are no direct studies on the stacking order in CVD multilayer graphene. We use the relative electron diffraction intensity in our DF-TEM images for this purpose. Our results on oriented BLG and TLG are shown in Figure 4.3 and Figure 4.4.

### 4.3.1 Diffraction in Oriented Graphene Layers

In oBLG, the electron diffraction intensities could be larger or smaller than that of a single layer graphene[19]. This is because the electron wave diffracted from one layer interferes with the wave diffracted from the other layer, where the relative phase φ between the two diffracted waves is determined by the lateral shift (Δx) of the lattice lines in the top layer relative to those in the bottom layer. Under the flat Ewald sphere approximation, this leads to fully constructive (or destructive) interference when Δx = 0 (Δx = ½ lattice period).

Using this model, the DF-TEM intensity for the first and second order families of diffraction peaks $Ø_1$ and $Ø_2$ (see Figure 4.2b) can be estimated for Bernal stacked oBLG. For $Ø_2$ peaks, which corresponds to the lattice line periodicity of $a_2$= 1.23 Å (red lines in Figure 4.2a, c), fully constructive interference occurs since lattice lines in both top and bottom layers are vertically aligned (Figure 4.2c). Maximum intensities are expected for all oriented BLG and TLG with graphitic stacking configurations for the same reason, when they are imaged using one of the $Ø_2$ peaks. In contrast, the lattice lines with a longer $a_1$= 2.13 Å period (corresponding to $Ø_1$ peaks in Figure

4.2b) are shifted in the top layer by one third of the period (Figure 4.2d), resulting in a phase shift of $\varphi = (2\pi)(\Delta x/a_1) = 2\pi/3$. This phase is also highly sensitive to tilts; for the configuration shown in Figure 4.2d, $\varphi$ will decrease (increase) with a small clockwise (counter-clockwise) tilt rotation.

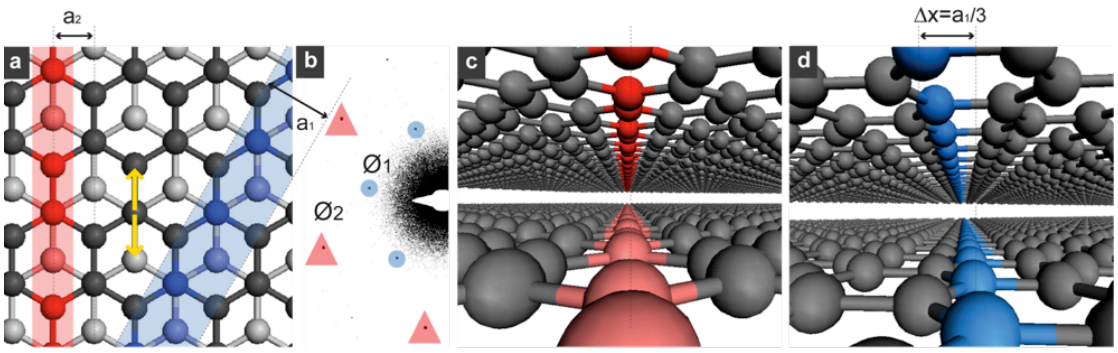


**Figure 4.2: Diffraction in oriented BLG and TLG. a,** Bernal stacked (BS) bilayer. The graphene lattice with period $a_2$= 1.23 Å ($a_1$= 2.13 Å) is highlighted in red (blue). Displacement vectors for AB, or AC, configurations are marked in yellow. **b,** SAED pattern of BS-BLG. We name the equivalent Bragg reflections $Ø_2$ and $Ø_1$, corresponding to 1.23 Å and 2.13 Å lattice spacing. **c,** 3D illustration of BS-BLG 1.23 Å lattice; **d,** 3-D illustration of BS-BLG 2.13 Å lattice.

### 4.3.2 Stacking Faults in Oriented Layers

We observe these behaviors from the DF-TEM images of our oriented BLG and TLG. In Figure 4.3a we show a DF-TEM image of an oBLG domain connected to a tBLG (twisted angle = 7°), taken with a $Ø_2$ peak. The oBLG area is almost four times as bright as the single layer as a result of fully constructive interference, whereas the rotated bilayer is simply twice as bright. We observe this brighter DF-TEM intensity from any of the six $Ø_2$ peaks for all oBLG areas in our sample, with a uniform intensity. This confirms that CVD grown oBLG has a long range stacking

order and atomic interlayer registry. We also note that this increase in intensity is an efficient way to identify oriented multilayer regions. Furthermore, our measurements show that $Ø_1$ intensities on oBLG (Figure 4.4) and TLG (Figure 4.3b) are consistent with the expected values for graphitic stacking (Bernal or rhombohedral) order, thus excluding the AA stacking. One representative example is shown in Figure 4.3b-e. These are DF-TEM images of an oriented BLG/TLG region, with Figure 4.3d (taken with a $Ø_2$ peak) and Figure 4.3e ($Ø_1$) each showing a zoom-in image of the TLG area marked in Figure 4.3b (also taken with a $Ø_2$ peak).

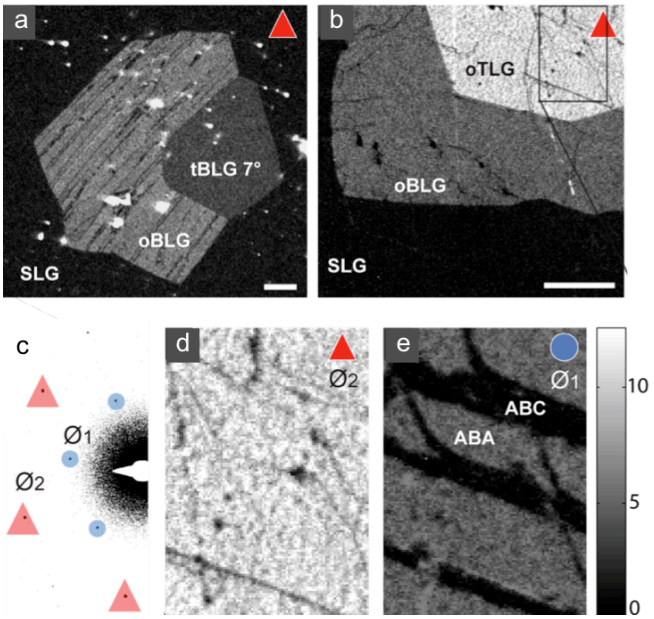


**Figure 4.3: Stacking order in oriented BLG and TLG. a,** DF-TEM ($Ø_2$) image of BLG containing two stacking arrangements - a Bernal stacked region and a twisted region (7° rotation). The intensity of the BS region is roughly twice that of the twisted region. **b,** DF-TEM ($Ø_2$) of trilayer graphene with graphitic (ABA, ABC, or ACB) stacking; the uniform intensity indicates complete coverage. **c,** SAED pattern of BS-BLG. **d,** close-up of the trilayer area in (b). **e,** DF-TEM ($Ø_1$) of the same region shows discrete changes in regional intensity, indicating ABA (bright) and ABC / ACB (dark) stacking. DF-TEM image intensities are normalized to the first layer. All scale bars are 1 micron.

While Figure 4.3d shows uniformly bright intensity as expected, Figure 4.3e has sharply defined bright and dark stripes. Because the dark striped regions in Figure 4.3e maintain the same bright intensity in Figure 4.3d (roughly 9 times as bright as single layer graphene), they cannot be tears or gaps in the graphene. Instead, the discrete changes in Figure 4.3e and the uniform intensities in Figure 4.3d of the oTLG area agree with the expected theoretical intensities for two different graphitic stackings, Bernal (ABA; bright stripes in Figure 4.3e) and rhombohedral (ABC; dark stripes). In particular, the ABC stacked areas show completely destructive interference because the diffracted electron wave from the second and third layer has a relative phase difference of $2\pi/3$ and $4\pi/3$, respectively.

### 4.3.3 Observation of Twinning in Oriented Bilayer Graphene

Surprisingly, we observe similar behaviors from Bernal stacked BLG, as shown in Figure 4.4a and b. The $Ø_2$ image of a Bernal stacked BLG (Figure 4.4a) shows uniform intensity, incorrectly suggesting a continuously stacked second layer, whereas the $Ø_1$ image of the same area (Figure 4.4b) display sharply contrasted bright and dark stripes. These structures with discrete changes in the $Ø_1$ intensity are abundant across all of our oBLG samples—they are often observed along parallel lines (Figure 4.4b, c), or in complex orientations (Figure 4.4d), while few BS regions do not display them at all (Figure 4.4e). We ascribe these behaviors to the presence of two distinct Bernal stacked configurations (AB and AC) coexisting within single oBLG domains.

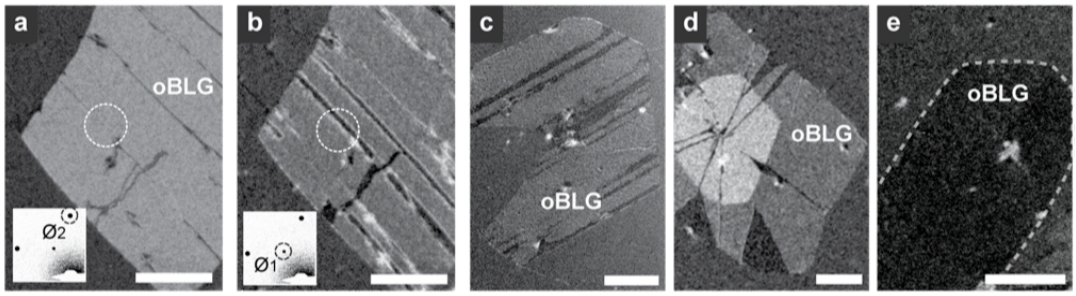


**Figure 4.4: Observation of twinning in oriented BLG. a,** DF-TEM ($Ø_2$) image of BS-BLG, with uniform intensity. *Inset*: diffraction pattern. **b,** DF-TEM ($Ø_1$) image of the same area in (a), shows sharp contrast from AB/AC twinning across the bilayer region. *Inset*: diffraction pattern. **c-e,** other examples ($Ø_1$) of twinning in BS bilayer graphene. oBLG border is marked in a dotted line in (e) for clarity. All scale bars are 1 micron.

As described earlier, they dark/bright domains are associated with two different displacement vectors (Figure 4.2a) and are mirrored configurations. When the BLG sample is perpendicular to the incoming electron beam, the two configurations are identical and cannot be distinguished. However, a slight tilting of the sample may break the mirror symmetry resulting in different $Ø_1$ peak intensities. To resolve the difference between the AB and AC mirrored configurations in BLG, one may thus exploit the sensitivity of the $Ø_1$ peak to sample tilt angle relative to the electron beam. Most of our oBLG samples are indeed not perfectly perpendicular to the electron beam axis, which explains the significant contrast observed in Figure 4.4b-d.

We confirm that these are Bernal stacked AB/AC crystalline twins by performing a tilt-dependent SAED analysis on two of these areas, as shown in Figure 4.5b. We plots the total intensity of diffraction spots 1, 2 and 3 (Figure 4.5a, *inset*), as a function of tilt angle for the twinned locations L and R shown in Figure 4.5a and c. One can see that the two $Ø_1$ peaks (1-diamond and 2-circle) express the mirrored

behavior of the twinned regions, while the $Ø_2$ peak (3-triangle) remains similar in both AB and AC stacking. This result is in agreement with previous discussion and our full theoretical calculation of the diffraction spot tilt pattern, determined from the scattered wave function of Bernal stacked graphene (see Figure 4.6).

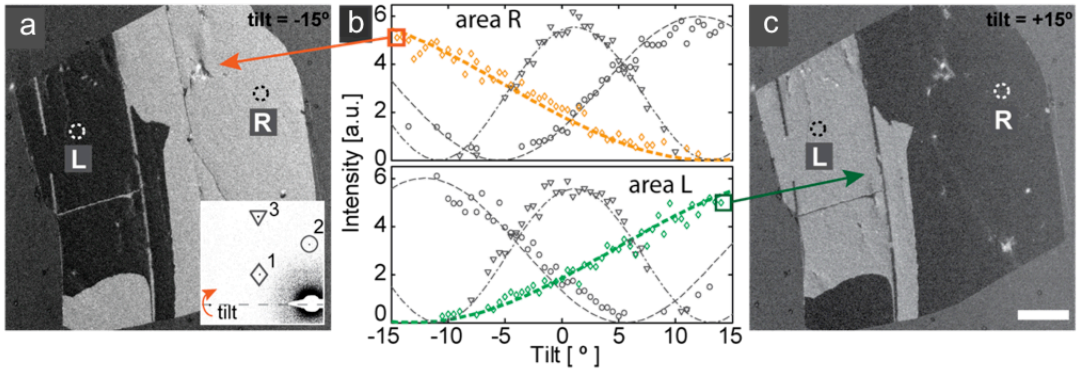


**Figure 4.5: SAED tilt series of oriented BLG twins. a,** DF-TEM image showing AB/AC twinning of a BS-BLG tilted -15° relative to the incident beam. Image was taken with diffraction peak #1, indicated in the inset. *Inset*: diffraction pattern taken at 0° tilt, showing the $Ø_1$ peaks 1 (diamond) and 2 (circle), and $Ø_2$ peak 3 (triangle). **b,** Integrated intensity of diffraction spots 1-3 as a function of tilt angle taken from regions R and L as marked in (a,c). Integrated intensity was determined from a 6-parameter 2D Gaussian fit. The dashed lines are theoretical intensities calculated for BS-BLG and an 80 keV electron beam. The curves corresponding to spot #1 location are marked in orange (area R) and green (area L) to highlight the mirrored symmetry in the twinned regions. **c,** DF-TEM image of the same area as (a) taken with diffraction spot #1 at +15° tilt. Scale bars are 1 micron.

The corresponding DF image intensity for each twinning regions of the BLG indeed varies with tilt angles, as demonstrated in Figure 4.5a and c, measured with tilt angles ±15°. These images clearly show twinning of oBLG. Furthermore, we can estimate the interlayer spacing in the Bernal stacked BLG by comparing our experimental SAED tilt data in Figure 4.5b and theoretical plots in Figure 4.6. Our analysis based on the plot using diffraction spot 2 in Figure 4.5b results in 3.27±0.18 Å, close to the 3.35 Å interlayer spacing for HOPG[26].

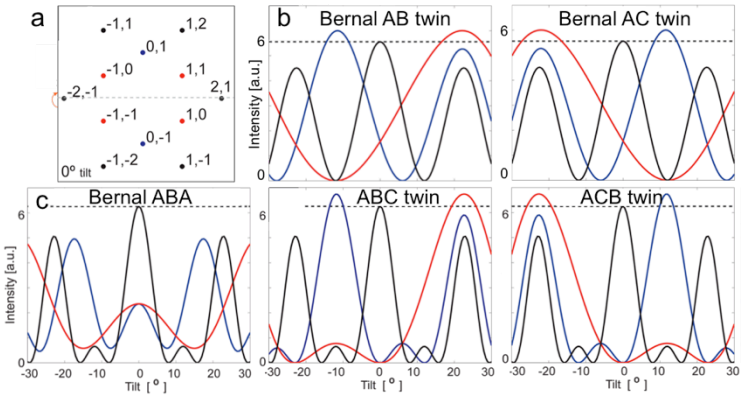


**Figure 4.6: Diffraction patterns tilt series for oriented BLG and TLG. a,** Color-coded diffraction peak pattern and tilt axis . **b-c,** Diffraction tilt patterns assuming a flat Ewald sphere of **b,** Twin forms of Bernal stacked BLG, and **c,** Bernal (left) and two rhombohedral stacked twin TLG,.

Our data shown in Figures 4.3-4.5 clearly demonstrate, for the first time in CVD graphene, that non-twisted TLG and BLG areas may contain crystalline twin boundaries. Since these twinning sites are not apparent from SAED without sample tilt, they may be easily mistaken for a single Bernal-stacked domain. In oTLG, we show that a single continuous trilayer region can be composed of both Bernal stacked (ABA) and rhombohedral (ABC) stacked regions—or their permutations—connected by a twin boundary. Similarly, in oBLG, mirrored twins of AB and AC stacked regions are also joined by twin boundaries. We note that this technique provides relative stacking information and does not determine in which layer the twinning occurs. However, it may be possible to infer twinned layers in multilayer systems through continuity with neighboring regions.

Tilted DF-TEM imaging of many samples revealed widely prevalent twinning in our CVD graphene. We propose that the twins observed here are gliding twins, where non-twinned graphene layers slide into a twin position under structural strain present

during growth and subsequent cooling[27]. Such strain could be induced by the graphene interaction with features in the Cu substrate, such as steps[28], or twin boundaries in Cu[29]. Our AFM measurements show that the twin boundaries correspond to a heightened surface line (Figure 4.7). This height deformation may also account for their appearance as dark lines in an $Ø_2$ DF-TEM image (see Figure 4.3a).

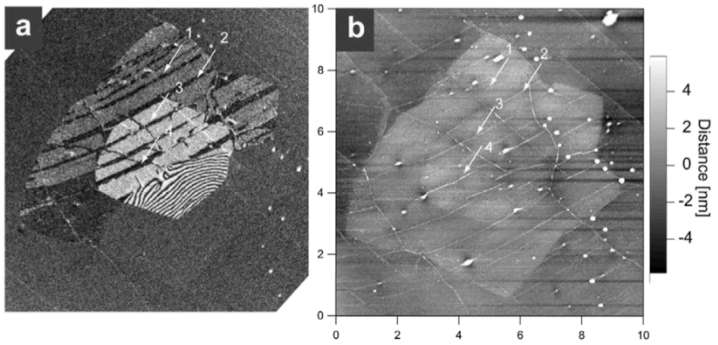


**Figure 4.7: Twin boundaries in AFM. a,** DF-TEM of the same area in Figure 4.3b, taken with an aperture around $Ø_1$. **b,** AFM height image of the same area. White arrows point to thin folds which correspond to twinning sites in the DF-TEM image.

Since previous work has demonstrated that twin boundaries on single-layer graphene exhibit structural corrugation and local changes in the densities of states[29], we expect that the presence of twins in bilayer graphene will also influence the electrical and mechanical properties of Bernal stacked graphene. Controlling these twinning sites will be crucial for device applications. This method had been applied by our group and collaborators to investigating the width, motion, and topological structure of the soliton boundaries in between AB/AC Bernal stacked bilayer graphene areas, shown in Figure 4.8 [30]. Other groups explore the unique electronic properties of soliton structures in BS-BLG which exhibit one-dimensional valley polarized

behavior, opening up opportunities for valley physics in graphene[31]. We also expanded this method to image the atomic registry and twin boundaries in *h*-BN bilayer stacks[32].

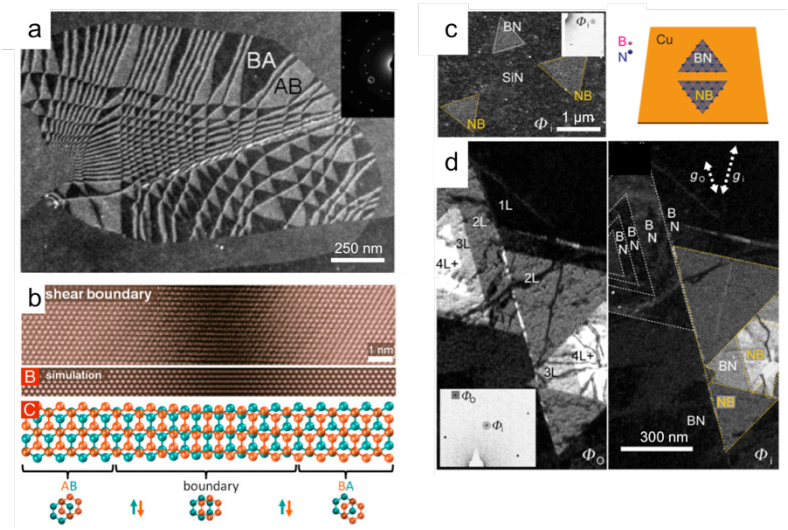


**Figure 4.8: Soliton grain boundaries in graphene and in *h*-BN. a,** DF-TEM images of bilayer graphene with AB/AC twin boundaries, which is obtained by selecting an inner diffraction spot, $Ø_1$ (inset). **b,** an atomic resolution STEM image of a soliton boundary. Adapted from [30]. **c,** DF-TEM image of single layer *h*-BN crystals (outlined by triangles), which is obtained by selecting an inner diffraction spot, $Ø_1$ (left). They show two different orientations, BN and NB, illustrated on the right. **d,** DF-TEM image of multilayer *h*-BN obtained by selecting an outer diffraction spot, $Ø_2$, (left) and an inner diffraction spot, $Ø_1$ (right), showing intensity changes for different stacking features. Adapted from [32].

## 4.4 Interlayer Coupling in Twisted Graphene Layers

Now we turn our discussion to the structure of twisted multilayer graphene grown using the CVD method. As discussed earlier, the electronic and mechanical properties of tBLG are expected to depend on the interlayer coupling, which in turn is predicted to depend strongly on the commensurability of each twist angle[4]. Since the size of the commensurate unit cell, an important parameter determining the interlayer coupling, fluctuates wildly for a small angle change, the band structure of tBLG for a given

angle remains difficult to predict. One important assumption for most existing theories for high-angle tBLG is that the configuration may be described by a set of discrete parameters (such as p, q indices used by Mele[4]), while treating the lattice constant of both layers as a fixed value. The TEM data shown in Figure 4.10, however, suggest that such assumption might not be valid in CVD graphene. Instead, our measurements provide strong evidence for superlubricity in twisted multilayer graphene systems. Superlubricity in graphene layers has been demonstrated previously, where force measurements on a rotating graphene flake on a graphite surface display sharp friction peaks at two angles, 0° and 60°, and close-to-zero values between them, shown in Figure 4.9.

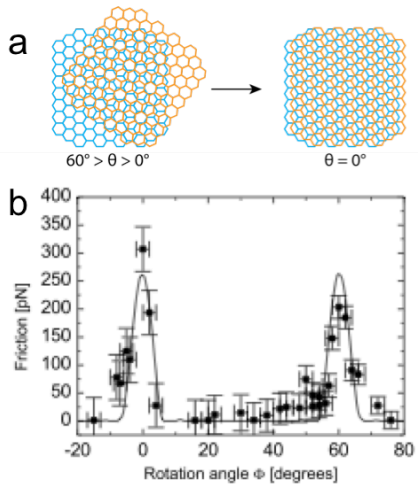


**Figure 4.9: Superlubricity in graphene layers. a,** Illustration of twisted graphene and the energetically preferred Bernal stacked graphene. **b,** Plot of friction versus rotation angle of a graphene flake on a graphite surface, displaying two sharp friction peaks at 0° and 60°.Adapted from [20].

This experiment, combined with the knowledge on the 6-fold symmetry in the graphene lattice, concludes that there is ultra-low friction between graphene layers at

high twist angles. These data have been reproduced for larger area graphene[33], and for other Van der Waals systems such as $MoS_2$[34], and is theoretically predicted for stacked heterostructures such as graphene/h-BN[35] and $MoS_2$/Fluorographene[36] systems.

### 4.4.1 Superlubricity in Twisted Graphene Layers

In Figure 4.10, we show DF-TEM images of commonly found trilayers AtA stacking system, where "t" denotes a twisted layer. In Figure 4.10a (left), we show SAED pattern taken from trilayer regions I and II (DF-TEM image, right) together; the SAED pattern shows the major diffraction peaks (including three peaks marked 1, 2, and 3) for the oriented graphene layers (colored pink in the DF-TEM image) and a set of weak spots corresponding to the rotated second layer (blue). When imaged using the major diffraction peak, the DF-TEM images of region I show the behaviors discussed previously, consistent with the atomic registry and uniform intensity within each domain. However, under the same imaging conditions, the intensity in region II presents a complex and continuously varying sinusoidal pattern, as shown in Figure 4.10b. We conclude that this is a trilayer system, with an AtA trilayer (region II), where the middle layer is rotated by 5°, adjoining an oriented TLG (region I). The relative sizes of the three layers are indicative of the slower rates growth rates for the second and the third layer, and support the proposed AtA structure for region II.

In general, two twisted layers are predicted to present a Moiré pattern[37–39], an interference pattern between two mismatched grids. However, twist bilayers with a few degrees of rotation angle show a Moiré periodicity of a few nanometers, too small to easily resolve in DF-TEM imaging. As a result, the tBLG in Figure 4.3a appears

uniform in the DF image despite its relatively small twist angle. When two layers have very similar orientations, such as the outer two layers in region II in Figure 4.10a, the Moiré periodicity becomes large and will eventually diverge for oriented bilayers if they have long range atomic registry. Instead, the AtA region in Figure 4.10a shows the complex Moiré pattern even though the outer two layers have the same orientation.

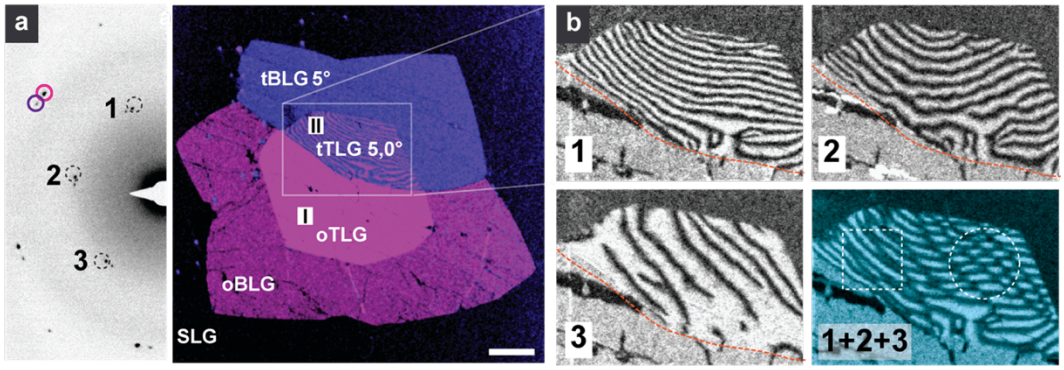


**Figure 4.10: Superlubricity in twisted BLG. a,** DF-TEM color-overlay image of a three layer system taken from two $Ø_2$ diffraction peaks (pink, blue) shown left. Region I shows a three layer graphitic stacking, and region II shows two oriented layers (top and bottom), separated by a twisted middle layer (blue, twist angle is 5°).The Moiré pattern in region II indicates continuous lateral displacement between the top and bottom layers. Scale bar is 1 micron. **b,** DF-TEM of the area marked in (a), taken from diffraction peaks 1, 2 and 3, excluding the peak diffracted by the rotated middle layer. The Moiré pattern is indicative of strain. The dashed line in images 1, 2 and 3 shows the boundary between region II and the graphitic region I. The bottom right image is a superposition of the other three images, where an area with isotropic (anisotropic) strain is marked by a circle (square).

This suggests that there are small lattice mismatches between the top and bottom layers, whose mismatch parameters are continuously varying (as opposed to discrete changes in Figure 4.3-Figure 4.5). This strongly suggests that these aligned "A" layers lack atomic registry or definite stacking order. We propose that this is a result of the lack of atomic registry between the twisted A-t bilayers, due to these

constituting layers (both A-t and t-A) being free to move laterally relative to each other, as a result of very low friction, or superlubrication. The Moiré periodicities we observe in Figure 4.10b are of the order of a few hundred nanometers, indicating strain between A-A layers is on the order of 0.1%. This indication of a spatially varying lattice mismatch in one of the "A" layers results in incommensurate structures for the A-t twisted bilayers. This observation could help explain some of the discrepancies between modeling and experiments in tBLG.

Under this model, the Moiré fringes in Figure 4.10a may also provide information on local strains, which differ between the two separated "A-A" layers. We further analyze the strain by imaging region II with different Ø1 peaks, as shown in Figure 4.10b. In each image we see different Moiré patterns, which indicate strain along the direction of the diffraction peak, as well as shear. The strain is highest perpendicular to the boundary between region I and region II (~0.2%) and much lower parallel to it (~0.01%), as seen in Figure 4.10b-1. Because pure strain would result in Moiré fringes only along the direction of each diffraction peak, the curvature of the lines in Figure 4.10b-2 indicates that both pure-strain and shear-strain elements are present. Furthermore, by superimposing all three interference images together (Figure 4.10b, bottom right), we can map out the degree of anisotropy in the strain field. As expected, it is highly anisotropic near the boundary between regions I and II, and become more isotropic away from it. The capability of imaging strain distribution in multilayer graphene, as demonstrated here will be an important characterization method for understanding the mechanical and electrical properties of CVD multilayer graphene devices.

## 4.5 Twist Angle Distribution in CVD Graphene Bilayers

The presence of atomic registry in oBLG and superlubricity in tBLG provides an important clue for explaining the observed twist angle distribution in our CVD multilayers.

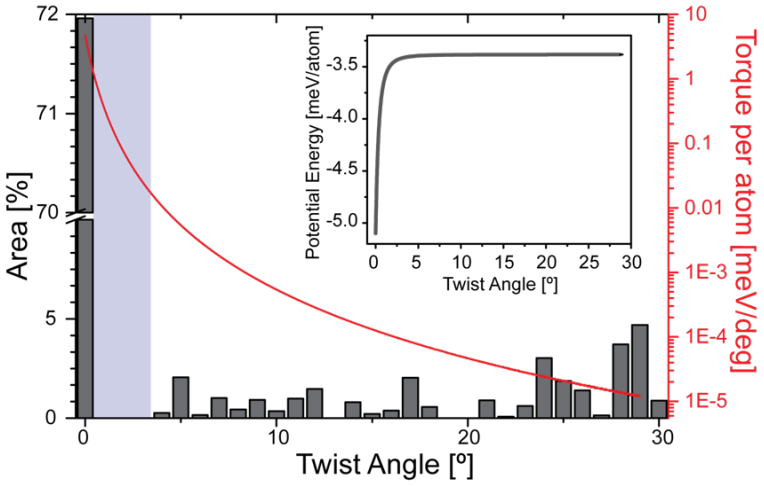


**Figure 4.11: Statistical analysis of twist angle distribution in bilayer graphene.** Area probability histogram of bilayer twist angles, taken from 50 continuous bilayer regions with >100 individual bilayers. Overlaid in red is the torque calculated based on the theoretical plot of the interlayer potential as a function of the twist angle (inset; as adapted from Morell *et al.*[6]).

In Figure 4.11, we plot area probability histogram compiled based on all our TEM measurements acquired using multiple CVD graphene samples. As discussed earlier, more than 70% of the BLG areas are oBLG with the rest being tBLG. Two additional trends are seen: we observe no tBLG areas with a twist angle smaller than 4° (shaded area in Figure 4.11), and find that the majority (81% of tBLG) of tBLG areas are directly connected to at least one oBLG region. It is well known that the Bernal stacked oBLG is the most energetically preferred BLG structure[6]. A theoretical

plot of calculated interlayer potential as a function of the twist angle is shown in the inset of Figure 4.11 (adapted from Morell *et al*.[6]). It suggests that during growth, tBLG will be subjected to torque, which would drive it toward smaller twist angles. The magnitude of the torque is proportional to the derivative of the interlayer potential and thus increases rapidly near the zero-angle. The depletion of tBLG for small twist angles is consistent with this picture. In addition, the lack of atomic registry in tBLG suggests a lower potential barrier, if any, against rotations driven by this torque, making tBLG unstable when it is not connected to oBLG regions.

## 4.6 Conclusion

In conclusion, we have used SAED and DF-TEM to resolve key structural parameters, including twist angle, stacking configurations, and interlayer spacing, in oriented and twisted BLG and TLG grown by CVD method. We find that different stacking configurations with long-range atomic registry coexist in oriented BLG and TLG forming twin boundaries. Similar twinning boundaries are abundant in other macroscopic and nanoscale materials and their properties and topological structures will be exciting to study in the future. In contrast, the lack of atomic registry in twisted graphene as discussed here, suggests new theoretical approaches would be desirable in the description of tBLG. Our model based on the interlayer potential and superlubricity in tBLG will be helpful in providing guidelines for controlling the coverage distribution of BLG and TLG with known twist angle by modifying the thermodynamic driving force and kinetics during the growth.

REFERENCES


1. Luican, A. *et al.* Single-Layer Behavior and Its Breakdown in Twisted Graphene Layers. *Phys. Rev. Lett.* **106,** (2011).

2. Lopes dos Santos, J. M. B., Peres, N. M. R. & Castro Neto, A. H. Graphene Bilayer with a Twist: Electronic Structure. *Phys. Rev. Lett.* **99,** (2007).

3. Shallcross, S., Sharma, S., Landgraf, W. & Pankratov, O. Electronic structure of graphene twist stacks. *Phys. Rev. B* **83,** (2011).

4. Mele, E. J. Commensuration and interlayer coherence in twisted bilayer graphene. *Phys. Rev. B* **81,** (2010).

5. Ohta, T., Bostwick, A., Seyller, T., Horn, K. & Rotenberg, E. Controlling the electronic structure of bilayer graphene. *Science* **313,** 951–4 (2006).

6. Suárez Morell, E., Vargas, P., Chico, L. & Brey, L. Charge redistribution and interlayer coupling in twisted bilayer graphene under electric fields. *Phys. Rev. B* **84,** (2011).

7. Hicks, J. *et al.* Symmetry breaking in commensurate graphene rotational stacking: Comparison of theory and experiment. *Phys. Rev. B* **83,** 205403 (2011).

8. Lui, C. H., Li, Z., Mak, K. F., Cappelluti, E. & Heinz, T. F. Observation of an electrically tunable band gap in trilayer graphene. *Nat. Phys.* **7,** 944–947 (2011).

9. Castro, E. V. *et al.* Biased bilayer graphene: Semiconductor with a gap tunable by the electric field effect. *Phys. Rev. Lett.* **99,** (2007).

10. Zhang, Y. *et al.* Direct observation of a widely tunable bandgap in bilayer graphene. *Nature* **459,** 820–3 (2009).

11. MacDonald, A. H. & Bistritzer, R. Materials science: Graphene moiré mystery solved? *Nature* **474,** 453–4 (2011).

12. Li, X. *et al.* Large-area graphene single crystals grown by low-pressure chemical vapor deposition of methane on copper. *J. Am. Chem. Soc.* **133,** 2816–9 (2011).

13. Bae, S. *et al.* Roll-to-roll production of 30-inch graphene films for transparent electrodes. *Nat. Nanotechnol.* **5,** 574–8 (2010).

14. Reina, A. *et al.* Large area, few-layer graphene films on arbitrary substrates by chemical vapor deposition. *Nano Lett.* **9,** 30–5 (2009).

15. Lui, C. H. *et al.* Imaging stacking order in few-layer graphene. *Nano Lett.* **11,** 164–9 (2011).

16. Nelson, F., Diebold, A. C. & Hull, R. Simulation Study of Aberration-Corrected High-Resolution Transmission Electron Microscopy Imaging of Few-Layer-Graphene Stacking. *Microsc. Microanal.* **16,** 194–199 (2010).

17. Huang, P. Y. *et al.* Grains and grain boundaries in single-layer graphene atomic patchwork quilts. *Nature* **469,** 389–92 (2011).

18. Kim, K. *et al.* Grain boundary mapping in polycrystalline graphene. *ACS Nano* **5,** 2142–6 (2011).

19. Meyer, J. C. *et al.* The structure of suspended graphene sheets. *Nature* **446,** 60–3 (2007).

20. Dienwiebel, M. *et al.* Superlubricity of Graphite. *Phys. Rev. Lett.* **92,** 126101 (2004).

21. Yan, K., Peng, H., Zhou, Y., Li, H. & Liu, Z. Formation of bilayer bernal graphene: layer-by-layer epitaxy via chemical vapor deposition. *Nano Lett.* **11,** 1106–10 (2011).

22. Yu, Q. *et al.* Control and characterization of individual grains and grain boundaries in graphene grown by chemical vapour deposition. *Nat. Mater.* **10,** 443–9 (2011).

23. Jhang, S. *et al.* Stacking-order dependent transport properties of trilayer graphene. *Phys. Rev. B* **84,** (2011).

24. Lee, S., Lee, K. & Zhong, Z. Wafer scale homogeneous bilayer graphene films by chemical vapor deposition. *Nano Lett.* **10,** 4702–7 (2010).

25. Liu, Z., Suenaga, K., Harris, P. & Iijima, S. Open and Closed Edges of Graphene Layers. *Phys. Rev. Lett.* **102,** (2009).

26. Bacon, G. E. The interlayer spacing of graphite. *Acta Crystallogr.* **4,** 558–561 (1951).

27. Lalena, J. N., Cleary, D. A. & Weiser, M. W. *Principles of Inorganic Materials Design*. (John Wiley and Sons, 2010).

28. Ruiz-Vargas, C. S. *et al.* Softened elastic response and unzipping in chemical vapor deposition graphene membranes. *Nano Lett.* **11,** 2259–63 (2011).

29. Lahiri, J., Lin, Y., Bozkurt, P., Oleynik, I. I. & Batzill, M. An extended defect in graphene as a metallic wire. *Nat. Nanotechnol.* **5,** 326–9 (2010).

30. Alden, J. S. *et al.* Strain solitons and topological defects in bilayer graphene. *Proc. Natl. Acad. Sci. U. S. A.* **110,** 11256–60 (2013).

31. Ju, L. *et al.* Topological valley transport at bilayer graphene domain walls. *Nature* **520,** 650–655 (2015).

32. Kim, C.-J. *et al.* Stacking order dependent second harmonic generation and topological defects in h-BN bilayers. *Nano Lett.* **13,** 5660–5 (2013).

33. Liu, Z. *et al.* Observation of Microscale Superlubricity in Graphite. *Phys. Rev. Lett.* **108,** 205503 (2012).

34. Martin, J. M. *et al.* Superlubricity of MoS2: crystal orientation mechanisms. *Surf. Coatings Technol.* **68-69,** 427–432 (1994).

35. Leven, I., Krepel, D., Shemesh, O. & Hod, O. Robust Superlubricity in Graphene/ h -BN Heterojunctions. *J. Phys. Chem. Lett.* **4,** 115–120 (2013).

36. Wang, L.-F. *et al.* Superlubricity of two-dimensional fluorographene/MoS2 heterostructure: a first-principles study. *Nanotechnology* **25,** 385701 (2014).

37. Mele, E. J. Interlayer coupling in rotationally faulted multilayer graphenes. *arxiv.org* 23 (2011).

38. Kaczér, J. & Kroupa, F. The determination of strain by mechanical interference. *Czechoslov. J. Phys.* **1,** 80–85 (1952).

39. Hashimoto, H. & Uyeda, R. Detection of dislocation by the Moiré pattern in electron micrographs. *Acta Crystallogr.* **10,** 143–143 (1957).

# CHAPTER 5

# ALIGNED GRAPHENE AND *h*-BN AS 2D HETEROSTRUCTURE BUILDING BLOCKS

## 5.1 Introduction

As discussed in previous chapters, chemical vapor deposition (CVD) on copper (Cu) provides a powerful growth technique for realizing large-scale graphene films in an inexpensive and simple way, enabling their production up to meter scale[1,2]. However, these films do not exhibit crystalline alignment over distances critical to the large-scale production of spatially uniform vertical heterostructures. For example, CVD grown graphene films are usually comprised of small, randomly rotated grains (see Chapter 3, Section 3.2) [3,4] and even though some recipes can create graphene grains nearly one centimeter in size (see Chapter 3, Section 3.3)[5,6], neighboring grains rarely maintain a common orientation[7].

Previous studies have shown that controlling the graphene crystallinity requires ordered substrates with strong templating interactions during growth. For instance, graphene deposited on the symmetry-matched surface lattices of certain single crystal metals, including ruthenium (0001), iridium (111), rhodium (111), and Cu (111), can follow the substrate's rotational orientation under specific growth conditions, as can be seen in the examples in Figure 5.1[6]. An example is the growth of a graphene film aligned over 1 mm on a sputtered Cu (111) film[8]. A 2014 paper by Lee *et al*[9] has demonstrated aligned graphene growth on 5 cm germanium (110) wafers. Graphene, although generally not a single layer, can also be grown epitaxially on silicon carbide

(SiC) substrates. These aligned growth methods, however, all suffer from complicated and expensive substrate preparation[8,9] or transfer procedures.[10]

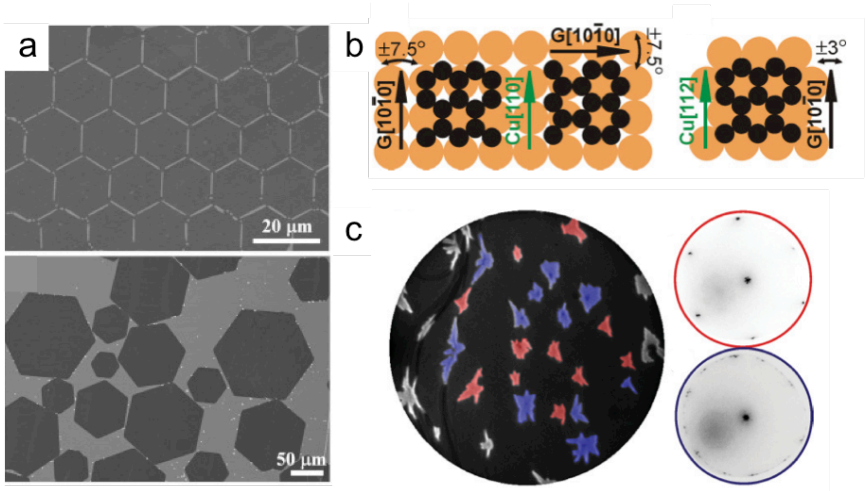


**Figure 5.1: Aligned graphene overview. a,** graphene grown on molten Cu achieves an ordered structure in some areas (top) but not in others (bottom). Reproduced from [11]. **b,** Illustration of graphene alignment on a cubic Cu (100) surface, showing two preferred orientations (left), but only one preferred orientation on a trigonal Cu (111) surface. **c,** The effect of surface defects on grain uniformity, where the aligned red grains nucleated on flat surfaces, and the blue polycrystalline grains nucleated on surface defects. Reproduced from [12]

In this chapter we report the scalable growth of aligned single layer graphene and hexagonal boron nitride (*h*-BN) on commercial copper foils, where each film originates from multiple nucleations yet exhibits a single orientation. Thorough characterization of our graphene films reveals uniform crystallographic and electronic structures on length scales ranging from nanometers to tens of centimeters. As we demonstrate with artificial twisted graphene bilayers, these inexpensive and versatile films are ideal building blocks for large-scale layered heterostructures with angle-tunable optoelectronic properties. This section is largely adapted from L. Brown, *et al*., ***Nano Letters***, 14, 5706–5711 (2014), and describes work done mainly in

collaboration with E. Lochocki on the growth and characterization of aligned graphene and *h*-BN films.

## 5.2 Crystalline Film Alignment

Our method relies on two key factors: 1) Cu foil recrystallization and 2) growth parameters optimized for reduced reactivity (see Figure 5.2a). First, we produce long-range crystallinity in the Cu foil (Nilaco Corporation, #CU-113213, 99.9% purity) by annealing it for up to twelve hours at a temperature of 1030 °C, which is close to its melting point, in an $Ar/H_2$ environment. This procedure generates a single Cu(111) domain with a spatially uniform in-plane orientation over the entire foil, which we have verified up to 16 cm using bulk sensitive Laue X-ray diffraction (XRD) (Figure 5.2, insets) and surface sensitive spatially-resolved backscatter electron diffraction (BSED) (Figure 5.6a).

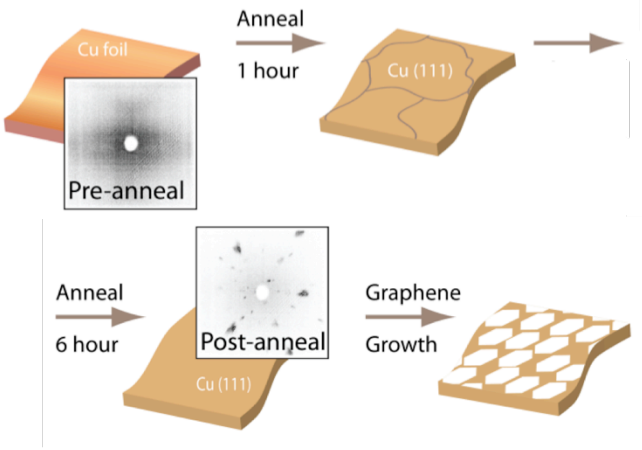


**Figure 5.2: Schematics showing the graphene growth process**, where Cu foil is annealed to create large Cu(111) grains. Insets: Laue diffraction taken on pre-anneal (left) and post-anneal (right) Cu foils.

Second, graphene or *h*-BN is grown using carefully chosen growth parameters that reduce the nucleation density[6], suppress bilayer growth[13,14], and, most importantly, favor angular correlation between graphene or *h*-BN grains and the underlying Cu(111) surface[15,16]. As mentioned in Chapter 1, *h*-BN can be grown via CVD on Cu substrates, similar to graphene[17]. The final results are continuous graphene and *h*-BN films (Figure 5.3b, middle and Figure 5.3c, bottom, respectively); however, we often intentionally limit the growth time to produce a partial coverage that facilitates characterization of individual grains (Figure 5.3a and Figure 5.3c, top).

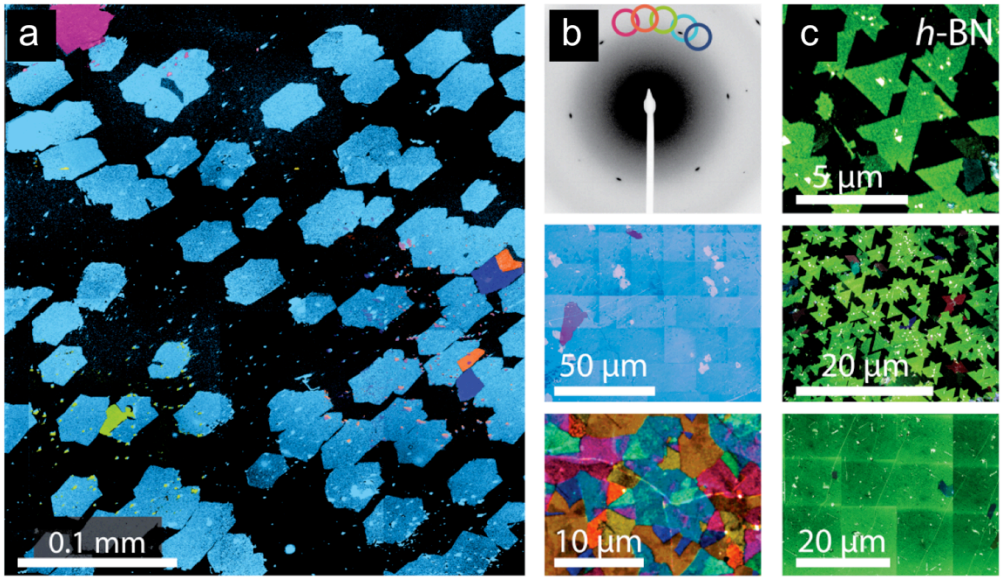


**Figure 5.3: DF-TEM images of aligned graphene and *h*-BN. a,** False-color DF-TEM image of a partial-coverage aligned graphene monolayer, where color indicates different crystalline orientations. **b,** Diffraction pattern explaining the DF-TEM color scheme, with colored circles indicating crystalline angle (top). Comparison of false-color DF-TEM images of a continuous aligned graphene monolayer (middle) and monolayer graphene with randomly oriented grains (bottom). **c,** False-color DF-TEM images of a partial-coverage aligned *h*-BN monolayer showing typical grain shape (top) and long-range alignment (middle). Bottom: False-color DF-TEM image of a continuous aligned *h*-BN film.

The resulting graphene and *h*-BN films display uniform crystalline alignment, as we confirm using several microscopy and spectroscopy techniques. In Figure 5.3 we show false-colored dark field transmission electron microscope (DF-TEM) images of the graphene and *h*-BN transferred onto TEM grids, where each color represents a specific crystallographic orientation (Figure 5.3b, top)[3]. In partial-coverage graphene (Figure 5.3a), the majority of the islands (blue) have similar orientations across the imaged area (~300 μm), which is representative of the entire sample; this crystalline uniformity was also observed on continuous graphene films (Figure 5.3b, middle).

This is in stark contrast to the properties of graphene films grown under different conditions; for example, a graphene sample grown using a method reported by Li *et al*.[2] exhibits small, randomly oriented graphene grains (Figure 5.3b, bottom). We also find in Figure 5.3c that the partial-coverage and continuous monolayer *h*-BN grown on our annealed Cu foil displays characteristically triangular domains with a long range alignment of the B-N bond orientation (but not the polarity), while other growths lack this alignment[18]. Further experiments, in which we vary the growth rate or change the substrate, confirm that the substrate preparation and growth conditions discussed above are essential for the creation of aligned graphene and *h*-BN films (see more details in Supplementary Information for [19]).

## 5.3 Uniform Electronic Structure

Extending this promising growth technique to larger areas and using the resulting aligned films in stacked electronic and optoelectronic devices will require quantitative knowledge regarding both the film-substrate rotational alignment and the uniformity

of the electronic structure between different grains. We investigate these properties below for the case of graphene. Angle resolved photoemission spectroscopy (ARPES) is an ideal characterization tool, as it is sensitive to both the film and its Cu substrate and can easily distinguish between the two. In particular, we simultaneously perform two types of ARPES measurements, an innovative capability of the ANTARES beamline at the SOLEIL synchrotron. Conventional ARPES with a 90 μm photon beam spot ($\mu$-ARPES) directly measures the *k*-resolved electronic structure averaged over multiple grains, while nano-spot ARPES with a 200 nm photon beam spot (*n*-ARPES) can probe a single grain.

A comparison between single- and multi-grain ARPES Fermi surface maps (Figure 5.4a and b) reveals the precise graphene inter-grain and graphene-Cu alignments. A *n*-ARPES Fermi surface map acquired from the center of a single grain (Figure 5.4a; located using a *n*-ARPES spatial map like the one in Figure 5.4c) appears nearly identical to a map taken from many grains with $\mu$-ARPES (Figure 5.4b).

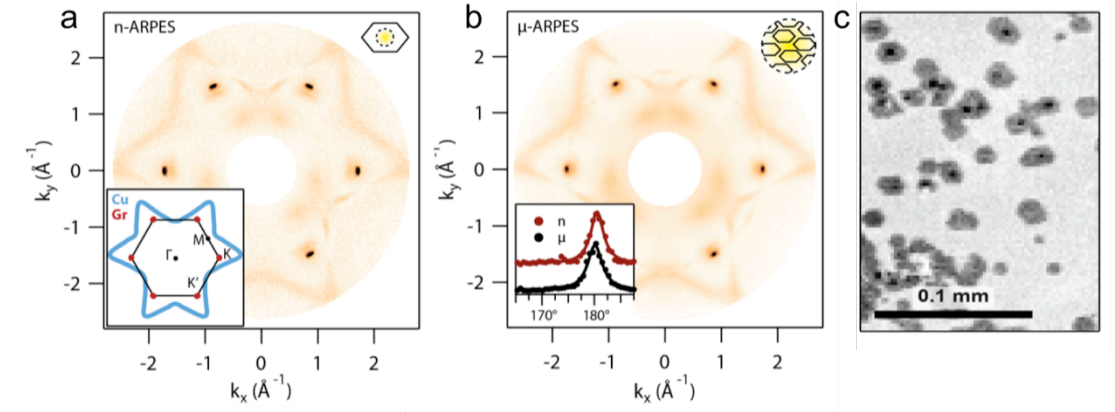


**Figure 5.4: Graphene-Cu lattice alignment and electronic properties. a,** Symmetrized *n*-ARPES Fermi surfaces showing photoelectron intensity integrated from ($E_F$ – 30 meV) to ($E_F$ + 10 meV), acquired from a single grain with a 200 nm photon spot; Inset: Schematics of the copper (blue) and graphene (red) features in (a) and (b). **b,** *μ*-ARPES Fermi surface similar to (a) but acquired using a 90 μm photon spot. Inset: nano- and *μ*-ARPES photoelectron intensity along an arc passing through one of the Dirac spots. **c,** 200 x 150 μm$^2$ (2 μm step size) *n*-ARPES spatial map showing aligned graphene grains. Small bilayer regions can be seen at the centers of some grains.

Both maps display six bright spots (red in inset of Figure 5.4 K and K' points. The angular widths of these spots (*n*-ARPES FWHM = 2.4°; *μ*-ARPES FWHM= 2.8°) are similar in the two maps, demonstrating that all grains measured with the large spot have nearly the same orientation (inset of Figure 5.4b). In addition to the graphene spots, both maps display faint star-shaped curves (blue in inset of Figure 5.4a) originating from the Cu substrate. These curves confirm that the copper surface has a (111) orientation with a single azimuthal domain, based on comparison to previous ARPES measurements[4,20] and density functional theory (DFT) calculations. Our key finding is that the two Fermi surfaces belonging to graphene and Cu are aligned to within 0.5°, as determined by the coincidence of the graphene Γ-M high symmetry axes with the Cu reflection symmetry axes.

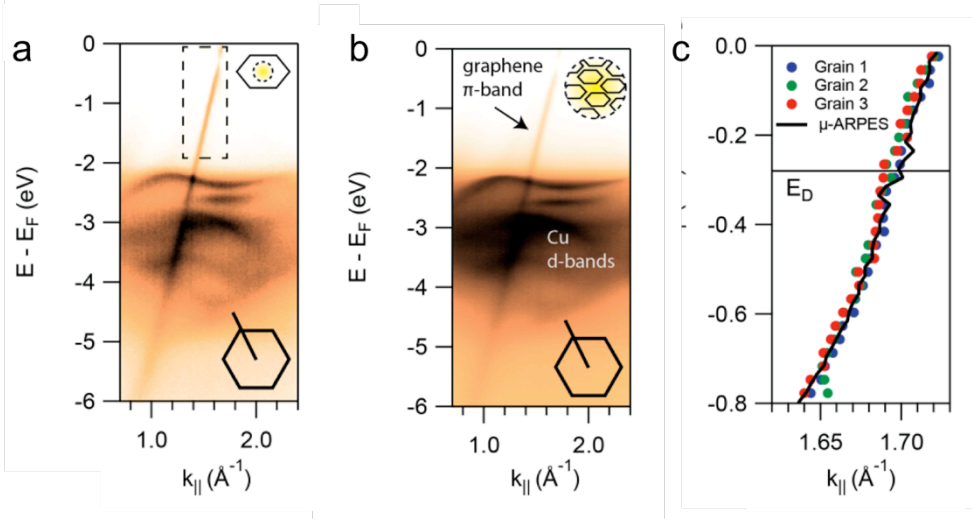


**Figure 5.5: The uniformity of graphene's electronic structure. a,** A valence band spectrum along the graphene Γ-K direction acquired in the center of a single graphene grain. Dotted box: region used to form map in (Figure 5.4c). **b,** A valence band spectrum along the graphene Γ-K direction using the 90 μm spot. **c,** Several Γ-K cuts acquired on separate individual graphene grains nearly 200 μm apart (colors), and a Γ-K cut acquired using the 90 μm spot (black).

In order to study the uniformity of the graphene's electronic structure, we present *k*-resolved spectra taken along the Γ-K direction both with *n*-ARPES (single grain; Figure 5.5a) and *μ*-ARPES (multi-grain; Figure 5.5b). They again show almost identical features, including a sharp graphene π-band and a manifold of Cu d-bands between 2-5 eV binding energy. For a more direct comparison, we plot the extracted dispersion of the graphene π-band taken from several different grains measured using *n*-ARPES (dots with different colors, Figure 5.5c) together with that of multi-grain *μ*-ARPES measurements (solid line, Figure 5.5c). Any spatial variations in the grain orientation, Fermi velocity, or doping level would be evident from these plots; instead, all dispersion curves show the same characteristics, ensuring highly uniform electrical and optical properties. From both our *n*-ARPES and *μ*-ARPES measurements, we extract a Fermi velocity of $1.04\pm0.03\times10^6$ m/s and a Dirac energy of 285±30 meV

(measured from the Fermi level, indicating electron doping), all in close agreement with previously reported values[4,21,22]. Altogether, our *n*-ARPES and $\mu$-ARPES data reveal a well-defined electronic structure (as expected from a single crystal) that exists despite its origin in many individual grains; the *n*-ARPES data in particular provides a quantitative understanding of inter-grain alignment that has been unavailable in previous ARPES studies of aligned graphene films[22].

## 5.4 Long-Range Copper Alignment

These observations suggest that our approach can generate an arbitrarily large graphene film with a crystalline electronic structure, and we demonstrate this ability below. First, the BSED data in Figure 5.6a confirm the large-scale alignment of our Cu foil after thermal recrystallization. Here, the constant color displayed in the out-of-plane (z) and in-plane (y) maps indicates a Cu(111) surface with a single rotational domain across the entire 12 cm sample (see optical image of the foil in Figure 5.7). After graphene growth, low energy electron diffraction (LEED) patterns (Figure 5.6b) acquired from several different spots (as far as 7 mm) on a single sample demonstrate the preservation of the graphene-Cu and graphene inter-grain alignment. This is evident in the presence of a single set of graphene diffraction spots with constant azimuthal orientation, as well as the apparent overlap of the graphene and copper spots. The optical images in Figure 5.7 are consistent with these measurements, showing the edges of the graphene islands to be aligned over an entire 2.5 cm sample.

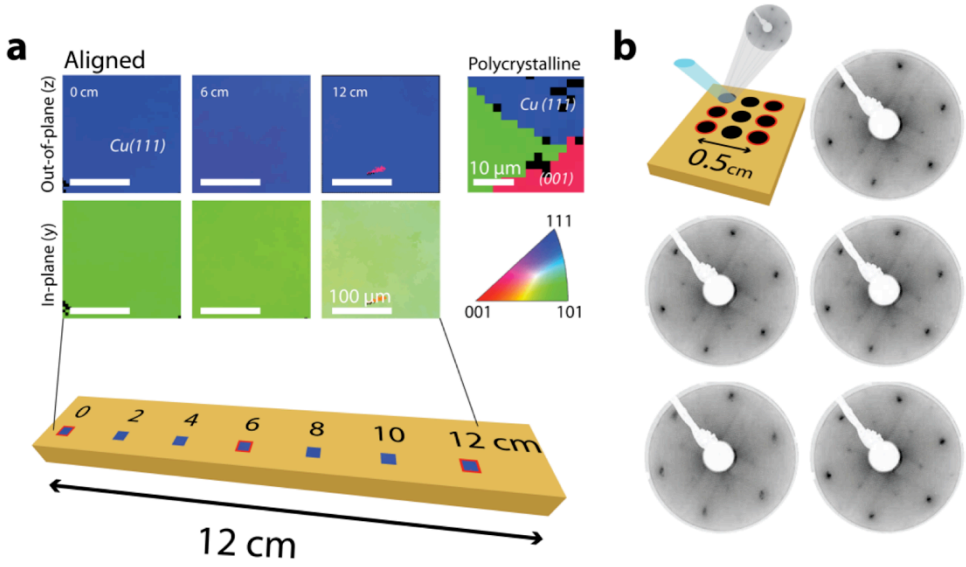


**Figure 5.6: Large scale Cu and graphene alignment. a,** Back-scatter electron diffraction maps taken over three 200 x 200 $\mu m^2$ areas across a 12 cm annealed Cu foil, to demonstrate the large-scale Cu alignment (bottom left). "Out-of-plane (z)" data represents the surface orientation, while the corresponding "In-plane (y)" measurements indicate azimuthal angle. For comparison, the right-most map shows polycrystalline Cu on a foil annealed for just one hour. Bottom right: key orientation color map. **b,** LEED patterns taken more than 7 mm apart on a single sample.

The graphene alignment can be characterized by the fraction of the Cu foil with a Cu(111) surface and by the percentage of aligned graphene grains on the Cu(111) areas. We estimate that 95% of the Cu foil is Cu(111) after thermal recrystallization, based on our optical images. After growth, 95% of the graphene grown on the Cu(111) facet shares the same orientation, based on our ARPES and DF-TEM data. These results represent a significant improvement over existing studies and point to strategies for increasing the overall alignment. For example, we note that the end result of an annealing process is extremely sensitive to the initial state of the material. For this reason, manufacturing processes play a large role in determining the post-anneal surface of a Cu foil: cold-rolled Cu foil typically recrystallizes with a

Cu(001) surface after a long anneal[23,24], while electrodeposited foils are able to provide various recrystallized surface planes[25,26]. Certain annealing conditions can even produce multi-faceted surfaces from cold-rolled Cu[27].

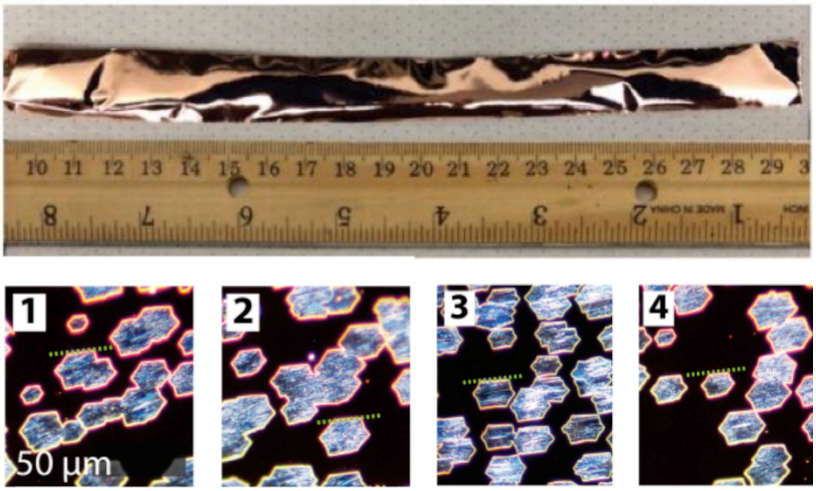


**Figure 5.7: Optical image of aligned graphene.** Top: Large post-anneal Cu foil. The contrast in the optical image is caused by macroscopic bending of the copper foil. Bottom: optical dark-field images of the graphene on the Cu foil taken from the locations separated by 1 cm, where dotted lines (green) highlight the graphene edge orientation.

The high efficiency of thermal recrystallization in the polycrystalline Nilaco foil is likely facilitated by a manufacturing process, which produced a favorable distribution of surface orientations and grain sizes. Optimization of foil production in conjunction with ideal annealing conditions could therefore further improve the efficiency of the thermal recrystallization. In terms of growth, the complex interplay between a growing graphene grain and the Cu surface beneath it can contribute to misalignment. Attempts at growth on molten copper[11] encounter limited film alignment due to the highly malleable Cu surface. Even for a (111) surface, growth dynamics have been found to depend sensitively on thermodynamic variables such as

temperature and pressure[28], surface morphology and defects[15,29], and relative growth orientation[30]. Further control of the growth process can be achieved by applying results from recent studies[6].

## 5.5 Aligned Graphene as Building Blocks for Graphene Heterostructures

Large scale 2D films with structural uniformity, such as our aligned graphene and *h*-BN films, are ideal building blocks for artificial stacked materials that require precise control of the interlayer rotation angle θ. Initial exploration of this rotational degree of freedom, which is not accessible to layered synthesis techniques like molecular beam epitaxy (MBE) or pulsed laser deposition (PLD), has already revealed several θ-dependent electrical and optical phenomena in bilayers of graphene[31,32], *h*-BN[33], and molybdenum disulfide ($MoS_2$)[34], as well as graphene/*h*-BN heterostructures[35–38]. As mentioned in Chapter 1, tuning these θ-dependent behaviors on macroscopic scales has been untenable so far, as CVD grown bilayers exhibit multiple interlayer rotations (see Chapter 3)[39], and stacked polycrystalline layers result in physical properties averaged over many random θ domains.

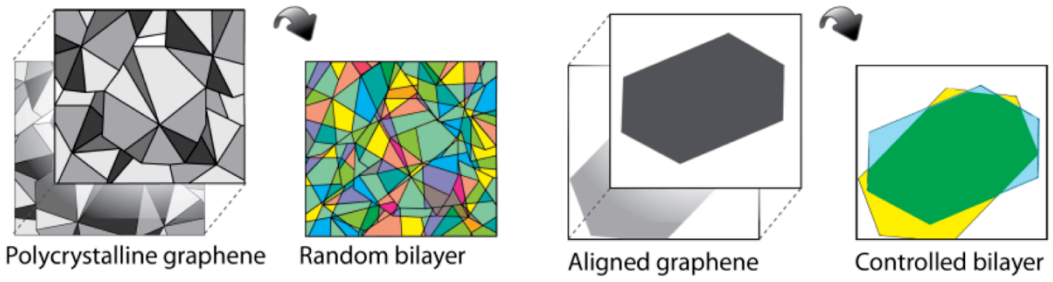


**Figure 5.8: Illustrations showing the benefits of aligned graphene** (right) in artificial stacks as opposed to graphene with randomly-oriented grains (left).

Figure 5.8 illustrates the benefits of using aligned single layer films as building blocks for angle controlled layered 2D structures. Using our aligned films, it is possible to create uniform heterostructures over large scales, with geometries that were previously unavailable, such as low-θ twisted bilayer graphene (tBLG), chiral 2D stacks, and stacks combining several 2D materials. Below we demonstrate the creation of angle-uniform tBLG stacks, and examine their uniformity over large scales.

### 5.5.1 Large-Scale twisted Bilayer Graphene Structures

The next step in creating graphene heterostructures is the development of a reproducible, θ-controlled transfer method for layer-by-layer assembly, accurately controlling the relative twist angle θ at each transfer step. We can fabricating tBLG with a controlled θ using a custom-made X-Y-Z-θ transfer stage[40]. The transfer process is done in a way that maintains information regarding the relative crystalline orientation of each graphene sheet, based on the orientation of their Cu substrate. First, a thick PMMA layer is spun on the graphene as transfer support (PMMA: 495K, 8% in Anisol, Micro-chem. Spin casting: 3000 rpm, 60 sec), enabling the transfer of areas up to 1 $cm^2$. A support frame of thermal release tape (TRT) is attached to PMMA/graphene/Cu stack, and the Cu is etched. Since neighboring pieces share the same orientation, they can be transferred one by one using the aligned transfer setup in an angle controlled way. Each transfer was followed by a short anneal to promote interlayer adhesion (10 minutes, 350 °C), and an acetone/IPA wash.

### 5.5.2 Angle Uniformity in Engineered twisted Bilayer Graphene

Figure 5.9 shows preliminary results for fabricated artificial tBLG stacks. We confirm the quality of their coupling using DUV-Vis-IR hyperspectral imaging (see Chapter 2 and reference [31] for details on the method), where two coupled graphene layers exhibit an optical absorption peak whose energy has a precisely known relationship to θ. Our spatial absorption peak maps shown in Figure 5.9a (bottom) confirm the spatial angle uniformity of our artificial tBLG.

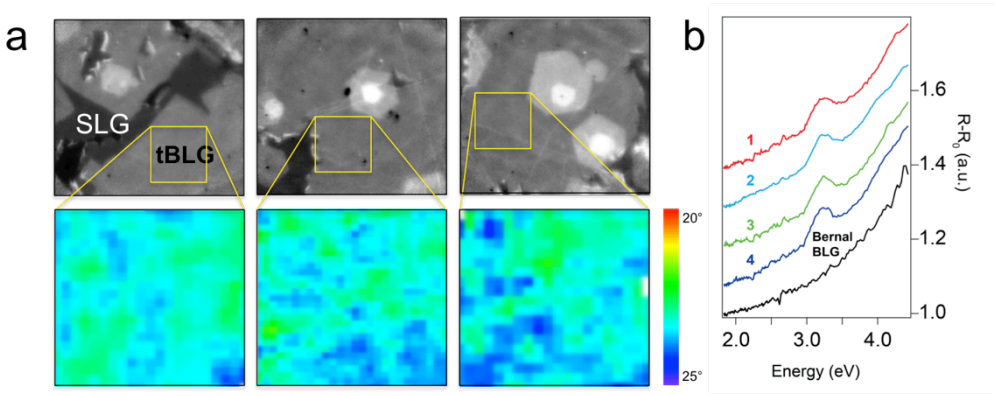


**Figure 5.9: Hyperspectral imaging of artificial tBLG. a**, Optical reflection images of artificial tBLG **b**, Optical reflection spectra at different locations on a single tBLG sample on a fused silica substrate, compared to Bernal stacked bilayer graphene (black curve). In this geometry, the differential change in reflection due to the graphene, ΔR/R, is proportional to the graphene's absorption. Spectra are offset for clarity. Inset: schematic indicating the location where each spectrum was taken.

Optical spectra taken in different locations on our tBLG are shown in Figure 5.9b; each region exhibits a peak with almost identical position, magnitude, and width confirming the effective interlayer coupling and the tight angular spread, with the energy (~ 3.2 eV) corresponding to θ ~ 20˚. Area histograms of θ similarly measured from two separate samples are shown in Figure 5.10, demonstrating the spatial

uniformity of our large-scale tBLG with different average θ. The two samples show sharp peaks in the histogram with FWHMs of 1.3˚ and 1.4˚, which include 88% and 93% of the total bilayer areas, respectively.

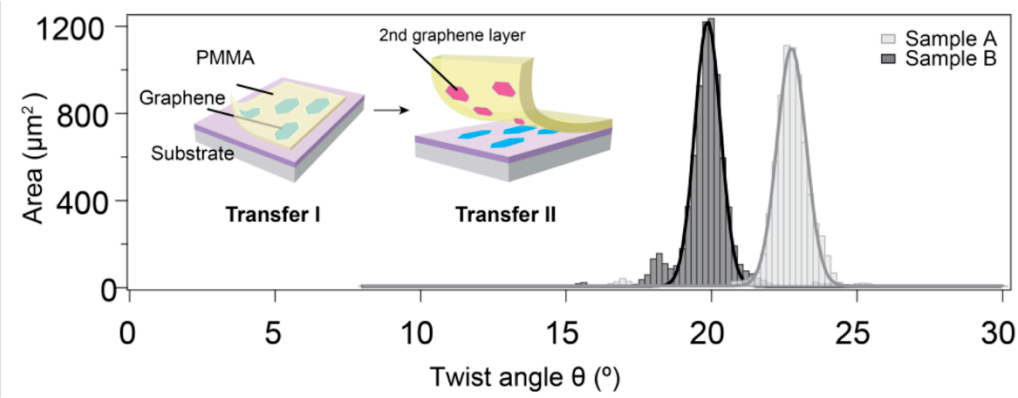


**Figure 5.10: Angle uniformity of artificially stacked tBLG.** Histogram of area vs. twist angle compiled from hyperspectral absorption measurements taken from two samples, over an area of 400 x 400 $mm^2$ each. Superimposed in (b) are Gaussian fits to the histograms. The peak position ($\theta_p$) and full with at half maximum (FWHM) are ($\theta_p$, FWHM) = (19.9˚, 1.3˚) and (22.8˚,1.4˚) for the two samples. Inset: Illustration of the aligned transfer process.

This data suggests that this aligned transfer technique can directly control θ, thus engineering its optical properties over large area. Additionally, it suggests that the multiple transfer processes do not damage the layers' ability to form effective interlayer coupling, enabling the creation of complex multilayered structures.

While the well-defined crystalline orientation of our films successfully eliminates the predominant source of non-uniformity, still significant challenges remain in order to efficiently construct more complicated graphene layered structures. First, θ precision should be improved, since the current error Δθ is close to ±1.5°, as described above. For this, better scaffolds for handling graphene during transfer should be developed, in order to minimize any structural distortion such as wrinkling,

shearing, folding, drifting and rotation[41]. Second, a better method for inducing a uniform interlayer contact is needed. The currently used method of thermal annealing is insufficient due to contaminations introduced by the supporting transfer polymer and trapped between the layers. These advances will improve the quality of artificial tBLG and the performance of artificial 2D layered devices.

## 5.6 Conclusion

In conclusion, we presented a scalable method for growing single layer graphene and *h*-BN on inexpensive Cu foils which results in films with uniform orientation and electronic structure potentially over arbitrarily large distances. We then use these films to create homogeneously oriented tBLG with a uniform twist angle throughout. We create artificial tBLG films with predetermined θ, and determine the average angle dispersion to be $\Delta\theta \pm 1.5°$ across the sample. These proof-of-concept structures pave the way to other, more complex structures, which will enable us to explore previously unavailable regimes. These include low-θ tBLG, chiral 2D stacks, and stacks with two or more 2D materials.

Although significant breakthroughs have been achieved, such as the growth of uniform single layer graphene and *h*-BN layers, and their controlled transfer, still many challenges remain. These include the further optimizing and scaling the Cu recrystallization process, understanding the detailed growth dynamics, creating a stronger transfer scaffold to better maintain the orientation uniformity, and the growth of other 2D materials, such as the semiconductors $MoS_2$ and $MoSe_2$, with large-scale crystalline alignment.

Nonetheless, the concepts of our growth method demonstrate great promise as they can be generalized for growing other uniform 2D materials grown on recrystallized metal surfaces. Furthermore, our results offer new avenues for implementing 2D materials in real-world devices, as well as exploring new phases of electronic matter in heterostructures based on 2D materials.

REFERENCES


1. Bae, S. *et al.* Roll-to-roll production of 30-inch graphene films for transparent electrodes. *Nat. Nanotechnol.* **5,** 574–8 (2010).

2. Li, X. *et al.* Large-area synthesis of high-quality and uniform graphene films on copper foils. *Science* **324,** 1312–4 (2009).

3. Huang, P. Y. *et al.* Grains and grain boundaries in single-layer graphene atomic patchwork quilts. *Nature* **469,** 389–92 (2011).

4. Avila, J. *et al.* Exploring electronic structure of one-atom thick polycrystalline graphene films: a nano angle resolved photoemission study. *Sci. Rep.* **3,** 2439 (2013).

5. Hao, Y. *et al.* The role of surface oxygen in the growth of large single-crystal graphene on copper. *Science* **342,** 720–3 (2013).

6. Yan, Z., Peng, Z. & Tour, J. M. Chemical Vapor Deposition of Graphene Single Crystals. *Acc. Chem. Res.* **47,** 1327–1337 (2014).

7. Wu, Y. A. *et al.* Large single crystals of graphene on melted copper using chemical vapor deposition. *ACS Nano* **6,** 5010–7 (2012).

8. Ogawa, Y. *et al.* Domain Structure and Boundary in Single-Layer Graphene Grown on Cu(111) and Cu(100) Films. *J. Phys. Chem. Lett.* **3,** 219–226 (2012).

9. Lee, J.-H. *et al.* Wafer-scale growth of single-crystal monolayer graphene on reusable hydrogen-terminated germanium. *Science* **344,** 286–9 (2014).

10. Kim, J. *et al.* Layer-Resolved Graphene Transfer via Engineered Strain Layers. *Science* **342,** 833–836 (2013).

11. Geng, D. *et al.* Uniform hexagonal graphene flakes and films grown on liquid copper surface. *Proc. Natl. Acad. Sci. U. S. A.* **109,** 7992–6 (2012).

12. Nie, S., Wofford, J. M., Bartelt, N. C., Dubon, O. D. & McCarty, K. F. Origin of the mosaicity in graphene grown on Cu(111). *Phys. Rev. B* **84,** 155425 (2011).

13. Fang, W. Bilayer graphene growth by low pressure chemical vapor deposition on copper foil. (Massachusetts Institute of Technology, 2012). at <http://hdl.handle.net/1721.1/75656>

14. Kim, K. K. *et al.* Synthesis of monolayer hexagonal boron nitride on Cu foil using chemical vapor deposition. *Nano Lett.* **12,** 161–6 (2012).

15. Nie, S., Wofford, J. M., Bartelt, N. C., Dubon, O. D. & McCarty, K. F. Origin of the mosaicity in graphene grown on Cu(111). *Phys. Rev. B* **84,** 155425 (2011).

16. Roth, S., Matsui, F., Greber, T. & Osterwalder, J. Chemical vapor deposition and characterization of aligned and incommensurate graphene/hexagonal boron nitride heterostack on Cu(111). *Nano Lett.* **13,** 2668–75 (2013).

17. Kim, K. K. *et al.* Synthesis of monolayer hexagonal boron nitride on Cu foil using chemical vapor deposition. *Nano Lett.* **12,** 161–6 (2012).

18. Joshi, S. *et al.* Boron nitride on Cu(111): an electronically corrugated monolayer. *Nano Lett.* **12,** 5821–8 (2012).

19. Brown, L. *et al.* Polycrystalline graphene with single crystalline electronic structure. *Nano Lett.* **14,** 5706–11 (2014).

20. Walter, A. L. *et al.* Electronic structure of graphene on single-crystal copper substrates. *Phys. Rev. B* **84,** 195443 (2011).

21. Avouris, P., Chen, Z. & Perebeinos, V. Carbon-based electronics. *Nat. Nanotechnol.* **2,** 605–15 (2007).

22. Ago, H. *et al.* Epitaxial Growth and Electronic Properties of Large Hexagonal Graphene Domains on Cu(111) Thin Film. *Appl. Phys. Express* **6,** 075101 (2013).

23. Campbell, F. C. *Elements of metallurgy and engineering alloys*. (ASM International, 2008).

24. Wilson, N. R. *et al.* Weak mismatch epitaxy and structural feedback in graphene growth on copper foil. *Nano Res.* **6,** 99–112 (2013).

25. Pick, H. J., Storey, G. G. & Vaughan, T. B. The structure of electrodeposited copper—I: An experimental study of the growth of copper during electrodeposition. *Electrochim. Acta* **2,** 165–176 (1960).

26. Merchant, H. D., Liu, W. C., Giannuzzi, L. A. & Morris, J. G. Grain structure of thin electrodeposited and rolled copper foils. *Mater. Charact.* **53,** 335–360 (2004).

27. Murdock, A. T. *et al.* Controlling the orientation, edge geometry, and thickness of chemical vapor deposition graphene. *ACS Nano* **7,** 1351–9 (2013).

28. Li, X. *et al.* Graphene films with large domain size by a two-step chemical vapor deposition process. *Nano Lett.* **10,** 4328–34 (2010).

29. Batzill, M. The surface science of graphene: Metal interfaces, CVD synthesis, nanoribbons, chemical modifications, and defects. *Surf. Sci. Rep.* **67,** 83–115 (2012).

30. Jiang, H., Wu, P., Hou, Z., Li, Z. & Yang, J. Orientation-sensitive nonlinear growth of graphene: An epitaxial growth mechanism determined by geometry. *Phys. Rev. B* **88,** 54304 (2013).

31. Havener, R. W. *et al.* Hyperspectral imaging of structure and composition in atomically thin heterostructures. *Nano Lett.* **13,** 3942–6 (2013).

32. Kim, Y. *et al.* Breakdown of the Interlayer Coherence in Twisted Bilayer Graphene. *Phys. Rev. Lett.* **110,** 096602 (2013).

33. Li, Y. *et al.* Probing Symmetry Properties of Few-Layer MoS2 and h-BN by Optical Second-Harmonic Generation. *Nano Lett.* **13,** 3329–33 (2013).

34. Hsu, W.-T. *et al.* Second Harmonic Generation from Artificially Stacked Transition Metal Dichalcogenide Twisted Bilayers. *ACS Nano* **8,** 2951–2958 (2014).

35. Dean, C. R. *et al.* Hofstadter's butterfly and the fractal quantum Hall effect in moiré superlattices. *Nature* **497,** 598–602 (2013).

36. Geim, A. K. & Grigorieva, I. V. Van der Waals heterostructures. *Nature* **499,** 419–25 (2013).

37. Hunt, B. *et al.* Massive Dirac Fermions and Hofstadter Butterfly in a van der Waals Heterostructure. *Science* (2013).

38. Ponomarenko, L. A. *et al.* Cloning of Dirac fermions in graphene superlattices. *Nature* **497,** 594–7 (2013).

39. Lu, C.-C. *et al.* Twisting bilayer graphene superlattices. *ACS Nano* **7,** 2587–94 (2013).

40. Kim, C.-J., Levendorf, M. & Park, J. *Internal communication*.

41. Beechem, T. E., Ohta, T., Diaconescu, B. & Robinson, J. T. Rotational Disorder in Twisted Bilayer Graphene. *ACS Nano* **8,** 1655–1663 (2014).

# CHAPTER 6

# CONCLUSIONS AND OUTLOOK

## 6.1 Conclusions

Graphene has attracted increasing interest for its potential in new fields of research and technology[1–4]. An exciting possibility is the incorporation of graphene and other 2D materials in rationally designed van der Waals (vdW) heterostructures with engineered properties. In this thesis we provided a framework for the creation of such heterostructures, and demonstrate it with artificially stacked graphene multilayers. This framework includes several aspects: first, the imaging capability required to comprehend the structure of these stacks and the relationship between their structure and their optical, electronic, and mechanical properties. Second, the ability to create large-scale, uniform single layer building blocks for the methodical construction of vdW stacks. Finally, the ability to transfer these building blocks in a large-scale, precise, clean, angle-controlled, and repeatable way.

We reported a method for imaging the structural varieties in graphene stacks. We image the long-range atomic registry for oriented bilayer and trilayer graphene, and report the lack of long-range registry in twisted graphene multilayers. We also observe two kinds of strain-induced deformations: we find a high density of twinned domains in oriented multilayer graphene, connected by discreet twin boundaries. In contrast, individual layers in twisted regions continuously stretch and shear independently, forming elaborate Moiré patterns. These results can be understood in terms of an angle-dependent interlayer potential model, and can be adapted to

understand the structure of *h*-BN stacks[5], as well as other 2D crystals and their heterostructures.

Second, based on our understanding of CVD graphene growth, we reported a method for producing aligned single layers graphene and *h*-BN on centimeter scale. In this method the Cu foil acts as a templating substrate. We confirm the angular uniformity of the graphene film using DF-TEM images and ARPES band structure measurements. We observe single crystalline-like electronic structures with an orientation determined by the underlying Cu substrate. This growth is scalable as well; the Cu (111) planes are formed over 12 cm scale, as confirmed by the EBSD studies.

Finally, we report the development of a reproducible, θ-controlled transfer method for layer-by-layer assembly, accurately controlling the relative twist angle θ at each transfer step. We demonstrate this method by constructing twisted graphene stacks with controlled θ, and measuring their spatial and angular uniformity using hyperspectral microscopy imaging. These advances could be used to extend the field of atomically thin vdW materials into the discovery of new physical phenomena, as well as their commercial utilization.

## 6.2 Future Outlook

Our achievements illustrated in this thesis create a framework for the design and fabrication of 2D heterostructures with tunable physical properties. This framework opens up the possibility of creating vdW materials using the ever-growing library of 2D materials, and investigating their structure dependent physical properties[6]. Nonetheless, even graphene alone can inspire several interesting artificial structures in

regions that were previously unavailable, such as low-θ twisted BLG, large area Bernal stacked BLG, or chiral graphene stacks. Below we discuss these opportunities in more detail.

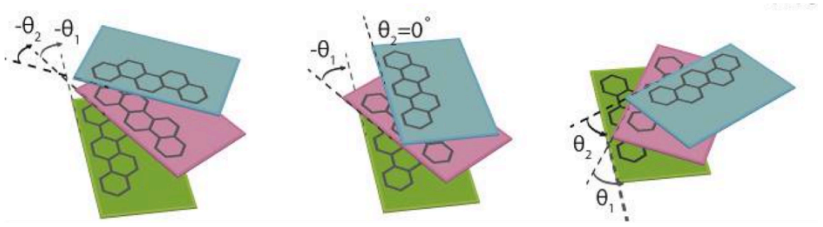


**Figure 6.1: Possible arrangements of trialyer graphene with different twist angles.** The right and left images show clockwise and counter clockwise chirality respectively, while the image in the center shows mirror symmetry.

### 6.2.1 Twist Bilayer Graphene With a Low Twist Angle

Some of the most interesting and novel physical phenomena are expected from low-θ tBLG ($\theta < 6°$). The proximity between the Fermi level and the vHSs at the cone crossing is expected to induce new physical phenomenon such as charge density waves, antiferromagnetism, and fermion-mediated superconductivity expected for highly doped single layer graphene[7]. Additionally, the vHS energies for low-θ tBLG are typically in the IR range, where there exist relatively few materials with tunable optical properties.

Our assembly method will allow for methodically creating and exploring the low-θ tBLG regime. Extracting their electronic band-structure is a critical step in developing an understanding of their properties. While previous scanning tunneling microscopy (STM) studies have demonstrated the existence of vHSs and renormalized Fermi velocities, their angular dependence often disagrees with theory, and many

studies report conflicting results[8]. More recently, ARPES conducted on tBLG has demonstrated vHSs and superlattice minigaps[9]. However, a systematic understanding of the continuous evolution of the band structure as a function of θ is lacking at this point, mainly due to the limitations of the sample preparation discussed earlier. For this, better angle control is critical. As the current accuracy remains close to 1°, only tBLG with θ > 1° can be made reliably.

As proof-of-concept we have successfully created several artificial tBLG samples with low-θ over a large area (~1 $cm^2$) on thin Cu film (sputtered Cu, 500 nm thick, growth method adapted from [10] and [11]). Importantly, despite PMMA residue due to the transfer, the samples were clean enough to perform highly surface sensitive experiment such as LEED and ARPES.

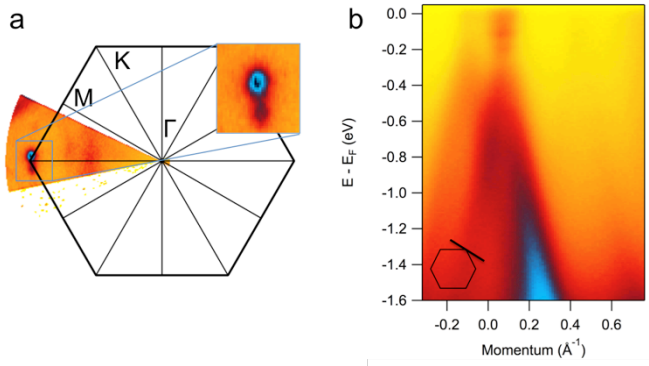


**Figure 6.2: ARPES data of low-θ artificial tBLG. a,** ARPES Fermi surface showing two bright spots (inset) near the K-point, which relate to the two twisted layers. **b,** Valence band spectrum perpendicular to the Γ-K direction (see inset) which cuts through both K-points, showing two Dirac cones.

In Figure 6.2 we show ARPES data taken at the ANTARES beamline in the SOLEIL synchrotron in France. This data was taken on an artificial tBLG sample on

Cu film with a twist angle of ~5°. The Fermi surface map in Figure 6.2a shows two distinct Dirac cones. The valence band cut in Figure 6.2b shows that both layers have similar doping and Fermi velocity. Further studies of these samples are underway, and could provide a unique outlook into the electronic properties of low twist-angle bilayer graphene.

### 6.2.2 Bernal Stacked Bilayer Graphene

Another exciting opportunity is the production of large scale Bernal stacked bilayer graphene. Despite its thermodynamic stability, its coverage during CVD growth is limited by the completion of the first growth as discussed in Chapter 3. Therefore, methods aimed to achieving full coverage of Bernal Stacked BLG are required. When two layers of aligned graphene are combined in tilt angle of 0° or 60°, the interlayer rotation becomes $\theta \sim 0°$. As we previously discussed in Chapter 4, the strong interlayer interaction in the low-$\theta$ regime drives most of the bilayer areas toward Bernal stacking, where mirror twins are separated by boundaries[12,13]. Our production method could potentially be used to engineer unique soliton structures, or to create a soliton-free Bernal stacked bilayer structures.

### 6.2.3 Chiral Twisted Bilayer Graphene and Multilayer Stacks

Our layer-by-layer transfer method with interlayer angle control allows for the creation of previously unexplored graphene structures, including chiral tBLG and multilayer stacks with novel symmetries. Using this method, it is straightforward to create chiral (left-handed vs. right-handed) multilayer graphene stacks (see Figure 6.3). The effects of chiral rotation have not been reported before, as the absolute

orientation of the stacks cannot be confirmed in exfoliated or in CVD grown graphene samples.

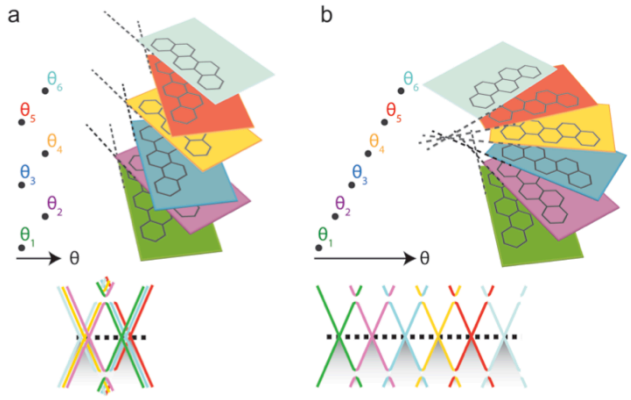


**Figure 6.3: Forms of ordered multilayer stacks (top) and their respective band structure near the k-point (bottom). a,** A-B-A-B- stack. **b,** Left handed chiral stack.

Multilayers with programmed θ also provide new approaches for further modulating the overall band structure and symmetry. This is schematically shown in Figure 6.3. Even with a single value of |θ|, multilayer variations with different symmetries could be created. For instance, alternating θ and -θ would result in a non-chiral multilayer graphene stack, with a band structure similar to that of tBLG (Figure 6.3a, bottom). Repeating θ for each transfer would create a chiral multilayer graphene stack (Figure 6.3b) with its electronic band structure with many periodic band crossings. Realization of chiral 2D system would lead to the fundamental understanding of the role of structural chirality in layered systems, as well as the creation of light sensitive ultra-thin heterostructures for potential polarization sensitive optoelectronic applications.

REFERENCES


1. Novoselov, K. S. *et al.* Two-dimensional gas of massless Dirac fermions in graphene. *Nature* **438,** 197–200 (2005).

2. Novoselov, K. S. *et al.* Electric field effect in atomically thin carbon films. *Science* **306,** 666–9 (2004).

3. Zhang, Y., Tan, J. W., Stormer, H. L. & Kim, P. Experimental observation of the quantum Hall effect and Berry's phase in graphene. *Nature* **438,** 201–204 (2005).

4. Lu, X., Yu, M., Huang, H. & Ruoff, R. S. Tailoring graphite with the goal of achieving single sheets. *Nanotechnology* **10,** 269–272 (1999).

5. Kim, C.-J. *et al.* Stacking order dependent second harmonic generation and topological defects in h-BN bilayers. *Nano Lett.* **13,** 5660–5 (2013).

6. Geim, A. K. & Grigorieva, I. V. Van der Waals heterostructures. *Nature* **499,** 419–25 (2013).

7. Nandkishore, R., Levitov, L. S. & Chubukov, A. V. Chiral superconductivity from repulsive interactions in doped graphene. *Nat. Phys.* **8,** 158–163 (2012).

8. Li, G. *et al.* Observation of Van Hove singularities in twisted graphene layers. *Nat. Phys.* **6,** 109–113 (2009).

9. Ohta, T. *et al.* Evidence for interlayer coupling and moiré periodic potentials in twisted bilayer graphene. *Phys. Rev. Lett.* **109,** 186807 (2012).

10. Ogawa, Y. *et al.* Domain Structure and Boundary in Single-Layer Graphene Grown on Cu(111) and Cu(100) Films. *J. Phys. Chem. Lett.* **3,** 219–226 (2012).

11. Brown, L. *et al.* Polycrystalline graphene with single crystalline electronic structure. *Nano Lett.* **14,** 5706–11 (2014).

12. Brown, L. *et al.* Twinning and twisting of tri- and bilayer graphene. *Nano Lett.* **12,** 1609–15 (2012).

13. Alden, J. S. *et al.* Strain solitons and topological defects in bilayer graphene. *Proc. Natl. Acad. Sci. U. S. A.* **110,** 11256–60 (2013).

# APPENDIX A

# GRAPHENE AS AN OXIDATION PROTECTIVE BARRIER

## A.1 Introduction

The potential of the applications of graphene is immense, with a variety of potential applications[1]. In this chapter we will present an application of graphene as an oxidation protection membrane for refined metals. The full potential of graphene as a protection layer can be understood based on its unique physical and chemical properties. First, surfaces of $sp^2$ carbon allotropes form a natural diffusion barrier thus providing a physical separation between the protected metal and reactants. This can be seen from the encapsulation of various atomic species inside of fullerenes[2] and carbon nanotubes at high temperatures and in vacuum[3]. More recently, graphene has been used to form a microscopic air-tight 'balloon'[4], which clearly demonstrates its property as an impermeable barrier. Second, graphene has exceptional thermal and chemical stability. Under an inert environment it is stable at extremely high temperatures (higher than 1500 ºC[5–7]) and it is also stable under many conditions where other substrates would undergo rapid chemical reactions. In fact, the latter property has been the key to the processes used to separate large scale graphene from the substrates where they are grown. Combined, these two properties (impermeability and thermal/chemical stability) alone would make graphene an excellent candidate for a novel protection layer. Furthermore, graphene offers several other unique benefits, such as optical transparency in visible wavelengths, electrically and thermally conductive, and it adds only about 0.34 nanometer per layer to the total dimension of

the coated metal. In sections adapted from S. Chen, L. Brown, *et al*., ***ACS Nano***, 5, 1321–1327, (2011), we demonstrate that graphene provides an excellent barrier against gaseous and liquid oxidation reagents, and examine the extent and limitations of its protection.

## A.2 Graphene as an Atomic Barrier

The use of refined metals is widespread, but they are often chemically reactive, requiring protective coatings for many applications. Protecting the surface of reactive metals has developed into a significant industry which employs many different approaches, including coating with organic layers[8–10], paints or varnishes[11], polymers[12], formation of oxide layers[13], anodization[14], chemical modification[15], and coating with other metals or alloys[16]. However, these conventional approaches can suffer from a variety of limitations, such as susceptibility to damage by heat, limited chemical stability, cost, and formation of waste products. In addition, most conventional methods modify the physical properties of metals being protected. The addition of a protective coating changes the dimensions of the metal due to the finite thickness of the coating, changes the appearance and the optical properties of the metal surface, and often decreases the electrical and thermal conductivity. One important approach to overcome these problems would be to develop a novel protection coating with an exceptional chemical and thermal stability with minimum changes to the physical properties of the protected metal. Graphene, with its exceptional mechanical, thermal, optical and electronic properties, is an excellent candidate for an atomically-thin oxidation protection membrane. For example,

previous reports show that the surface topography of metal substrates used to grow graphene is flat and smooth, significantly different than uncoated substrates[17], due to the atomic oxidation barrier provided by the graphene sheet[18]. In this chapter, we demonstrate the ability of graphene films grown by CVD to protect the surface of the metallic growth substrate (Cu and Cu/Ni alloys) from oxidation, both in air at elevated temperatures, as well as in aggressively oxidizing liquids such as hydrogen peroxide and sulfuric acid.

## A.3 Optical Observation of Metal Surface Protection

Large area graphene films were grown directly on Cu foils, Cu/Ni alloys using methane as a carbon source by CVD, using the method developed by Li *et al*[17], and their high quality was confirmed by micro-Raman spectroscopy (see Figure A.4 for more details). The performance of the graphene coating as a transparent, conductive and potentially passivating film on these metal foils was evaluated by heating the graphene-coated foils in an oven for 4 hours at 200 °C in air (which contains 21% oxygen by volume), as well as immersing 1 $cm^2$ pieces of such graphene-coated metal foils into a solution of 30% (w/w) hydrogen peroxide ($H_2O_2$, Fisher Scientific) up to 45 minutes.

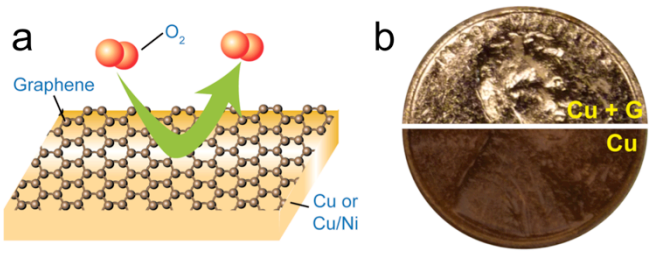


**Figure A.1: Graphene as an oxidation barrier. a,** Illustration depicting a graphene sheet as a chemically inert diffusion barrier. **b,** Photograph showing graphene coated (upper) and uncoated (lower) penny after $H_2O_2$ treatment (30%, 2 min).

In Figure A.1 and Figure A.2 we show optical images of various metal surfaces, both graphene-coated and uncoated, after air anneals and exposure to liquid etchant. In all cases the graphene-coated metal surfaces show very little visible change, as opposed to the uncoated metals whose surfaces change appearance dramatically. As schematically shown in Figure A.1a, the graphene film can be seen as a molecular diffusion barrier, preventing the reactive agent from ever reaching the metal underneath. To demonstrate the potential of graphene as a protection layer for bulk metals, we grew single layer graphene on a copper penny (95%Cu/5% Zn, minted 1962 - 1982). In Figure A.1b two pennies are displayed, both of which were exposed to 30% $H_2O_2$ for 2 minutes. Although both pennies originally looked the same, a stark contrast arises between the graphene-coated (upper) and uncoated (lower) coins after exposure. The unprotected copper penny turned a dark shade of brown, whereas the protected coin maintained the original appearance.

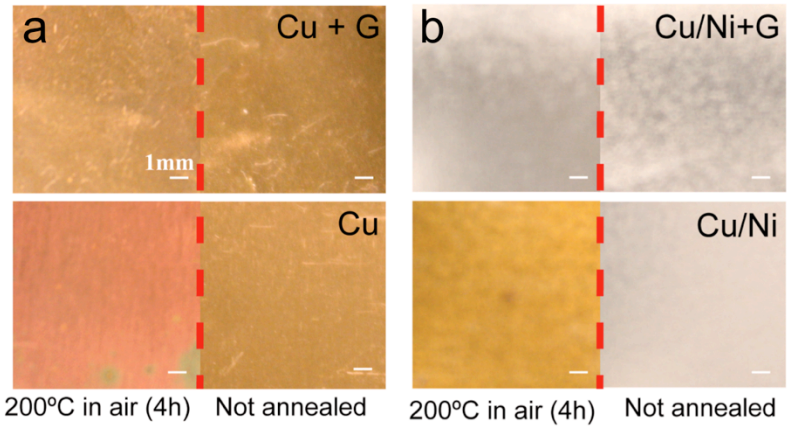


**Figure A.2: Oxidation protection on Cu and Cu/Ni foils.** Photographs of **a,** Cu and **b,** Cu/Ni foil with and without graphene coating taken before and after annealing in air (200 °C, 4h).

More specifically, graphene-coated Cu (Cu+G) and Cu/Ni (Cu/Ni+G ) foils show no changes after lengthy air anneals (200 ºC, 4 hours, see Figure A.2), whereas uncoated films exhibited a substantial darkening. All these examples show that graphene passivates the growth surface, which, as discussed earlier, is due to its impermeability and chemical resistance. Below we discuss these two aspects in more detail.

## A.4 Metal Surface Passivation

Figure A.3 shows scanning electron microscopy (SEM) and X-ray photoelectron spectroscopy (XPS) measurements of metal surfaces before and after air oxidation. The atomic steps under the graphene film are clearly visible for graphene coated samples before and after the anneals (Figure A.3a and Figure A.3c, top), indicating that copper oxide has not formed beneath the graphene. The coated Cu and Cu/Ni surface is free from surface oxide due to the hydrogen ($H_2$) gas exposure at a high temperature (1000 °C) prior to the growth of graphene. The metal surface is

protected by the graphene layer during subsequent extended exposure (4 hours) at 200 °C in air. The micrograph has a number of small bright white spots representing oxides formed, most likely at the graphene grain boundaries or defect sites of the graphene surface, as presented in a previous paper[18]. Better protection is afforded for the Cu/Ni alloy foil surface by a multilayer (as confirmed by the measured Raman ratio of the G/2D band shown in Figure A.4) graphene coating. In contrast, images of unprotected metal foils after annealing in air show a rough surface structure and are much more blurry – likely due to a charging effect from the presence of oxides. It is difficult to obtain a clear image because of the accumulated charges in insulating oxides on the surface.

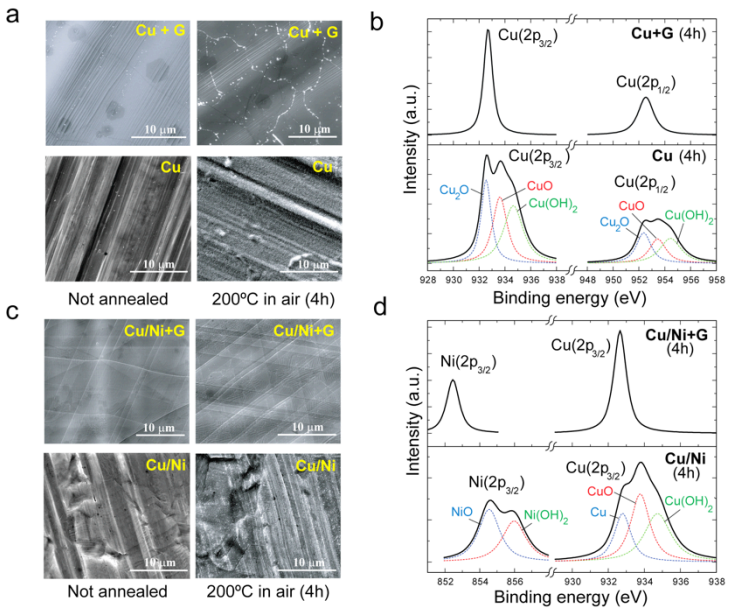


**Figure A.3: Effects of air oxidation on graphene coated metal surface. a,** SEM images of graphene coated (upper) and uncoated (lower) Cu foil taken before (left column) and after (right column) annealing in air. **b,** XPS core-level Cu2p spectrum of coated (upper) and uncoated (lower) Cu foil after air anneal (200 °C, 4h). **c,** SEM images of Graphene coated (upper) and uncoated (lower) Cu/Ni foil taken before (left column) and after (right column)

annealing in air. **d,** XPS core-level $Ni2p_{3/2}$ and $Cu2p_{3/2}$ spectrum of coated (upper) and uncoated (lower) Cu/Ni foil after air anneal (200 °C, 4h).

XPS was then performed on these substrates in order to provide an analysis of the metal composition after heat treatment. The XPS spectrum of coated Cu foil before and after air annealing both show two Cu peaks at binding energies of 932.6 and 952.5 eV, which correspond to $Cu2p_{3/2}$ and $Cu2p_{1/2}$ (Figure A.3b) [19,20]. However, uncoated Cu foil shows broader peaks which correspond to different copper oxides, $Cu_2O$ (932.5 and 952.3 eV), CuO (933.6 and 953.4 eV), and $Cu(OH)_2$ (934.7 and 954.5 eV)[19,20]. These data indicate that the graphene coating is clearly acting as a diffusion barrier, protecting the underlying copper from oxidation.

Similarly, Figure A.3d shows the XPS spectrum for the coated Cu/Ni foil. Two sharp peaks are present, corresponding to $Cu2p_{3/2}$ (932.6 eV) and $Ni2p_{3/2}$ (852.5 eV)[19], demonstrating no change in the chemical composition of the protected metal. As before, inspection of the uncoated foil reveals two broader peaks, one is comprised of two nickel oxide peaks, NiO (854.5 eV) and $Ni(OH)_2$ (856.0 eV) [19,21], and the other is comprised of three peaks - metallic Cu (932.6 eV) and two copper oxide peaks, CuO (933.6 eV), and $Cu(OH)_2$ (934.7 eV). These XPS spectra demonstrate that the uncoated Cu/Ni foil was oxidized to a certain extent after heat treatment. The data in Figure A.3d also provide a means to compare graphene as a protection layer with the Cu/Ni alloy inherent corrosion resistance. Upon oxidation the uncoated Cu/Ni alloy forms a protective film of $Cu_2O$ with Ni compounds (e.g., NiO) as minor components[22,23]. This oxide layer is more stable due to the presence of Ni atoms in the copper lattice, resulting in a lower number of defects[22,24]. The oxide therefore provides

better protection against further oxidation, which explains the presence of a metallic Cu signal in Figure A.3d (lower). Nevertheless, in our experiments the graphene-coated Cu/Ni alloy still shows significantly better oxidation resistance, compared to the uncoated Cu/Ni alloy, as can be seen from the absence of an oxide signals in Figure A.3d (upper).

## A.5 Chemical Stability of Graphene Under Reducing Conditions

Under air oxidation graphene also shows remarkable chemical stability. Figure A.4 presents the Raman spectra of coated and uncoated Cu and Cu/Ni foil samples, before and after heating in air. Before treatment, the coated Cu foil exhibits a small G/2D peak ratio ~ 0.5, which is indicative of high quality single layer graphene[25]. The coated Cu/Ni foil also exhibits characteristics of high quality multilayer graphene – a low D band in conjunction with the distinct G and 2D peak shapes. After heat treatment, the uncoated Cu foil shows multiple peaks between 214 $cm^{-1}$ and 800 $cm^{-1}$, corresponding to various copper oxides - $Cu_2O$ (214, 644 $cm^{-1}$), CuO (299, 500 $cm^{-1}$) and $Cu(OH)_2$ (800 $cm^{-1}$)[26,27]. Uncoated Cu/Ni foil displays CuO (299, 342, 634 $cm^{-1}$) and $Cu_2O$ (218 $cm^{-1}$) peaks, as well as NiO peaks (550 and 1100 $cm^{-1}$)[28,29]. In contrast, the initial and final spectra of the coated foils are essentially identical. This clearly shows that the graphene is not only protecting the underlying metal, but is also virtually unaltered by the oxidizing gas. The data shown in Figure A.3 and Figure A.4 illustrates that both single and multi-layer graphene serve as ideal protection coatings by both preventing diffusion and remaining chemically inert. Surprisingly, this oxidation protection by graphene is possible without strong adhesion to metal

surfaces. Theory indicates that the interaction between graphene and the underneath metal is rather weak[30–33]. The graphene on Cu is considered to be physisorbed with a binding energy of $\Delta E<0.07$ eV per carbon atom[30].

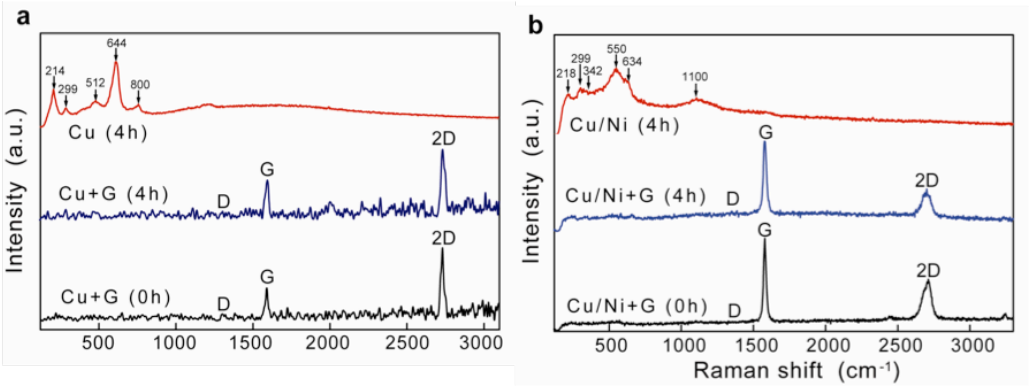


**Figure A.4: Chemical inertness of graphene.** Raman spectrum of the Cu (a) and Cu/Ni alloy (b) foils with and without a graphene coating, acquired following heating in air at 200 °C for 0 and 4 hours, respectively.

To test longer-term exposure, a run with 2 days exposure to air at 200 $^{o}$C was performed on the graphene-coated Cu and Cu/Ni alloy samples. The Cu foils coated with monolayer graphene were oxidized to some extent, but a multilayer graphene-coated Cu/Ni foil remains visibly ‘shiny’. The Raman spectrum obtained within graphene grains is identical to the 4 hour anneal, with sharp G and 2D Raman bands. However, regions of oxidized metal surface were formed along the grain boundaries of the graphene can seen by SEM, suggesting that the grain boundary is more susceptible to oxidative reactions.

## A.6 Effects of Graphene Grain Boundaries on Impermeability

Short time exposure to the oxidizing aqueous solutions $H_2O_2$ showed also significant protection for both graphene-coated Cu and Cu/Ni alloy foils. Graphene coated Cu and Cu/Ni samples were only attacked in few spots (white regions) after 15 and 5 minutes of $H_2O_2$ exposure respectively (Figure A.5). Once the metal is exposed, the liquid can easily penetrate underneath the graphene sheet to attack the pristine metal, since there is no oxide layer to slow the corrosion. Examples of this are seen in both the Cu and the Cu/Ni samples after longer $H_2O_2$ exposure, 45 and 15 minutes, respectively. The slower etch rate of graphene coated Cu than Cu/Ni might be due to the less reactive property of Cu than Ni in $H_2O_2$. The majority of the metal surface remains covered and protected by graphene.

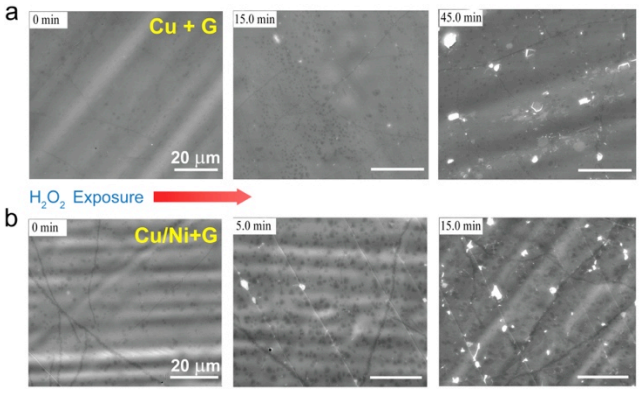


**Figure A.5: Effects of liquid oxidation on graphene coated metal surfaces. a,** SEM images of graphene coated Cu film after 30% $H_2O_2$ exposure for 0 min, 15 min and 45 min, respectively. **b,** SEM images of graphene coated Cu/Ni alloy after 30% $H_2O_2$ exposure for 0 min, 5 min and 15 min, respectively.

In order to study the impact of defects and grain boundaries present in CVD graphene sheets, 2D micro-Raman spectroscopy was used on a graphene-coated Cu

thin film. As noted above, an important aspect of graphene protection is its chemical inertness. Nevertheless, it is known that graphene is more likely to react at edges or where defects are present[34]. In Figure A.6, we show a series of 2D Raman maps taken on a graphene coated Cu thin film before and after $H_2O_2$ exposure. In particular we show spatial Raman mappings of signals for Cu oxide (490 – 652 $cm^{-1}$) and graphene D band (1300 – 1330 $cm^{-1}$), all normalized with respect to the G band signal. We make two notable observations in these 2D Raman images. First, even before the $H_2O_2$ exposure, there exist areas of high oxide signal, which also show larger D bands (black arrow). This is most likely due to the presence of some residual copper oxide before the growth that resulted in graphene of poor quality. Second, while most graphene areas show no changes before and after the exposure (white arrow), there are areas that display a clear change. In these areas (red arrow), we observe a large increase in D/G ratio, which is accompanied by the appearance of copper oxide peaks. This suggests that in the majority of areas the graphene is of higher quality and is able to protect the metal completely. In other areas, however, graphene does not act as a perfect diffusion barrier, and allows some of the etchant to penetrate through the graphene layer and oxidize the metal. This overall increase in the presence of surface oxides, which are hydrophilic, is further supported by the water contact angle measurements presented in Figure A.6b. Before $H_2O_2$ exposure, the graphene-coated Cu film exhibits a contact angle of 83º, comparable to values obtained for HOPG[35]. After peroxide treatment, however, the contact angle is reduced by over 10%, indicating the presence of a more hydrophilic film. Since this contact angle is much closer to that of HOPG than to the contact angle for pure copper oxide film[36], our

results further suggest that the hydrophobic graphene sheet is still protecting the majority of the underlying metal.

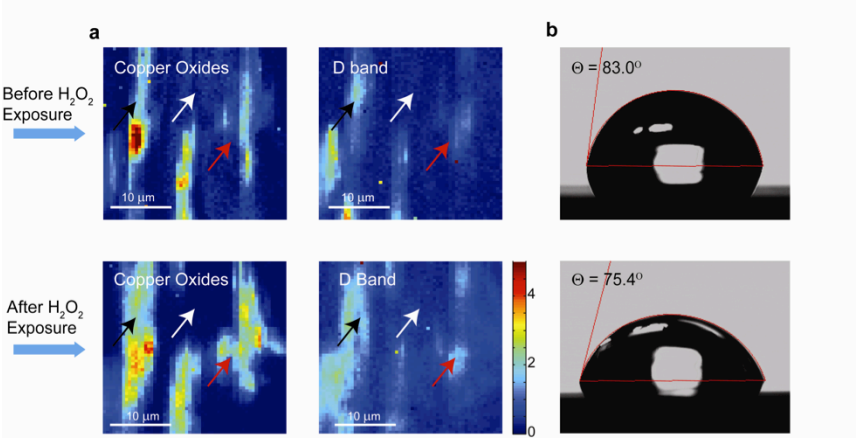


**Figure A.6: Oxidation effects of the graphene surface. a,** Two-dimensional micro-Raman maps of graphene coated Cu film (500 nm thick) before (upper row) and after (lower row) $H_2O_2$ treatment (30%, 2 min), measured for the same location. Left column indicates Cu oxide/G (490 – 652 $cm^{-1}$) while right column portrays D/G (1300 – 1330 $cm^{-1}$) ratio. Black arrows indicate pre-existing oxidized areas before $H_2O_2$ exposure while white and red arrows show well protected areas and poorly protected areas after $H_2O_2$ exposure, respectively. **b,** Contact angle measurements of water on graphene coated Cu films before (upper) and after (lower) $H_2O_2$ treatment.

Diffusion at metal grain boundaries is a significant factor in accelerating corrosion. In Figure A.7a we follow the etching of a thin copper film in 0.2M $HNO_3$. On both coated and uncoated films etch originates along the metal grain boundaries. For coated films, however, although the channels are etched all the way down to expose the silicon oxide, the top of the channel can remain bridged by a graphene sheet (see Figure A.7b). The proposed mechanism for this process is depicted in Figure A.7c.

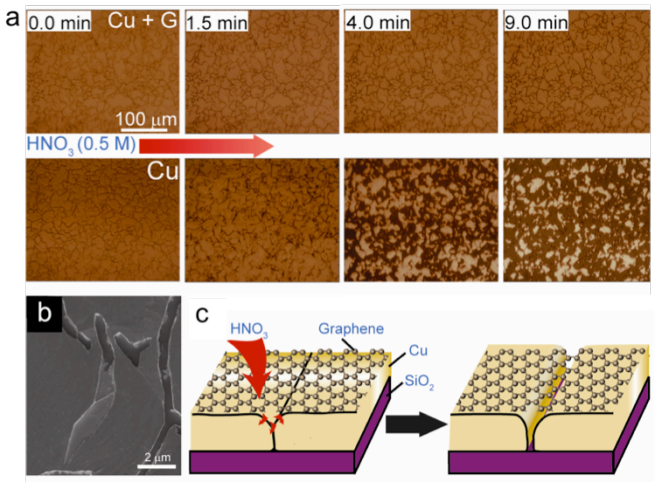


**Figure A.7: Diffusion at metal grain boundaries. a,** Time series optical images of graphene coated (upper row) and uncoated (lower) Cu films under a strong etchant ($HNO_3$, 0.2 M), showing 10× slower etching in the graphene coated Cu film. **b,** SEM image showing an etched Cu grain boundary partly covered by graphene. **c,** Schematic depicting the proposed mechanism of mass transport through defects/voids in graphene, leading to the corrosion of the underlying copper film, which is faster along Cu grain boundaries.

While high-quality graphene does act as a perfect diffusion barrier, graphene with many defects only limits it – eventually allowing the etchant to diffuse through, etch the metal, and diffuse the products out. According to the AFM images, the proposed mechanism is that in which the graphene sheet is ruptured in weak spots, allowing the etchant to flow freely through those small holes. Despite these effects, the protected copper film is etched about ten times more slowly.

In principle, "perfect" graphene – without defects and grain boundaries – is able to preserve the surface of metal under reactive environments over a long period of time thanks to its impermeability and chemical inertness. However, real CVD graphene is expected to show non-ideal behaviors. It is known that graphene is more likely to react at edges or where defects are present such as wrinkles, point defect as well as graphene boundaries[34]. Our results suggest that grain boundaries are likely to

be the main contributor to oxidation of the underlying metals. One way to solve this problem is to grow high quality graphene films with better mechanical integrity. Another way is to extend study to ultrathin graphite or hexagonal boron nitride thin films. The protection technique discussed here should be effective on any metals that can catalyze graphene or ultrathin graphite growth, e.g., Cu, Ni, Fe, Ta, Pt, Ir, Ru and their alloys. Furthermore, refinement of graphene (multilayer graphene, ultrathin graphite) transfer techniques may allow their broader use on arbitrary substrates. This approach may solve the problem of the pristine metal surface under graphene is highly prone to oxidation after an initial breach[37].

This discovery would lead the world-wide graphene synthesis community to implement these novel applications of graphene, multilayer graphene, and ultrathin graphite as passivation coatings. The main limitation of this protection technique is its deactivation after mechanical damages. Therefore we would suggest using this protective coating on applications that do not involve circumstances where abrasion would ever be present, such as replacement of the Au coating for passivating Cu lines in semiconductor chip technology.

## A.7 Conclusion

In this chapter we demonstrate the excellent performance of CVD graphene as a passivation layer for Cu and Cu/Ni films. The ability of graphene coating to both prevent diffusion, as well as its chemical inertness to oxidizing gas and liquid solutions allow for its use in a wide variety of environments. Although partial oxidation may occur at graphene grain boundaries, we note that the graphene sheets

provide near perfect protection within grains. With further advances in graphene growth and careful control of the metal catalyst, we anticipate a significant improvement in the level of protection these films may provide. Furthermore, refinement of graphene transfer techniques may even make it possible to take advantage of this material's amazing properties in any compatible system.

REFERENCES


1. Novoselov, K. S. *et al.* A roadmap for graphene. *Nature* **490,** 192–200 (2012).

2. M. S. Dresselhaus, G. Dresselhaus, P. C. E. *Science of Fullerenes and Carbon Nanotubes*. (1996).

3. Holt, J. K. *et al.* Fast mass transport through sub-2-nanometer carbon nanotubes. *Science* **312,** 1034–7 (2006).

4. Bunch, J. S. *et al.* Impermeable atomic membranes from graphene sheets. *Nano Lett.* **8,** 2458–62 (2008).

5. De Heer, W. A. *et al.* Epitaxial graphene. *Solid State Commun.* **143,** 92–100 (2007).

6. Hass, J. *et al.* Why Multilayer Graphene on 4H-SiC(0001¯) Behaves Like a Single Sheet of Graphene. *Phys. Rev. Lett.* **100,** 125504 (2008).

7. Shivaraman, S., Chandrashekhar, M. V. S., Boeckl, J. J. & Spencer, M. G. Thickness Estimation of Epitaxial Graphene on SiC Using Attenuation of Substrate Raman Intensity. *J. Electron. Mater.* **38,** 725–730 (2009).

8. Gray, J. E. & Luan, B. Protective coatings on magnesium and its alloys — a critical review. *J. Alloys Compd.* **336,** 88–113 (2002).

9. Appa Rao, B. V., Yakub Iqbal, M. & Sreedhar, B. Self-assembled monolayer of 2-(octadecylthio)benzothiazole for corrosion protection of copper. *Corros. Sci.* **51,** 1441–1452 (2009).

10. Stratmann, M., Feser, R. & Leng, A. Corrosion protection by organic films. *Electrochim. Acta* **39,** 1207–1214 (1994).

11. Merkula, Y. I. Utilization of Edn Varnish for Protection of Metal Sea-Water Sampling Bottles Against Corrosion. *Oceanology-Ussr* **14,** 299–300 (1974).

12. Redondo, M. I. & Breslin, C. B. Polypyrrole electrodeposited on copper from an aqueous phosphate solution: Corrosion protection properties. *Corros. Sci.* **49,** 1765–1776 (2007).

13. Mittal, V. K. *et al.* Formation and characterization of bi-layer oxide coating on carbon-steel for improving corrosion resistance. *Thin Solid Films* **517,** 1672–1676 (2009).

14. Kinlen, P. J. A Mechanistic Investigation of Polyaniline Corrosion Protection Using the Scanning Reference Electrode Technique. *J. Electrochem. Soc.* **146,** 3690 (1999).

15. Grundmeier, G., Reinartz, C., Rohwerder, M. & Stratmann, M. Corrosion properties of chemically modified metal surfaces. *Electrochim. Acta* **43,** 165–174 (1998).

16. Segarra, M. *et al.* Copper and CuNi Alloys Substrates for HTS Coated Conductor Applications Protected from Oxidation. *Mater. Sci. Forum* **426-432,** 3511–3516 (2003).

17. Li, X. *et al.* Large-area synthesis of high-quality and uniform graphene films on copper foils. *Science* **324,** 1312–4 (2009).

18. Li, X. *et al.* Synthesis, Characterization, and Properties of Large-Area Graphene Films. in *ECS Transactions* **19,** 41–52 (ECS, 2009).

19. Dubé, C. E. Electrodeposition of Metal Alloy and Mixed Oxide Films Using a Single-Precursor Tetranuclear Copper-Nickel Complex. *J. Electrochem. Soc.* **142,** 3357 (1995).

20. Poulston, S., Parlett, P. M., Stone, P. & Bowker, M. Surface Oxidation and Reduction of CuO and Cu2O Studied Using XPS and XAES. *Surf. Interface Anal.* **24,** 811–820 (1996).

21. Sasi, B. & Gopchandran, K. G. Nanostructured mesoporous nickel oxide thin films. *Nanotechnology* **18,** 115613 (2007).

22. Yuan, S. J. & Pehkonen, S. O. Surface characterization and corrosion behavior of 70/30 Cu–Ni alloy in pristine and sulfide-containing simulated seawater. *Corros. Sci.* **49,** 1276–1304 (2007).

23. Kato, C., Castle, J. E., Ateya, B. G., Pickering, H. W. On the Mechanism of Corrosion of Cu-9.4Ni-1.7Fe Alloy in Air Saturated Aqueous NaCl Solution. *J. Electrochem. Soc.* **127,** 1890 (1980).

24. Druska, P., Strehblow, H.-H. & Golledge, S. A surface analytical examination of passive layers on alloys: Part I. Alkaline solution. *Corros. Sci.* **38,** 835–851 (1996).

25. Ferrari, A. C. *et al.* Raman Spectrum of Graphene and Graphene Layers. *Phys. Rev. Lett.* **97,** 187401 (2006).

26. Niaura, G. Surface-enhanced Raman spectroscopic observation of two kinds of adsorbed OH− ions at copper electrode. *Electrochim. Acta* **45,** 3507–3519 (2000).

27. Chou, M. H., Liu, S. B., Huang, C. Y., Wu, S. Y. & Cheng, C.-L. Confocal Raman spectroscopic mapping studies on a single CuO nanowire. *Appl. Surf. Sci.* **254,** 7539–7543 (2008).

28. Ishida, Y., Mita, Y., Kobayashi, M. & Endo, S. Pressure effects on transition metal monoxide NiO. *Phys. status solidi* **235,** 501–504 (2003).

29. Mendoza, L., Baddour-Hadjean, R., Cassir, M. & Pereira-Ramos, J. P. Raman evidence of the formation of LT-LiCoO2 thin layers on NiO in molten carbonate at 650°C. *Appl. Surf. Sci.* **225,** 356–361 (2004).

30. Giovannetti, G. *et al.* Doping Graphene with Metal Contacts. *Phys. Rev. Lett.* **101,** 026803 (2008).

31. Qi, Y., Hector, L. G., Ooi, N. & Adams, J. B. A first principles study of adhesion and adhesive transfer at Al(111)/graphite(0001). *Surf. Sci.* **581,** 155–168 (2005).

32. Gamo, Y., Nagashima, A., Wakabayashi, M., Terai, M. & Oshima, C. Atomic structure of monolayer graphite formed on Ni(111). *Surf. Sci.* **374,** 61–64 (1997).

33. Bertoni, G., Calmels, L., Altibelli, A. & Serin, V. First-principles calculation of the electronic structure and EELS spectra at the graphene/Ni(111) interface. *Phys. Rev. B* **71,** 075402 (2005).

34. Jiang, D., Sumpter, B. G. & Dai, S. Unique chemical reactivity of a graphene nanoribbon's zigzag edge. *J. Chem. Phys.* **126,** 134701 (2007).

35. Yan, A., Xiao, X., Külaots, I., Sheldon, B. W. & Hurt, R. H. Controlling water contact angle on carbon surfaces from 5° to 167°. *Carbon N. Y.* **44,** 3116–3120 (2006).

36. Chang, F.-M., Cheng, S.-L., Hong, S.-J., Sheng, Y.-J. & Tsao, H.-K. Superhydrophilicity to superhydrophobicity transition of CuO nanowire films. *Appl. Phys. Lett.* **96,** 114101 (2010).

37. Schriver, M. *et al.* Graphene as a Long-Term Metal Oxidation Barrier: Worse Than Nothing. *ACS Nano* **7,** 5763–5768 (2013).

# APPENDIX B

# LATERAL GRAPHENE/GRAPHENE AND GRAPHENE *h*-BN HETEROSTRUCTURES

## B.1 Introduction

Precise spatial control over the electrical properties of thin films is the key capability enabling the production of modern integrated circuitry. While this ability is well established for bulk and thin film technologies, controlled fabrication of lateral heterostructures in truly atomically thin systems has not been achieved. Such control would enable the fabrication of electrically isolated active and passive elements embedded in continuous, one atom thick sheets, which could be manipulated and stacked to form complex devices at the ultimate thickness limit. Here we report a versatile and scalable process, "patterned regrowth," that allows for the spatially controlled synthesis of lateral junctions between electrically conductive graphene and insulating hexagonal boron nitride (*h*-BN), as well as between intrinsic and substitutionally doped graphene. We demonstrate that our resulting films are physically and electrically unchanged from the processing and form a mechanically continuous sheet, as confirmed by dark field transmission electron microscopy (TEM), atomic force microscopy (AFM), and Raman spectroscopy. This work is presented here is in part a useful demonstration of the bilayer graphene imaging technique presented in Chapter 4. The dark-field TEM imaging technique proved to be key in deciphering the boundary structure between the two consecutive graphene growths, as it can significantly enhance the appearance of the small bilayer domains present in the

inter-growth boundary. Further experiments were done to probe the electronic properties of these heterostructures. Conductance measurements confirm laterally insulating behavior for *h*-BN regions, while the electrical behavior of both doped and undoped graphene sheets maintain excellent and uniform properties, with low sheet resistances and high carrier mobilities of more than 10,000 $cm^2/V{\cdot}s$. Our results represent an important step towards developing atomically thin integrated circuitry. This section is based on work done in collaboration with my colleagues M. P. Levendorf and C.-J. Kim, and published in M. P. Levendorf, C.-J. Kim, L. Brown, *et al.*, ***Nature***, 488, 627–632 (2012).

## B.2 Growing Graphene and *h*-BN heterostructures

Integration of 2D materials into modern electronics has garnered considerable interest since few layer sheets of graphene were first obtained in 2004[1–4] In order to achieve this goal, precise spatial control over the electronic properties of thin film is essential. Such control would enable the fabrication of electrically isolated active and passive elements embedded in continuous, one atom thick sheets, which could be manipulated and stacked to form complex devices at the ultimate thickness limit. Recent advancements in CVD methods provide two capabilities essential towards this goal. First, they allow for the large scale production of both intrinsic and doped graphene[5–7], as well as *h*-BN[8–10]. Second, it is shown that areas of different atomic compositions may coexist within continuous atomically thin films; Ci *et al.* reported the synthesis of *h*-BN/graphene systems (*h*-BNC), where BN regions are uniformly distributed in graphene sheets[10], and Zhao *et al.* showed dopant atoms may be incorporated directly

into the graphene lattice during synthesis[6]. One exciting potential of these multi-component system is the presence of heterojunctions, naturally forming between different neighboring regions. Graphene/*h*-BN interfaces are of particular interest as, with proper control, the bandgap and magnetic properties can be precisely engineered[11–13]. These previous works, however, have focused on the synthesis of these sheets and have not provided ways to spatially control their atomic compositions and electrical properties. Meanwhile, previously reported approaches for such a capability have fundamental limitations and cannot be easily integrated with conventional lithography. For instance, surface adsorbates[14] and multiple local gates[15] have been used to spatially control the doping level in graphene, both of which fail to take advantage of the 2-dimensionality of the film. Other techniques used in modern thin film technology, such as ion implantation, have limited use in 2D materials, where they can cause damage to the crystal lattice[16].

In this section we present a new method of "*patterned regrowth"* that allows for multiple graphene/*h*-BN syntheses on a single catalytic surface, where regions with distinct electrical properties can be patterned to form an atomically-thin continuous film. The method is versatile and can be integrated with conventional device fabrication, as it is performed directly on the copper substrate and employs standard photolithographic techniques.


**Figure B.1: Process schematic of graphene heterostructures. a,** Schematic for formation of atomically thin lateral heterojunctions. Graphene ($G^1$, superscript representing growth order) is grown on copper and then patterned using photolithography and a reactive ion etch. A second layer of either graphene or *h*-BN is then grown ($G^2$ or *h*-$BN^2$) on the patterned Cu/$G^1$. The final film is then transferred to the target substrate. **b,** Left: optical image of a patterned Cu/ $G^1$ foil oxidized in order to enhance contrast between the $G^1$ (bright areas) and Cu (dark areas) surfaces. Right: optical image after growth of intrinsic-$G^2$ (*i*-$G^2$).

Figure B.1a summarizes our approach for the patterned regrowth and characterization. After growing the first film of graphene ($G^1$, superscript representing the growth order) we then deposit a protective layer of photoresist and pattern away unwanted areas. The key point here is the use of an extremely clean etching chamber to remove the thin graphene layer in the unwanted area. Next we grow a second layer of graphene or *h*-BN ($G^2$/*h*-$BN^2$) and transfer the hybrid film onto the desired substrate for further characterization. All of our growths are performed on Cu foil using standard literature recipes for both graphene and *h*-BN growths[5,6,8]. Introducing dopant gases during any graphene growth stage allows us to produce both intrinsic graphene (*i*-G; $H_2$ + $CH_4$) and *n*-type graphene (*n*-G; $NH_3$ + $H_2$ + $CH_4$) in a single process run. Figure B.1b shows optical images of the Cu growth substrate at different steps of the process. After patterning the first graphene layer, the substrate was heated to 135°C in air in order to enhance the contrast, as is shown in Figure B.1b (left); the areas of Cu protected by *i*-$G^1$ remain unoxidized whereas the unprotected areas do not[17]. Figure B.1b (right) shows the same foil after synthesis of the second graphene, and demonstrates the homogeneity of the Cu/graphene substrate. Prior to further

characterization, the presence of graphene is confirmed using micro Raman spectroscopy.

### B.3 The Crystalline Structure of Graphene/Graphene Lateral Junction

The fidelity of the transferred pattern and the quality of the junctions formed by our method were studied using DF-TEM[19–21], where use of a specific objective aperture filter allows imaging of areas with corresponding lattice orientations. As detailed in chapter 2, multiple such images are then colored and overlaid to form a complete map of the film. This technique can therefore resolve the grain structure and number of layers with nanometer scale resolution, thus allowing direct structural imaging of the resulting films near and away from the junction area. Figure B.2a shows a composite image of a graphene sample that includes both the first and second grown areas as well as the junction between the two, where each color represents a particular relative grain orientation. For this, growths of $i$-$G^1$/$i$-$G^2$ were transferred onto 10nm thick $Si_3N_4$ TEM membranes. Both $G^1$ and $G^2$ regions (see Figure B.2a inset) are comprised of single crystals of similar sizes, which indicates that the polycrystalline structure of the graphene is mainly determined by the synthesis conditions rather than the growth order, and also that the structure of the first grown graphene is unaffected by our patterned regrowth. The grain structure near the junction area further suggests high quality, continuous growth of graphene between $G^1$ and $G^2$ areas (Figure B.2b). It shows that the crystallinity is maintained uniformly across this region without amorphous carbon or voids even at the nanometer scale. Significantly,

the location of the junction closely follows the designed pattern within the resolution of our instrument (Figure B.2a, partially outlined).

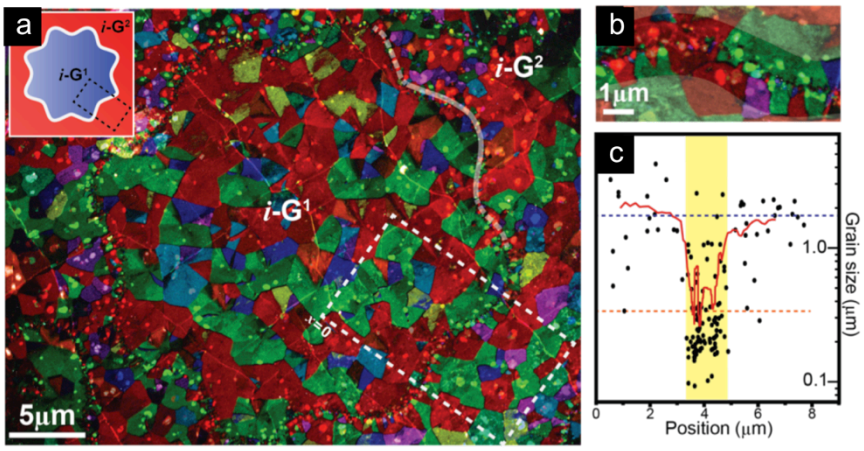


**Figure B.2: DF-TEM characterization of graphene heterostructures. a,** False color darkfield TEM image of an *i*-$G^1$/*i*-$G^2$ patterned area (schematic in inset). Colors correspond to relative grain rotation. The pattern (partially outlined) is maintained throughout the processing **b,** Zoomed-in image of the junction region. **c,** Plot of grain size vs position in the box outlined in (c) Standard growth areas show a mean grain size of ~1.7µm (blue), which are joined by a region of smaller grains (mean ~ 0.33µm, orange). A moving average (red line) suggests the width of the junction region (highlighted) is ~2µm. Adapted from [18].

We note that different growth behavior occurs at the junction. In Figure B.2c, we plot grain size as a function of position within the box indicated in Figure B.2a. While both $G^1$ and $G^2$ regions show average grain sizes of ~1.7µm, near the junction they are much smaller (mean ~0.33µm). The moving average (Figure B.2c, red line) shows that the width of this area with smaller grains is approximately 2µm, comparable to the average $G^1$ and $G^2$ grain size. This, in addition to the increased density of small bilayer areas in the junction (bright spots), suggests that the junction between $G^1$ and $G^2$ is formed by graphene nucleated and grown in the junction area rather than by direct stitching between grains nucleated away from it. This suggests

edge nucleated growth, which is similar to a "seeding" effect reported previously[22–24]. A highly reactive environment is thus required in order to promote uniform stitching (see Figure B.4). We observe that regrowth under conditions that provide slower growth do not produce well-connected junctions in both graphene/graphene and graphene/*h*-BN films, which is consistent with this explanation.

## B.4 Graphene/*h*-BN Lateral Junctions

The stitching technique described above is also applicable to the formation of insulator-metal lateral junctions using graphene and *h*-BN (Figure B.3), which we now discuss. In order to grow *h*-BN, we use ammonia-borane as a precursor, as reported previously[9], and carefully adjust growth parameters in order to control the average grain sizes and intergrain connectivity. Figure B.3a shows a false color DF-TEM image of a single layer *h*-BN sheet – as confirmed by Raman spectroscopy and X-ray photoelectron spectroscopy (XPS) – with relatively large domains in excess of 1 μm. Electron diffraction also shows that the film consists of single crystals with hexagonal lattice structures (Figure B.3a, inset). This *h*-BN growth, however, yields films with incomplete intergrain stitching, as indicated by the dark lines in Figure B.3a. Instead, *h*-BN grown under more reactive conditions (higher precursor flow rate) results in a continuous sheet, while exhibiting all the known characteristics of *h*-BN sheets.

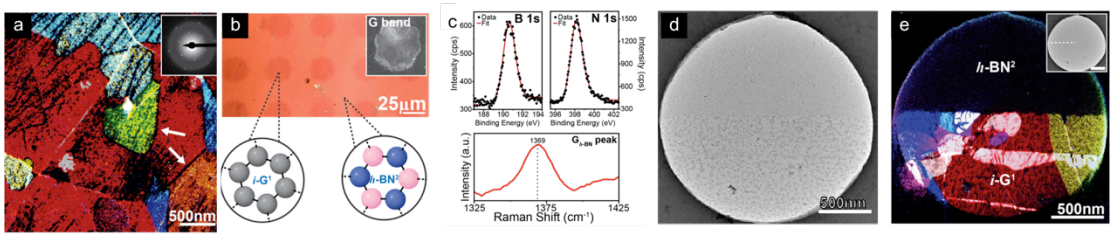


**Figure B.3: *h*-BN/graphene heterostructure synthesis and characterization. a,** False color DF-TEM image of an *h*-BN sheet grown in an environment of low reactivity with domains >1μm. **b,** Optical image of an *i*-$G^1$/*h*-$BN^2$ sheet transferred onto a $Si/SiO_2$ substrate. Inset: integrated intensity of Raman graphene G band showing a stark contrast between the regions. **c,** X-ray photoelectron spectroscopy data (upper) for an *h*-BN sheet grown in a more reactive environment, showing a 1:1.08 B:N atomic ratio. Raman spectroscopy (lower) confirms the presence of the *h*-BN G peak. **d,** Bright field TEM and **e,** False color DF-TEM image of a suspended *i*-$G^1$/*h*-$BN^2$ sheet with the junction region visible. The junction is well defined with no holes or tears observed, as shown by the brightfield TEM image in (d).

In Figure B.3b we show an optical image of a well-stitched *i*-$G^1$/*h*-$BN^2$ hybrid sheet transferred onto $Si/SiO_2$. The darker regions indicate areas of *i*-$G^1$ (stronger absorption) whereas the lighter regions are comprised of *h*-$BN^2$. The presence of *h*-BN is confirmed by the XPS data in Figure B.3c (upper; B and N in a 1:1.08 atomic ratio) and Raman spectroscopy (lower; *h*-BN G peak).

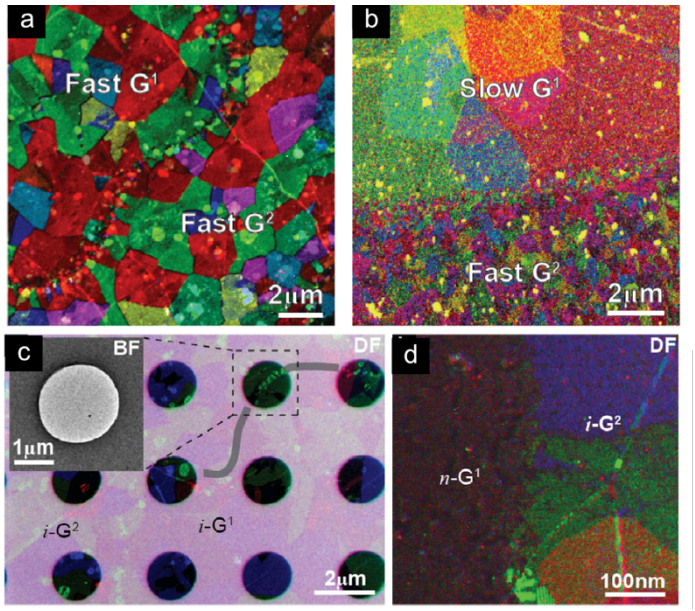


**Figure B.4: Well stitched junctions with a second 'fast' growth.** DF-TEM images the junction area in **a,** small grain and **b,** large grain graphene as first growths, followed by a small grain 'fast' growth **c,** DF-TEM image of suspended graphene/graphene membranes, displaying their mechanical integrity. Inset: brightfield image of the junction area. **d,** DF-TEM image of a junction between intrinsic and doped graphene. Adapted from [18].

## B.5 Electronic Properties of Graphene/Graphene and Graphene/h-BN Structures

This, as well as the 2-dimensional Raman image (Figure B.3b, inset) of the graphene G band intensity, confirms the successful pattern transfer to the *i*-$G^1$/*h*-$BN^2$ hybrid sheet. The brightfield image (Figure B.3d) shows a mechanically continuous sheet that is cleanly suspended with no breaks or tears at the junction region, confirming the stability and integrity of these growths. Furthermore, DF-TEM of suspended films confirms a sharp junction, as is shown in Figure B.3e, where the grains of the *i*-$G^1$ growth (lower, colored) end abruptly at the interface with the *h*-$BN^2$ (upper). We have observed similar mechanical continuity for both *i*-$G^1$/*i*-$G^2$ and *n*-$G^1$/-

*i*-G[2] growths (Figure B.4). Successful synthesis of these hybrid films allows us to fabricate electrically isolated graphene devices in a single, atomically flat sheet, and to create pre-patterned, multilayer devices, as is further demonstrated in Figure B.5 and in further detail in ref [18].

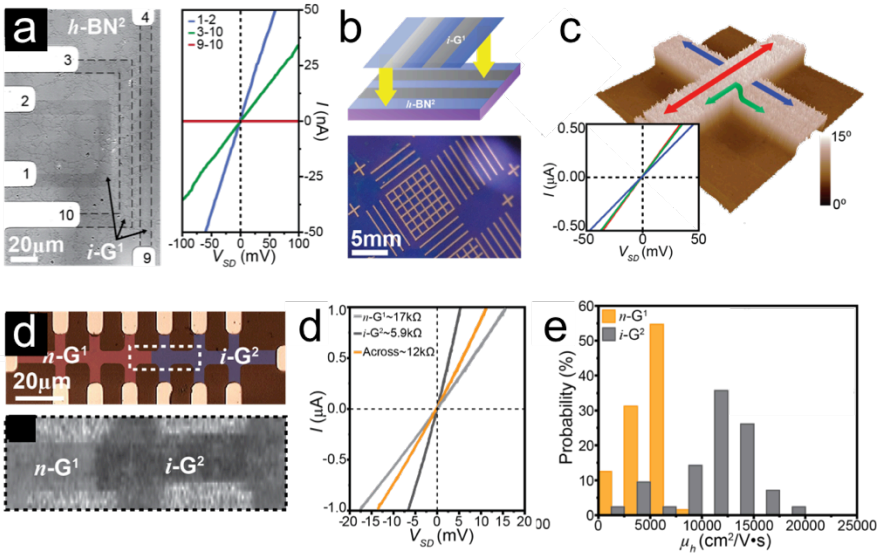


**Figure B.5: Electrical characterization of doped graphene and graphene/h-BN junctions, and their layered devices. a**, Optical image of an G/*h*-BN sheet with electrodes contacting graphene strips. Right: *I-V* characteristics of indicated devices, with graphene showing conducting behavior and *h*-BN exhibiting insulating characteristics ($R_{sheet}$ >400TΩ). **b,** Schematic of a multiple transfer process (top), resulting in an array of layered devices (bottom). **c,** Electrostatic force microscopy (EFM) phase image of a G[1]-G[1] cross junction. *I-V* characteristics (lower) show no additional contact resistance. **d,** Optical image (top) with false color overlay and Raman map (bottom) of a doped graphene heterojunction device. **e,** Four terminal *I-V* characteristics of the three regions, confirming electrical continuity. The junction adds almost no additional resistance ($\Delta R_{sheet}$ ~ 0.03 kΩ). **e,** Probability distribution of mobility $\mu_h$ for *n*-G[1] (orange) and *i*-G[2] (grey) regions, displaying high mobility values. Adapted from [18].

We propose that our patterned regrowth technique provides a versatile and scalable method for growing and integrating layered materials, beyond *h*-BN and graphene, for atomically thin circuitry. In particular, the addition of two-dimensional semiconducting materials, such as $MoS_2$[25], would bring together the three key building

blocks (insulator, metal, and semiconductor) of modern integrated circuitry into a single, transferrable film. Furthermore, the devices made using this approach are likely to remain mechanically flexible and optically transparent, allowing transfer to arbitrary substrates for flexible, transparent electronics.

## B.6 Conclusion

In this chapter, we propose a "patterned regrowth" method directly patterning electrical circuitry, using *h*-BN and graphene, into atomically thin films using patterned regrowth. Multiple iterations of such steps would allow the formation of more complex circuits connected by lateral heterojunctions, while multiple transfers of these films would produce vertical heterojunctions and interconnects for increased functionality. We propose that our patterned regrowth technique provides a versatile and scalable method for growing and integrating layered materials, beyond *h*-BN and graphene, for atomically thin circuitry. In particular, the addition of two-dimensional semiconducting materials, such as $MoS_2$, would bring together the three key building blocks (insulator, metal, and semiconductor) of modern integrated circuitry into a single, transferrable film. Furthermore, the devices made using this approach are likely to remain mechanically flexible and optically transparent, allowing transfer to arbitrary substrates for flexible, transparent electronics.

# REFERENCES


1. Novoselov, K. S. *et al.* Electric field effect in atomically thin carbon films. *Science* **306,** 666–9 (2004).

2. Novoselov, K. S. *et al.* Two-dimensional gas of massless Dirac fermions in graphene. *Nature* **438,** 197–200 (2005).

3. Zhang, Y., Tan, Y.-W., Stormer, H. L. & Kim, P. Experimental observation of the quantum Hall effect and Berry's phase in graphene. *Nature* **438,** 201–4 (2005).

4. Kubota, Y., Watanabe, K., Tsuda, O. & Taniguchi, T. Deep ultraviolet light-emitting hexagonal boron nitride synthesized at atmospheric pressure. *Science* **317,** 932–4 (2007).

5. Li, X. *et al.* Large-area synthesis of high-quality and uniform graphene films on copper foils. *Science* **324,** 1312–4 (2009).

6. Zhao, L. *et al.* Visualizing individual nitrogen dopants in monolayer graphene. *Science* **333,** 999–1003 (2011).

7. Jin, Z., Yao, J., Kittrell, C. & Tour, J. M. Large-scale growth and characterizations of nitrogen-doped monolayer graphene sheets. *ACS Nano* **5,** 4112–7 (2011).

8. Kim, K. K. *et al.* Synthesis of monolayer hexagonal boron nitride on Cu foil using chemical vapor deposition. *Nano Lett.* **12,** 161–6 (2012).

9. Song, L. *et al.* Large scale growth and characterization of atomic hexagonal boron nitride layers. *Nano Lett.* **10,** 3209–15 (2010).

10. Ci, L. *et al.* Atomic layers of hybridized boron nitride and graphene domains. *Nat. Mater.* **9,** 430–5 (2010).

11. Liu, Y., Bhowmick, S. & Yakobson, B. I. BN white graphene with 'colorful' edges: the energies and morphology. *Nano Lett.* **11,** 3113–6 (2011).

12. Pruneda, J. M. Origin of half-semimetallicity induced at interfaces of C-BN heterostructures. *Phys. Rev. B* **81,** 161409 (2010).

13. Miyamoto, Y., Rubio, A., Cohen, M. L. & Louie, S. G. Chiral tubules of hexagonal BC 2 N. *Phys. Rev. B* **50,** 4976–4979 (1994).

14. Wehling, T. O. *et al.* Molecular doping of graphene. *Nano Lett.* **8,** 173–7 (2008).

15. Williams, J. R., Dicarlo, L. & Marcus, C. M. Quantum Hall effect in a gate-controlled p-n junction of graphene. *Science* **317,** 638–41 (2007).

16. Dresselhaus, M. S., Jorio, A., Hofmann, M., Dresselhaus, G. & Saito, R. Perspectives on carbon nanotubes and graphene Raman spectroscopy. *Nano Lett.* **10,** 751–8 (2010).

17. Chen, S. *et al.* Oxidation resistance of graphene-coated Cu and Cu/Ni alloy. *ACS Nano* **5,** 1321–7 (2011).

18. Levendorf, M. P. *et al.* Graphene and boron nitride lateral heterostructures for atomically thin circuitry. *Nature* **488,** 627–32 (2012).

19. Huang, P. Y. *et al.* Grains and grain boundaries in single-layer graphene atomic patchwork quilts. *Nature* **469,** 389–92 (2011).

20. Kim, K. *et al.* Grain boundary mapping in polycrystalline graphene. *ACS Nano* **5,** 2142–6 (2011).

21. Brown, L. *et al.* Twinning and twisting of tri- and bilayer graphene. *Nano Lett.* **12,** 1609–15 (2012).

22. Yu, Q. *et al.* Control and characterization of individual grains and grain boundaries in graphene grown by chemical vapour deposition. *Nat. Mater.* **10,** 443–9 (2011).

23. Yan, Z. *et al.* Growth of bilayer graphene on insulating substrates. *ACS Nano* **5,** 8187–92 (2011).

24. Kim, Y.-J., Lee, J.-H. & Yi, G.-C. Vertically aligned ZnO nanostructures grown on graphene layers. *Appl. Phys. Lett.* **95,** 213101 (2009).

25. Radisavljevic, B., Radenovic, A., Brivio, J., Giacometti, V. & Kis, A. Single-layer MoS2 transistors. *Nat. Nanotechnol.* **6,** 147–50 (2011).